

**Design of Low-intensity Pulsed Ultrasound Device, Intensity Sensor  
and Its Application to Enhance Vaccine Production**

by

Jida Xing

A thesis submitted in partial fulfillment of the requirements for the degree of

Doctor of Philosophy

in

Biomedical Engineering

Department of Electrical and Computer Engineering

University of Alberta

© Jida Xing, 2016

## **Abstract**

The application of low-intensity pulsed ultrasound (LIPUS) technology for therapy has become a promising interdisciplinary research field in biomedical engineering. This thesis covers two important topics in the field: LIPUS design and its biological applications.

In therapeutic ultrasound applications, accurate ultrasound output intensities are crucial because the physiological effects of therapeutic ultrasound are very sensitive to the intensity and duration of these applications. Although radiation force balance is a benchmark technique for measuring ultrasound intensity and its output power, it is costly, difficult to operate, and compromised by noise vibration. To overcome these limitations, the development of a low-cost, easy to operate, and vibration-resistant alternative device is necessary for rapid ultrasound intensity measurement. Therefore, a novel two-layer thermoacoustic sensor using an artificial neural network technique was proposed and validated to accurately measure low ultrasound intensities between 30 and 120  $\text{mW}/\text{cm}^2$  at a frequency of 1.5 MHz. The first layer of the sensor design is a cylindrical absorber made of plexiglass, followed by a second highly attenuating layer composed of polyurethane rubber to absorb ultrasound energy efficiently. The sensor determined ultrasound intensities according to a temperature elevation induced by heat converted from incident acoustic energy. After obtaining multiple parameters of the sensor characteristics through calibration, an artificial neural network was built to correct temperature drifts and increase the reliability of the thermoacoustic measurements through

iterative training. After calibration, the designed sensor was able to measure ultrasound intensity in 12 seconds with an average error of  $1.31 \text{ mW/cm}^2$ .

For biological experiments, low-intensity pulsed ultrasound (LIPUS) was employed to enhance vaccine production as a unique physical-based approach. In this study, hepatitis B vaccine based on baculovirus-insect cell expression systems (BCESs) was used as a model system to demonstrate how LIPUS technology can increase the vaccine production. The experimental results demonstrated that LIPUS stimulation of 10 minutes per day at a frequency of 1.5 MHz, intensity of  $60 \text{ mW/cm}^2$  significantly increased both cell growth and vaccine production. The tests also showed that continuous sonication is better than stopping LIPUS stimulation after viral infection. Continuous ultrasound stimulation can achieve about a 40% increase in HBV S1/S2 production, while stopping sonication after viral infection increased the cell productivity by 11%. This finding is very meaningful for efficiently shortening vaccine production time or increasing the yield of proteins for vaccine use, which would reduce the manufacture costs of the vaccines.

## **Preface**

Chapter 2 of this thesis has been published as J. Xing, M. Choi, W. Ang, X. Yu and J. Chen. “Design and Characterization of a Close-proximity Thermoacoustic Sensor.” *Ultrasound in Medicine & Biology* 39.9: 1613-1622, 2013. I was responsible for the sensor design, measurement experiments, data analysis and the manuscript composition. M. Choi contributed to sensor concept formation and design, data collection board design and manuscript composition. W. Ang and X. Yu contributed to data collection board design. Dr. J. Chen supervised the work, provided valuable guidance and revised the manuscript.

Chapter 3 of this thesis has been published as J. Xing and J. Chen. “Design of a Thermoacoustic Sensor for Low Intensity Ultrasound Measurements based on an Artificial Neural Network.” *Sensors* 15.6: 14788-14808, 2015. I was responsible for the improved sensor design, measurement experiments, data analysis and the manuscript composition. Dr. J. Chen supervised the work, provided valuable guidance and revised the manuscript.

The work presented in Chapter 4 has been submitted to Scientific Reports as: J. Xing, Y. Duan, C. Hu, A. Ma, R. George, D. Cheng, J. Z. Xing and J. Chen, “Increasing Vaccine Production Using Pulsed Mechanical Waves”. I was responsible for the ultrasound device preparation and calibration, vaccine growth experiments and the manuscript composition. Y. Duan and D. Cheng contributed to the molecular dynamic simulation. C. Hu performed Western blot tests. A. Ma and R. George provided valuable feedback of the experiment designs. Dr. J. Z. Xing

initiated the research and provided feedback during the course of the studies. Dr. J. Chen supervised the work, provided valuable guidance and revised the manuscript.

## **Acknowledgements**

I would like to express my appreciation to Dr. Jie Chen for providing me the valuable opportunity to pursue the Doctor of Philosophy degree in the University of Alberta and perform this project in his research group; I would not have completed this thesis without his guidance, encouragement and support. I would like to express my appreciation to the members of my thesis committee: Dr. Jie Han, Dr. Xihua Wang, Dr. Hao Liang and Dr. Hua Li. I also would like to thank Woon Ang, Michael Choi, David Zhao, Xiaojian Yu, Chang Ge and the other group members for their support and help.

# Table of Contents

1. INTRODUCTION	1
1.1 ULTRASOUND	1
1.2 ULTRASOUND IN BIOMEDICAL FIELD AND ITS THERAPEUTIC MECHANISMS	2
1.2.1 Biomedical Applications of Ultrasound	3
1.2.2 Therapeutic Mechanisms of Ultrasound	4
1.3 CALIBRATION OF ULTRASOUND INTENSITY	7
1.3.1 Conventional Techniques	8
1.3.2 Thermoacoustic Sensing	11
1.4 LOW-INTENSITY PULSED ULTRASOUND FOR ENHANCING VACCINE PRODUCTION	15
1.5 MOTIVATION	19
2. PRELIMINARY THERMOACOUSTIC SENSOR DESIGN	22
2.1 SENSOR DESIGN	22
2.1.1 Ultrasound Propagation Theory	22
2.1.2 Physical Sensor Design and Its Set-up	25
2.2 SENSOR CALIBRATION AND ALGORITHM DESIGN	31
2.2.1 Calibration for Thermistor Data	31

2.2.2 Substitution Calibration	33
2.2.3 Approach for Relating Temperature Rise to Ultrasound Intensity	36
2.2.4 Transient Temperature Model	39
2.2.5 Relationship between Coefficient C and Ultrasound Intensity	46
2.2.6 Effect of Ambient Temperature	48
2.2.7 Sensor Algorithm	51
2.3 SENSOR PERFORMANCE EVALUATION	54
2.3.1 Ultrasound Medium Temperature	54
2.3.2 Sensor Response Time	55
2.3.3 Intensity Measurement Result	58
2.4 DISCUSSION	62
3. IMPROVED THERMOACOUSTIC SENSOR DESIGN	64
3.1 SENSOR DESIGN	64
3.2 SIMULATION OF ULTRASOUND PROPAGATION IN SENSOR	66
3.3 TRANSIENT TEMPERATURE MODEL EVALUATION	78
3.4 ARTIFICIAL NEURAL NETWORK IN SENSOR DESIGN	85
3.4.1 Artificial Neural Network Structure and Back Propagation Algorithm	87

3.4.2 Artificial Neural Network Model in Sensor Design	90
3.4.3 Artificial Neural Network Training	91
3.5 SENSOR PERFORMANCE EVALUATION	98
3.5.1 Neural Network Evaluation with Untrained Data Sets	98
3.5.2 Network Temperature Compensation Performance	100
3.5.3 Sensor Response Time	102
3.5.4 Measurement Comparison with the Previous Design	103
3.6 DISCUSSION	106
4. INCREASING VACCINE PRODUCTION USING LOW INTENSITY PULSED ULTRASOUND	111
4.1 MATERIALS AND METHODS	112
4.1.1 Cell Culture and Infection	112
4.1.2 Ultrasound Treatment Method	115
4.1.3 Analysis Methods	116
4.1.3.1 Cell Count	116
4.1.3.2 Protein Analysis	118
4.2 EXPERIMENT RESULTS	121
4.2.1 Screening LIPUS Conditions for Insect Cell Growth	121
4.2.2 LIPUS Stimulation and Infection	124
4.2.3 Checking Protein Production Increase	125

4.3 DISCUSSIONS	127
4.3.1 One Treatment Per Day is Better than Two Treatments Per Day	127
4.3.2 Treatment of 10 Minutes Per Day is Better than that of 15 Minutes Per Day	128
4.3.3 Continuous Ultrasound Stimulation is Better than No Stimulation After Infection	129
4.3.4 Protein Production Increase	129
5. CONCLUSIONS AND FUTURE WORK	131
5.1 CONCLUSIONS	131
5.2 FUTURE WORK	134
REFERENCES	136
APPENDIX A: PRELIMINARY THERMOACOUSTIC SENSOR CODE	150
APPENDIX B: IMPROVED THERMOACOUSTIC SENSOR CODE	158

## **Lists of Figures**

Figure 1.1: Schematic of radiation force balance

Figure 1.2: The figure of an ultrasound holder with an array of transducers used in biological experiments to stimulate cells for various therapeutic applications

Figure 2.1: The geometry of the ultrasonic field

Figure 2.2: Schematic of the standard thermoacoustic sensor and its setup

Figure 2.3: Close proximity setup of the thermoacoustic sensor. The sensor is placed in direct contact with the ultrasound transducer via degassed water as medium

Figure 2.4: Thermistor curve fitting based on the quadratic model

Figure 2.5: Temperature data over time at intensities of  $40 \text{ mW/cm}^2$ ,  $60 \text{ mW/cm}^2$ , and  $80 \text{ mW/cm}^2$

Figure 2.6: Temperature vs. Time curve measured by the sensor at  $40 \text{ mW/cm}^2$

Figure 2.7: Temperature data over time measured by the thermoacoustic sensor under ultrasound intensity of  $80 \text{ mW/cm}^2$

Figure 2.8: Temperature vs. time data measured by the thermoacoustic sensor for an applied ultrasound intensity of  $80 \text{ mW/cm}^2$ . Data was fit with equation (2.9) using the least squares model with prediction bounds with 95% certainty

Figure 2.9: Temperature vs. time data measured by the thermoacoustic sensor at the ultrasound intensity of  $40 \text{ mW/cm}^2$

Figure 2.10: Temperature vs. time data measured by the thermoacoustic sensor at the ultrasound intensity of  $60 \text{ mW/cm}^2$

Figure 2.11: Linear relationship between applied ultrasound and the calculated C coefficient

Figure 2.12: The sensor's temperature curves at ambient temperature  $22 \text{ }^\circ\text{C}$  and  $24 \text{ }^\circ\text{C}$  under the same ultrasound intensity  $100 \text{ mW/cm}^2$

Figure 2.13: Linear relationship between starting ambient temperatures and the calculated C coefficient under intensity of  $60 \text{ mW/cm}^2$

Figure 2.14: The thermoacoustic sensor's algorithm flowchart

Figure 2.15: Temperature drift of the coupling medium under intensity of  $100 \text{ mW/cm}^2$

Figure 2.16: Response time of the thermoacoustic sensor with respect to measurement error percentage

Figure 2.17: Response time of the thermoacoustic sensor design based on the transient temperature approach and the equilibrium temperature approach

Figure 2.18: Evaluation of the thermoacoustic sensor by comparing measurements made with the thermoacoustic sensor with measurements taken using a radiation

force balance. The linear line represents a 1:1 relationship between the Radiation Force Balance and the Thermoacoustic Sensor

Figure 3.1: The structure of the two-layer thermoacoustic sensor

Figure 3.2: The distributions of the medium and material parameters for sensor models in the ultrasound propagation direction. (a) The one-layer sensor model, (b) the two-layer sensor model

Figure 3.3: The source mask built for the acoustic source simulation in the 3-D model

Figure 3.4: The detector array built in the 3-D model to record output ultrasound pressure during the simulation

Figure 3.5: Pressure distribution of the generated ultrasound wave

Figure 3.6: Ultrasound pressure distributions of the remaining waves for (a) the two-layer sensor after attenuation, and (b) the one-layer sensor after attenuation

Figure 3.7: Thermal response comparison between the two-layer sensor and the one-layer sensor under the same intensity level of  $60 \text{ mW/cm}^2$

Figure 3.8: Curve fitting results for temperature rise data based on the first transient model

Figure 3.9: Curve fitting results for temperature rise data based on the three modes of transient profiles ( $60 \text{ mW/cm}^2$ )

Figure 3.10: Schematic of a three-layer artificial neural network

Figure 3.11: The mathematic model of a BP network

Figure 3.12: Model of the thermoacoustic sensor compensation using a neural network. The neural network algorithm is implemented using a microcontroller

Figure 3.13: Variation of mean squared error with training epochs (three hidden neurons)

Figure 3.14: MSE vs number of hidden neurons in a three-layer neural network

Figure 3.15: The agreement between the network's output intensity and target intensity

Figure 3.16: Comparison between the estimated data sets by the neural network and the real measurement data sets at 20 °C

Figure 3.17: Comparison between the estimated data sets by the neural network and the real measurement data sets at 25 °C

Figure 3.18: Ultrasound intensity error with and without network temperature compensation

Figure 3.19: Response time of the one- and two-layer sensors with respect to measurement error percentage

Figure 3.20: Comparison of the new sensors design measurements with that of the radiation force balance as a means to conduct a performance evaluation

Figure 4.1: Sf9 cells observed under a microscope stage

Figure 4.2: Experimental setup for increasing vaccine production. Here SonaCell is the device to generate low-intensity pulsed ultrasound (LIPUS)

Figure 4.3: Insect cell growth under different ultrasound intensities at 40, 60 and 80  $\text{mW}/\text{cm}^2$

Figure 4.4: Insect cell growth in 30 mL media in shake flask with various ultrasound treatments. The control refers to insect cell culture without ultrasound treatment. The ultrasound intensity is set at 60  $\text{mW}/\text{cm}^2$

Figure 4.5: Insect cell growth in 30 mL media in shake flask with 10 minute and 15 minute ultrasound treatments. Control refers to insect cell culture without ultrasound treatment. The ultrasound intensity is set at 60  $\text{mW}/\text{cm}^2$

Figure 4.6: Cells' growth curve. Method 1 is the one that stops sonication after infection while method 2 is the one with continuous ultrasound stimulation. Cells were infected by baculovirus at 72 hours

Figure 4.7: The Western blotting results. ImageJ software was used to measure the band area density change

## **Lists of Tables**

Table 2.1: Acoustic properties of ultrasound medium and plexiglass (20°C)

Table 2.2: Curve fitting accuracy of thermistor calibration

Table 2.3: Coefficients of the transient model for the applied ultrasound intensity of 80 mW/cm<sup>2</sup>

Table 2.4: Accuracy of fit analysis for temperature data at 80 mW/cm<sup>2</sup>

Table 2.5: Accuracy of fit analysis for data for applied ultrasound intensities of 40 mW/cm<sup>2</sup> and 60 mW/cm<sup>2</sup>

Table 2.6: Calculated *C* coefficients at various ambient temperatures

Table 2.7: Thermoacoustic sensor measurements

Table 2.8: Comparison between measurements made using a radiation force balance and measurements made using a thermoacoustic sensor

Table 3.1: Acoustic properties of media and materials (20°C)

Table 3.2: The coefficients of the first transient model curve fitting

Table 3.3: Curve fitting accuracy of the first transient model curve fitting

Table 3.4: The coefficients of the curve fitting based on the three modes of transient profiles

Table 3.5: Curve fitting accuracy of the three modes of transient profiles

Table 3.6: Measurement results of the improved sensor design

Table 3.7: Advantages and disadvantages of radiation force balance and the thermocoustic sensor

Table 4.1: Cell productivity increase after sonication

## List of Abbreviations

<b>Acronyms</b>	<b>Definition</b>
LIPUS	low-intensity pulsed ultrasound
HIFU	high intensity focused ultrasound
BCESs	baculovirus-insect cell expression systems
HBV	hepatitis B virus
RMSE	root-mean-square error
FFT	fast Fourier transform
ANN	artificial neural network
BP	back propagation
MSE	mean square error
MOI	multiplicity of infection
CP	cell productivity

# Chapter 1

## Introduction

### 1.1 Ultrasound

Ultrasound is acoustic wave with frequencies higher than 20 KHz, beyond human hearing range [1]. Although operating at different frequency ranges, both ultrasound and audible sound are mechanical waves. While electromagnetic waves, such as visible light, X-rays and radio waves, are able to travel in a vacuum environment, acoustic waves have to propagate through a physical medium. Relying on back and forth mechanical vibrations of the medium molecules, acoustic energy is transferred from one location to another [2]. Modern ultrasound devices are capable of generating a wide frequency range from 20 kHz to several GHz.

The discovery of ultrasound dates back to 18th century when Italian biologist Lazzaro Spallanzani found out that bats used echolocation to navigate and forage in complete darkness, and the acoustic wave used for echolocation was later proved to be ultrasound. Later in 1880, physicists Jacques and Pierre Curie discovered the piezoelectric effect, which describes a reversible relationship between mechanical and electrical energy, that is, applying mechanical stress to piezoelectric materials can produce electrical charge in the materials and vice versa [3]. This discovery has far-reaching implications for the development of ultrasound technology as piezoelectric materials can be used to either generate or detect ultrasound. After the incident of Titanic in 1912, the demand for detecting

icebergs and salvaging the ship wreckage spurred research on the detection of submerged objects. French physicist Paul Langevin, a former student of Pierre Curie, made use of piezoelectric quartz crystal to generate ultrasound and detect submerged objects through echo location [3]. The technology was further advanced during World War I and World War II when the Allies developed a military sonar system to locate and counter threats from submarines [4]. Since then the application of ultrasound technologies was popularized to other fields.

In addition to military applications, ultrasound has been widely applied in industry field. Non-destructive testing, one of the most important applications, measures the thickness of objects and detects invisible flaws based on the principle of echo location. The method achieves minimal health concern and relatively low-cost compared to the traditional ionizing radiation method. Moreover, using ordinary water as a cleaning solvent, ultrasound can clean a variety of solid items, such as jewellery, lenses, industrial parts and instruments. Other common industrial applications include ultrasonic welding and sonication induced by ultrasound to improve reactant mixing and chemical reactions.

In addition to military and industrial applications, ultrasound is also extensively utilized in biomedical fields, aiding diagnosis of healthy conditions and treatment to improve human health and living quality.

## **1.2 Ultrasound in Biomedical Field and Its Therapeutic Mechanisms**

### **1.2.1 Biomedical Applications of Ultrasound**

Based on functional orientation, the ultrasound applications in biomedical field can be categorized into two classes: diagnostic and therapeutic applications. Sonography is the most well-known diagnostic application of ultrasound. As a medical imaging technique, sonography visualizes the internal organ and tissue of human body by pressing a probe or detector directly on the overlying skin in order to detect and monitor pathological changes or fetus development during pregnancy. Endoscopic ultrasound, a derivative technique of sonography, inserts the detector inside the body to obtain clearer details of deeper organs, which remarkably improves tumor diagnosis [5].

Although sonography is the most well-known ultrasonic technique in the biomedical field, therapeutic applications of ultrasound actually predate diagnostic usage. As early as 1927, it was recognized that ultrasound was able to induce a range of biological changes in living systems, which initiated the safety studies of ultrasound applications and elicited speculation of its therapeutic utility in health domain [6]. A range of biological benefits induced by ultrasound have been described in the literature, including physiotherapy for tissue healing, tumor ablation, facilitated drug delivery and so on [7]. The biological effects of ultrasound originate from thermal and mechanical impacts on cells and tissues, varying in degrees as a function of the dosimetry of the applied ultrasound. Generally, the applications of ultrasound in therapy can be divided into two categories by intensity: high intensity and low intensity. The main application of high intensity ultrasound in medicine is high intensity focused ultrasound (HIFU).

HIFU is a non-invasive surgical technique that delivers heat induced by high-intensity ultrasonic energy to a defined region and destroys the pathogenic tissue rapidly with high temperatures. Compared to the high intensity ultrasound, the ultrasound in the low intensity has much wider applications in therapy, which include physiotherapy, fracture repair, sonophoresis, sonoporation and gene therapy [7].

### **1.2.2 Therapeutic Mechanisms of Ultrasound**

Therapeutic effects induced by ultrasound in biomedical applications arise from the interaction between ultrasound energy and biological materials. Thermal effects and non-thermal effects are two kinds of mechanisms commonly used to explain the induced beneficial changes by ultrasound [8] [9].

When ultrasound waves propagate through tissues or cells, the ultrasound energy is attenuated and absorbed, and the absorbed energy is converted into heat and causes temperature changes in tissues or cells. Employing thermal mechanism, HIFU delivers high-intensity focused ultrasonic energy around  $1 \text{ kW/cm}^2$  to generate a temperature above  $60 \text{ }^\circ\text{C}$  in the target region within 1-2 seconds and kill cells in diseased tissue instantly for tumor ablation [8].

Low intensity ultrasound, on the other hand, induces biological effects by stimulating cellular activity. Enzymatic activity plays an important role in regulating cell structure and function. Biochemical reaction rates in cells increase with temperature, since enzymatic activity depends on temperature. Ultrasound is able to improve the cellular activity by increasing surrounding temperature

through thermal effects, thus increases overall cellular functions [10]. The degree of the regulating effects counts on the applied ultrasound intensity and treatment time, which governs the temperature rise rate and the achieved maximum temperature [8]. It is worthy to note that enzymatic activity does not always increase with the temperature rise. Once the maximum temperature is over 45 °C, enzymatic activity goes down and finally stops due to protein denaturation, which consequently generates an adverse influence on cellular activity [10]. Collagen, as a structural protein, is a main component of a wide variety of connective tissues, which exists abundantly in bones, skin, blood vessels, cartilage, tendons, ligaments and the dentin in teeth [11]. As collagen is a kind of large protein molecule and has high absorption coefficient of ultrasound, collagenous tissues can absorb ultrasound energy and generate heat. With appropriate control of time and intensity of ultrasound treatment, the generated heat can raise the temperature of collagenous tissues several degrees above normal temperature and improve the blood flow supply to the area [7]. Heating of muscle and nerve roots using absorbed ultrasound energy also helps to relieve muscle spasm and pain [12-14]. The therapeutic effects include an improvement of extensibility and flexibility of collagenous structures to improve healing of tendons, joints and scar tissues [15-17].

Ultrasound can also take effect via non-thermal mechanisms. When ultrasound waves propagate through tissue, acoustic streaming and cavitation are induced due to the acoustic pressure field or radiation forces. The acoustic streaming and cavitation can change the concentration gradients outside a cell

membrane and improve cell permeability, which can help molecules and ions to diffuse through a cell membrane [8]. It has been proved that nutrient uptake of cell, such as calcium and potassium, increases after ultrasound treatment [18] [19]. The mechanism is also used for drug and gene delivery. Direct drug delivery to the targeted tissue or cells is an effective way for therapy and avoiding side effects of the drugs, especially for cancer chemotherapy. However, the delivery of drugs to solid tumors is always inefficient in reality; conversely, the toxicity of drug could affect healthy cells and tissues [10]. Through transiently improving permeability of the tumor cells using ultrasound, the drug delivery efficiency to the diseased tissue can be greatly increased, which in turn reduces the drug toxicity to other healthy tissues [20]. The transfer of genes into the target and diseased cells for therapeutic effects is called gene therapy. Enhancement in gene transfer and expression into cells in vitro has also been demonstrated through ultrasound treatment [21] [22].

Ultrasound treatments for tissue repair and healing are typical applications of ultrasound through the thermal and non-thermal mechanisms, which have been widely studied and demonstrated in both laboratory and clinical trials. Ultrasound plays diverse roles in different phases of the healing process. For the initiate inflammatory phase after injury, although ultrasound does not work as an anti-inflammatory agent itself, it can activate and migrate immune cells to the injured tissue to help the repair process and shorten the healing period [8] [9]. The second stage is the proliferative phase, at which collagen is essential for cell and tissue repair [8]. Ultrasound has been demonstrated to improve fibroblasts for collagen

synthesis, thus can accelerate the healing process at this stage [8] [23] [24]. Tissue remodelling is the final stage of tissue healing, at which ultrasound enhances tissue healing by changing collagen fiber pattern [9]. Scar tissues under ultrasound treatment have been shown enhanced strength and elasticity compared to scar tissues without treatment [8]. Therapeutic benefits under ultrasound treatments for tissue healing have various applications including muscle spasm and pain relief, tendon and joint treatment, wound healing, scar tissue repair, skin rejuvenation and bone injure repair [7, 12-17, 25, 26].

### **1.3 Calibration of Ultrasound Intensity**

Low intensity pulsed ultrasound (LIPUS) has shown great utility and promise in medical therapeutic treatments, including bone and soft tissue healing, tooth root resorption [27-30], stem cell proliferation and differentiation [31, 32], antibody and antibiotic production [33-35]. In these applications, 1.5 MHz has been validated to be an effective stimulation frequency, and the applied intensities are within a range between 30 mW/cm<sup>2</sup> and 100 mW/cm<sup>2</sup>. Ultrasound intensity can be defined as the power of the ultrasound beam divided by its corresponding area, which represents temporal-average rate of ultrasound energy flowing into a specific unit area. Accurate calibrations of ultrasound intensities have become important because treatment outcomes are highly dependent on the intensities and duration of LIPUS. If the ultrasound exposure level is too low, no biomedical or clinical effect will be observed, while too high a dose can cause adverse or damaging effects to the target tissues or cells [36]. Therefore, it is necessary to accurately measure and calibrate the intensities of the LIPUS devices.

### 1.3.1 Conventional Techniques

Currently, there are two conventional and commonly used techniques to evaluate ultrasound output parameters: hydrophones and radiation force balances. A hydrophone can be considered as a microphone to record the underwater acoustic waves, which uses a piezoelectric material to convert acoustic pressure changes into electrical signals based on the piezoelectric effect. Through a preamplifier, the converted electrical signals are amplified and finally displayed on an oscilloscope. Therefore, the hydrophone can output acoustic pressure time waveform on an oscilloscope. While hydrophones can describe pressure waveform of an acoustic field, they are not designed to measure overall output intensity. Although the acoustic intensity can be estimated based on the plane-wave approximation of the acoustic field [37], the estimation is very complicated and not accurate.

Radiation force balance is a benchmark technique to measure ultrasound power and intensity for both diagnostic and therapeutic ultrasound systems. As indicated in Figure 1.1, the key component of a radiation force balance is a target in the water placed on the way of acoustic wave generated by a transducer. Acoustic radiation force, generated from the interaction between the target as an obstacle and the propagating acoustic wave, is related to the acoustic radiation pressure over the surface of the target. The radiation force balance employs the physical phenomenon and the relationship between the acoustic radiation pressure and its generated force to do the measurement. As a widely accepted technique, high quality radiation force balances normally have an uncertainty rate of less

than 10%. Commercial products using radiation force technique are commercially available from companies like Ohmic Instruments, Precision Acoustics, and Onda Corporation.

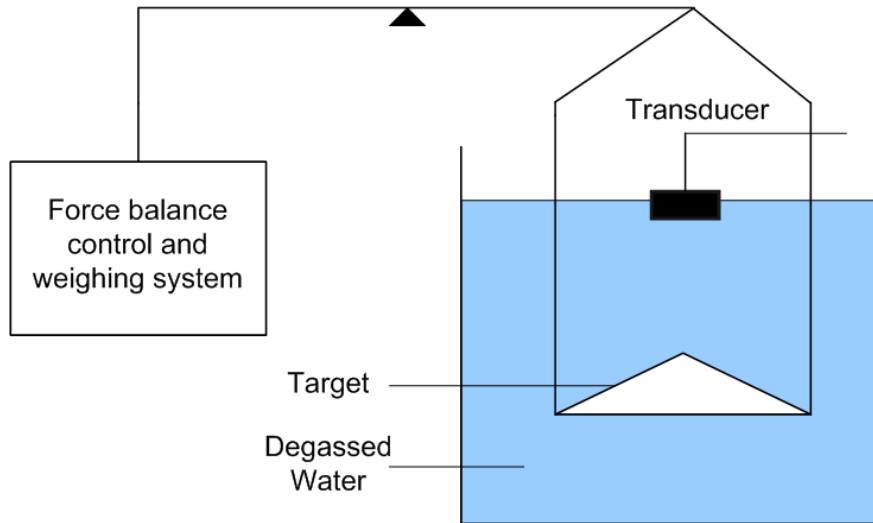


Figure 1.1: Schematic of radiation force balance.

Although the radiation force balance technique is widely accepted and devices based on the technique are commercially available, it has some obvious drawbacks, such as costly, difficult to operate, and susceptible to noise [38]. In an environment with noise vibration, the error of a radiation force balance for low intensity ultrasound measurement can easily surpass 20%. In a working environment such as in a biology laboratory, the measurement is likely to be affected by background vibrations produced from other lab equipment. Air currents from air conditioning system also affect the force balance of the device, which makes the measurement results inaccurate. Moreover, the use of the radiation force balance is restricted in some situations. Due to its setup, the technique cannot make measurements in the field (i.e. during equipment service

activities) in certain settings. For example, an ultrasound holder with an array of transducers is commonly used in biological experiments to stimulate cells for various therapeutic applications, as shown in Figure 1.2. In this situation, it is quite difficult for the radiation force balance to directly measure the intensity of each individual transducer that has been fixed in the ultrasound holder, since it uses a large target to collect the ultrasonic beam, which in turn would also collect the ultrasound beams of several other transducers simultaneously. For biological studies, the technique based on large volume of water to set up is difficult to disinfect and can cause contamination problems. In addition, the measurement accuracy of the radiation force balance is directly related to the expertise and experience of the person to set up the device and operate it. Therefore, the development of a vibration-resistant, easy-to-operate and low-cost alternative measurement device is indispensable for rapid measurement and calibration of ultrasound intensity in the field.

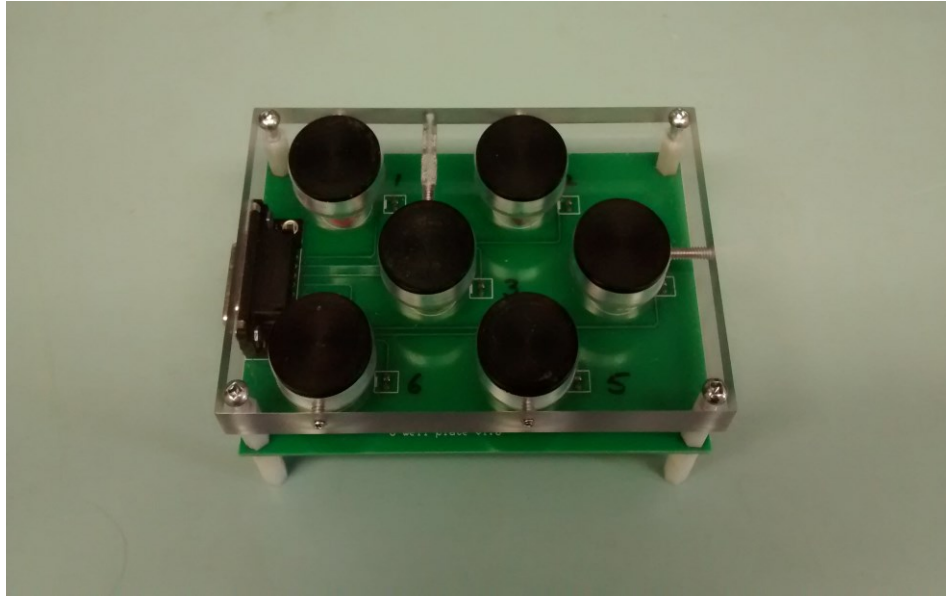


Figure 1.2: The figure of an ultrasound holder with an array of transducers used in biological experiments to stimulate cells for various therapeutic applications.

### 1.3.2 Thermoacoustic Sensing

Compared to previously mentioned techniques, thermoacoustic sensing, as a very simple, vibration-resistant and cost-effective technique, has the potential to be an alternative approach to determine ultrasound intensity. This type of sensor determines the ultrasound intensity according to the temperature rise caused by the heat produced from incident acoustic energy [39, 40]. A sensor using the thermal method was developed to directly measure spatial-peak temporal-average intensity ( $I_{\text{spta}}$ ) or determine intensity beam profiles of ultrasonic fields [40-42], as it is commonly performed, for instance, in acoustic output characterization of diagnostic ultrasonic equipment for safety considerations, which presents an alternative to the traditional methods of hydrophone. Different from spatial-peak temporal-average intensity ( $I_{\text{spta}}$ ), which represents the maximum intensity in the

acoustic field, spatial-average temporal-average intensity ( $I_{\text{sata}}$ ) describes the average intensity of the acoustic field [7]. Therapeutic ultrasound applications require accurate measurements of spatial-average temporal-average ( $I_{\text{sata}}$ ), which cannot be directly measured by hydrophones or the above mentioned sensor. To this end, we designed thermoacoustic sensors to directly measure  $I_{\text{sata}}$  for therapeutic ultrasound applications. The previous thermoacoustic sensors are based on a conventional beam-plotting set-up in a water tank, which in principle can be used to calibrate a range of transducers, but the set-up procedure is very complicated, which requires the sensor and transducer to be placed in a large water tank, therefore, the set-up demands large space, large amount of degassed water and time-consuming adjustment and measurement. Degassed water is usually made by heating the distilled water for around one hour to remove the remaining gas, and then wait for the hot degassed water to cool down. The preparation of large amount of degassed water is time-consuming and inconvenient. More important, the traditional beam-plotting set-up limits the sensor applications in many cases, for example bioreactors, or in clinic to measure ultrasound intensities during treatments. To make the sensor easy to operate and maintain consistency during each measurement, a close-proximity thermoacoustic sensor was proposed and designed to simplify sensor operation, the designed sensor was directly coupled to the transducer through ultrasound medium (ultrasound gel or degassed water) to perform the measurements in the field. Such a design can dramatically reduce the difficulty of suspending sensor and

transducer separately in a large water tank with conventional procedure [39-42], which is very convenient to use.

Previously developed thermoacoustic sensors have mostly used the relationship between the equilibrium temperature reached by the thermoacoustic sensor and the incident ultrasound intensity to indirectly measure the ultrasound intensity [39-42]. However, this model requires an impractical amount of time for quick measurement. For instance, it takes 400 seconds to reach equilibrium (corresponding to ultrasound intensity of  $40 \text{ mW/cm}^2$ ). The equilibrium method doesn't satisfy our design purpose, since the long waiting time brings inconvenience to the measurement. For ultrasound intensity calibration, it requires intensity adjustment of ultrasound generator based on the sensor measurement, and the procedure should be repeated at least dozens of times to finally achieve the desired ultrasound intensity. If each sensor measurement takes 400s, the time for ultrasound calibration of each transducer will be more than several hours. Furthermore, the long measurement time prevents the sensor integrating with ultrasound generators to realize an ultrasound auto-calibration system, since it is quite difficult for the system to accurately control and adjust ultrasound intensities through feedback loop based on long measurement time. In order to quickly measure ultrasound intensity, we have implemented an algorithm that determines the incident ultrasound intensity by fitting the temperature vs. time data to a transient model that describes the time dependent profile of the spatially averaged temperature at the absorber's back face [43, 44]. Through the transient model, the

sensor design can detect initial temperature rise trend due to ultrasound energy and determine ultrasound intensity in a very short time.

We developed a preliminary thermoacoustic sensor based on the close-proximity concept and the transient model. The measurement results prove the feasibility of the promising method. To apply the close-proximity thermoacoustic sensor design for ultrasound calibration, enhancement in response time, accuracy and consistency of the sensor design is still necessary. Therefore, further studies are still needed. An improved design was developed to further improve the performance of the sensor design through a new structural design and artificial neural network algorithm.

The performance of the thermal sensor heavily depends on the conversion efficiency from the low intensity ultrasonic energy into heat. In our preliminary sensor design, a cylindrical plexiglass absorber was applied to convert ultrasound energy into heat. To improve the conversion efficiency, we proposed a two-layer structure to increase the absorption efficiency of ultrasound energy in our improved design. The first layer was a cylindrical plexiglass absorber, the same as our previous design. A second layer is made of polyurethane rubber with high attenuation coefficient to absorb extra ultrasound energy. This improved design provided higher conversion efficiency than our previous one-layer design.

The thermoacoustic sensor measures the temperature rise caused by incident ultrasound energy to determine the ultrasound intensity. However, in the close-proximity setup, the sensor characteristics are not only dependent on applied

ultrasound intensity, but also on ambient temperature and the slightly changing acoustic properties of absorber materials as the absorber heats up, which create a complex problem in sensor design. To obtain an accurate and consistent measurement, the effect of various ambient temperatures should be considered and compensated for the thermal sensor design. The traditional computational method usually identifies the exact mathematical relationship through data interpolation; however, this method is incompetent to solve the problem, since it is extremely difficult to resolve the mathematical formula, if not impossible, among multiple confounding variables such as the temperature change of the sensor, applied ultrasound intensity and ambient temperature from measured data. In the preliminary design, we find a solution using extrapolation and interpolation based on calibration values, but the method is still unsatisfactory due to the requirement of complex calibration and calculation procedures and limited improvement in accuracy. In the improved design, we propose the implementation of an artificial neural network to identify the relationship and solve the problem. An artificial neural network can map the implicit relationship of inputs and outputs through the training and testing of measured data, which has been applied to compensate for the various nonlinear errors in system designs [45-50]. Through proper training, the artificial neural network can compensate for the nonlinear errors, enabling a direct read-out of the applied ultrasound intensity.

#### **1.4 Low-intensity Pulsed Ultrasound for Enhancing Vaccine Production**

Low intensity pulsed ultrasound (LIPUS), as a type of non-continuous ultrasound wave with low intensity, is widely used in biomedical field. For therapeutic applications, our lab has developed a commercial low intensity pulsed ultrasound generator (SonaCell) at frequency of 1.5 MHz, which has been successfully applied to improve stem cell proliferation and differentiation [32] and increase antibody and antibiotic production [33-35]. The positive effects of LIPUS lead us to hypothesize that a physical-based stimulation could enhance vaccine protein production. To this end, we conducted a series of proof-of-concept experiments. To the best of our knowledge, we are the first to use physical-based sonication approaches to increase vaccine production.

Vaccines have become a highly suitable approach to control contagious diseases in humans due to cost-efficiency and ease-to-implement [51]. However, because of the costs associated with manufacturing these vaccines, existing vaccines are often not accessible in the developing world, especially in economically underprivileged countries. Increasing vaccine production is a highly effective way to reduce the costs of the vaccines and promote universal vaccine immunization, which will further help to control healthcare spending associated with infectious diseases and ease the financial burden worldwide. In my research project, we applied LIPUS technology to increase the production of hepatitis B vaccine based on baculovirus-insect cell expression systems (BCEs). Hepatitis B vaccines are used as a model system to demonstrate how the LIPUS technology can be applied to increase the vaccine production.

Hepatitis B virus (HBV) is the cause of infectious Hepatitis B liver disease, which has caused epidemics in Asia and Africa [52]. It has been shown that the virus has infected about 30% of the world population at one point in their lives [53]. Among them, more than 350 million are chronic carriers, who may suffer from acute hepatitis or chronic liver diseases like cirrhosis and even hepatomas (liver cancer) [53-55]. 786,000 people die each year from HBV infection, making it a leading cause of mortality and one of the top health priorities in the world [53, 56]. The HBV is carried in blood and other body fluid and can spread from carriers to others through various means [56]. There are effective prophylactic vaccines in the market to protect individuals from HBV infection and control the spread of hepatitis B. However, there is a non-responder rate of 10-15% to the conventional vaccine based on the sAg antigen [57]. In addition, no therapeutic vaccine to treat chronic infection exists at the moment in the market to induce immune responses against HBV in chronically HBV-infected individuals. HBV S1/S2 antigens are good target antigens for developing a therapeutic vaccine to treat HBV carriers or non-responder to the conventional vaccine, since they can produce a superior immunologic response compared to the current sAg antigen [56] [57].

HBV vaccines were originally developed from HBV antigen (sAg) isolated from blood plasma of individuals who had long-standing Hepatitis B viral infection. The vaccines produced with this method have been used for the past two decades, but the limitations are quite obvious, such as high production cost, limited availability of human plasma, poor acceptance rate and more importantly

the risk of opportunistic infections [58] [59]. Current methods to increase vaccination production focus on synthetic recombinant DNA technology based on yeast expression systems, which has been well established and widely used. However, serious adverse reactions, such as skin, rheumatic, vasculitic, hematologic, ophthalmologic and neurologic reactions, have been reported occasionally [60]. In addition, the yeast expression systems have difficulty producing some complex-structure proteins. The systems were initially employed to produce Pre-S2 antigen in Belgium, Japan, and the United States, but the attempts failed [56]. Using recombinant DNA technology based on baculovirus-insect cell expression systems (BCEs) is an alternative approach because BCEs have several advantages:

(1) It is highly versatile and can rapidly generate a wide range of complex and biologically active proteins for therapeutic vaccines [61], which make the system produce complex-structure antigen that the yeast expression system fails to generate.

(2) The cultures are also easy to scale up because insect cells can grow in serum-free culture media without CO<sub>2</sub> incubator, which simplifies the purification process used to secrete proteins [62, 63].

(3) The baculovirus-insect cell expression systems is also considered safe for humans because insects are the host for the baculoviruses in nature and the baculoviruses are non-pathogenic to humans [63]. Several insect-cell based proteins are currently used as therapeutic agents and vaccines (e.g. Provenge).

The BCESs have been used to achieve high levels of expression of recombinant proteins not only for exploratory research, but also for commercial production. Currently, the insect cell based system is one of the major sources for recombinant protein production [63, 64].

## **1.5 Motivation**

The low-intensity pulsed ultrasound (LIPUS) technology is a powerful tool for therapeutic treatment and has opened a promising interdisciplinary research field in biomedical engineering, which includes both electrical design and biological experiments. For the electrical design, an ultrasound platform to deliver ultrasound for biological experiments is essential, which is constituted by an ultrasound generator device and a custom-designed ultrasound holder. To make the ultrasound platform work for various biological experiments, accurate measurement and calibration of ultrasound intensity generated by the ultrasound platform is important. One part of my research projects is to design a sensor based on the thermal method to measure and calibrate the intensity of LIPUS. Although the radiation force balance is still the gold standard for ultrasound intensity measurement, it is not suitable for real-time ultrasound monitoring in a working environment such as in a biology laboratory, since its measurement is likely to be affected by background vibrations produced from lab equipment. Moreover, its setup procedure is complex and may not be justified in many cases. The expertise and experience is also required for the people to operate the device to guarantee the measurement accuracy. In addition, the high price of the radiation force balance also impedes the popularity of the technique. Therefore, the development

of a vibration-resistant, cost-effective and easy-to-operate alternative measurement device becomes indispensable for rapid calibration of ultrasound intensity. For this purpose, a thermoacoustic sensor was designed and tested for low intensity pulsed ultrasound generated at a 1.5 MHz frequency, 20% duty cycle, 1 kHz pulse repetition frequency, and intensities between 30 and 120 mW/cm<sup>2</sup>. The sensor captures the beam, converts the ultrasound power into heat, and indirectly measures the spatial average time average ultrasound intensity ( $I_{\text{sata}}$ ), which provides an easy-to-operate alternative method for rapidly measuring low ultrasound intensity with high accuracy, especially in a practical environment like a biology laboratory. In the second part of the project, accurate LIPUS was applied to enhance vaccine production. Vaccines have been proven to be a highly effective and cost-efficient approach to control contagious diseases in humans, however, existing vaccines are often not accessible in the developing world, especially in economically underprivileged countries, due to manufacturing costs. Increasing vaccine production through LIPUS technology would reduce the costs of the vaccines and promote universal vaccine immunization, which can effectively control the infectious diseases worldwide. My expertise and experience in ultrasound intensity calibration and ultrasound platform design can contribute to the project and guarantee that LIPUS is regulated and applied to the biological experiment effectively for the biomedical effects. This part of the projects also enables me to gain more knowledge about how the biological experiments work, which in return helps to improve electrical designs of LIPUS devices and sensors in biology experiments. As an interdisciplinary research, the

project integrates knowledge in both electrical engineering and biology.

## Chapter 2

### Preliminary Thermoacoustic Sensor Design

#### 2.1 Sensor Design

##### 2.1.1 Ultrasound Propagation Theory

Before designing a thermoacoustic sensor for ultrasound intensity measurement, it is helpful to understand the acoustic field radiated by a transducer. The ultrasound wave generated by the transducer of the SonaCell ultrasound generator is a plane-wave. The geometry of the ultrasonic field can be divided into two zones as illustrated in Figure 2.1. The region near the transducer is called the near field, in which the shape of the ultrasonic field is a cylinder and the diameter is slightly smaller than the transducer. The length of the near field  $L$  is governed by the radius of the source transducer and the wavelength of the ultrasonic waves [65], which is represented by equation (2.1):

$$L = \frac{r^2 f}{v} \quad (2.1)$$

where  $r$  represents the radius of the source transducer,  $f$  is the frequency of the generated ultrasound and  $v$  is the sound velocity in the analyzed medium.

The zone next to the near field is called the far field, in which the ultrasound beam begins to diverge and ultrasound intensity starts to decrease as the angular displacement increases along acoustic propagation direction. The divergence angle  $\theta$  can be expressed as equation (2.2) [65]:

$$\theta = \sin^{-1}\left(\frac{0.6v}{rf}\right) \quad (2.2)$$

where  $r$  is the radius of the source transducer,  $f$  is the frequency of the generated ultrasound and  $v$  represents the sound velocity in the medium.

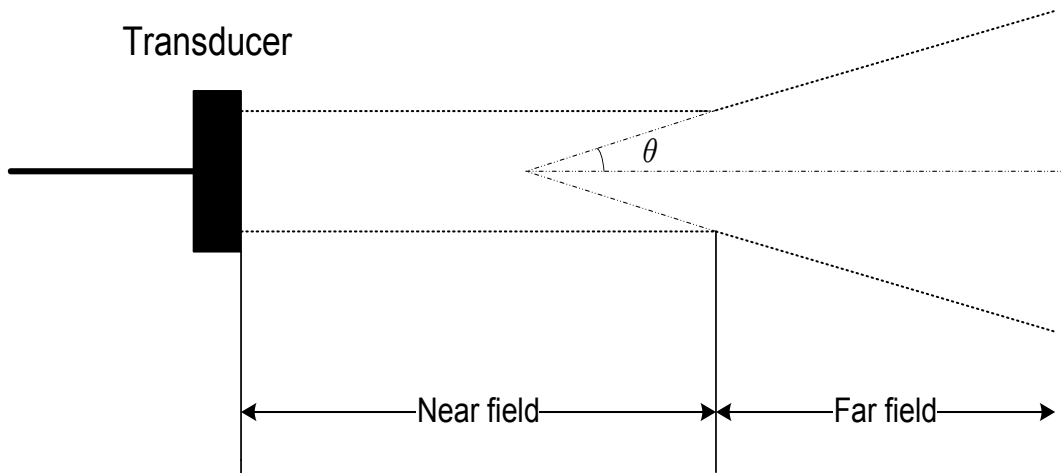


Figure 2.1: The geometry of the ultrasonic field.

The transducers used by the SonaCell ultrasound generator operate as 1.5 MHz frequency with a diameter of 2.6 cm. Being used as the coupling medium for ultrasound transmission, water has a sound velocity of 1481 m/s. Based on the equation (2.1), the length of the near field produced by the transducer is calculated to be 17 cm.

When the ultrasound wave generated by the transducer propagates from the first layer of medium/material to the second layer, part of the ultrasound wave is going to reflect back by the interface if the acoustic impedance of the second layer is different from that of the first layer. This difference of acoustic impedance

between the two layers of material/medium determines the proportion of ultrasound wave that enters the second layer.

Acoustic impedance ( $Z$ ) is related to a material's density and acoustic velocity, which can be calculated from equation (2.3) [66].

$$Z = \rho \times v \quad (2.3)$$

where  $\rho$  is the density of the material and  $v$  denotes the speed of sound.

A larger impedance mismatch will result in a higher percentage of energy reflecting off the interface. Since measuring intensity is interested in retaining ultrasound energy as much as possible, impedance match becomes crucial for sensor design and material selection. The percentage of the reflected ultrasound energy at the boundary can be calculated by equation (2.4) [66].

$$R = \left( \frac{Z_2 - Z_1}{Z_2 + Z_1} \right)^2 \times 100\% \quad (2.4)$$

where  $Z_1$  and  $Z_2$  represent the acoustic impedance of the two materials at the boundary.

Since acoustic attenuation affects the propagation of the ultrasonic wave, it is another important factor to consider when studying ultrasound propagation and sensor design. As ultrasound travels through a material, part of the ultrasonic energy is absorbed and converted to heat in the material. The acoustic absorption is related to the attenuation coefficient of the material ( $\alpha$ ), the frequency of the

incident ultrasound ( $f$ ) and the thickness of the material ( $x$ ) as shown in equation (2.5) [67].

$$I(x) = I_0 e^{-\alpha f x} \quad (2.5)$$

where  $I_0$  represents the incident ultrasound intensity, and  $I(x)$  is ultrasound intensity after transmitting a material with the thickness of  $x$ .

### 2.1.2 Physical Sensor Design and Its Set-up

The standard thermoacoustic sensor design and its setup are shown in Figure 2.2. The sensor design contains a cylindrical absorber for ultrasonic energy and a second hollow cylinder to insulate the absorber from the outside room temperature [39-44]. The ultrasound beam is generated by the transducer and propagates through water and reaches the front end of the sensor. At the water-sensor interface, a small percentage of incident ultrasound waves is reflected, while the remainder is transmitted into the absorber of the sensor. In a single reflecting approximation, by ignoring a small portion of the reflected ultrasound wave between the medium and sensor, almost all transmitted ultrasound energy is absorbed and converted into heat when traveling through the material (The ultrasound wave is fully reflected back by the back wall of the absorber due to large impedance mismatch at the absorber-air interface). Any reflected ultrasound waves return to the water through the front face of the sensor [43]. The generated heat induces temperature changes within the absorber which is measured by a temperature-sensing unit at the back end of the absorber. The thermoacoustic

sensor design estimates the ultrasound intensity based on the amount of temperature increase caused by the absorbed heat.

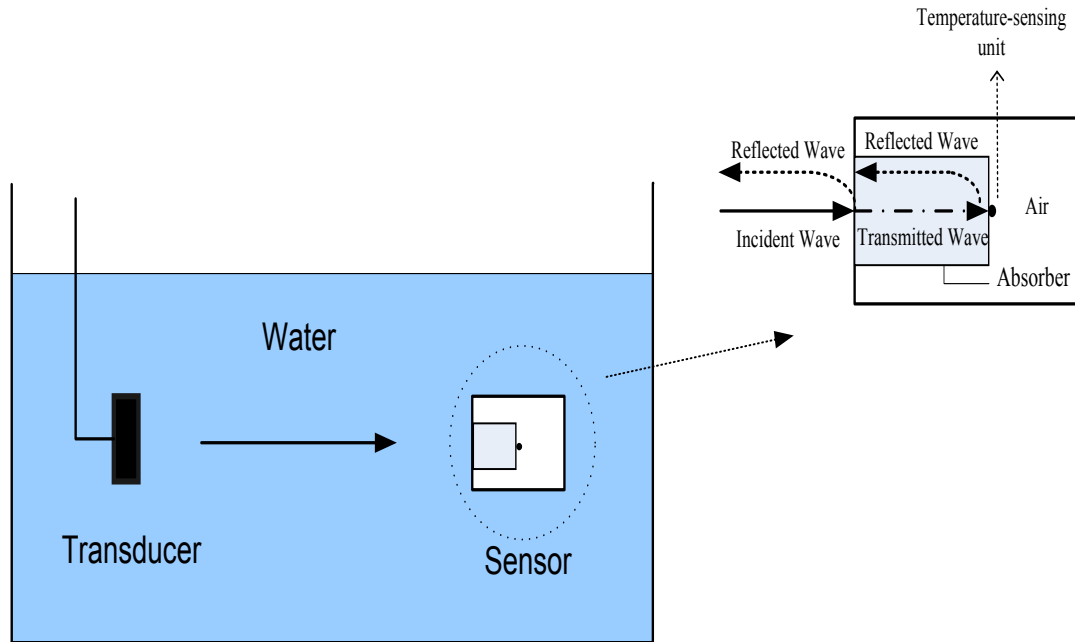


Figure 2.2: Schematic of the standard thermoacoustic sensor and its setup [40].

Standard thermoacoustic sensors employ a conventional beam-plotting set-up in a water tank. As shown in Figure 2.2, the conventional set-up requires a sizable water tank, large volume of degassed water, and time-consuming adjustment of the alignment between the transducer and the sensor for each time of use. Degassed water is usually processed through a series of steps including heating the distilled water for around one hour to remove residual gas, and waiting for another long period of time until the hot water cools down. In addition, the conventional beam-plotting set-up requires suspension and alignment of the sensor and transducer in the water tank. To achieve accurate positioning and

alignment, a mechanical positioning system is additionally requested. Without such a mechanical positioning system, it is quite difficult to totally align the absorber inside the sensor with the transducer in a water tank during each measurement. Any misalignment of the sensor's absorber with the transducer during a measurement compromises the accuracy of the sensor's measurement and makes it difficult to guarantee measurement consistency. However, a commercial positioning system or a customized positioning system further increases the cost of the system.

To simplify the set up procedure while maintaining measurement consistency during each measurement, a close-proximity thermoacoustic sensor was proposed to couple the sensor and the transducer together through ultrasound medium (ultrasound gel or degassed water) [68]. Such design tackles the difficulty of suspending and aligning the sensor and the transducer in a large water tank [39-42], enabling a much easier set up exempting from the use of a positioning system. Meanwhile, the consistency of measurements is guaranteed due to the fixed position of the sensor and the transducer for each time of use.

The close-proximity thermoacoustic sensor is shown in Figure 2.3. A transducer on top (black) and absorber in the middle (red) is coupled by a compartment of degassed water (blue) in the upper half of the sensor. The absorber attenuates the incident ultrasonic wave and converts the energy into heat, where the thermistor at the bottom of the absorber detects the change of temperature and sends the signal to measurement device outside. More specifically, to allow homogenous heat distribution, a layer of silver particles is

applied on the surface of the absorber to equally distribute the generated heat. While silver and copper are the two most commonly used materials for this purpose, silver was chosen in the design because it has a higher value of thermal diffusivity representing the ability of a material to redistribute heat. Silver has a thermal diffusivity of  $1.74 \times 10^{-4} \text{ m}^2/\text{s}$ , whereas copper has a value of  $1.15 \times 10^{-4} \text{ m}^2/\text{s}$  [69]. A micro thermistor (0.36mm in diameter, Honeywell Inc. Morristown, US) was chosen to measure the change of temperature because of its small size, fast response time and excellent long-term stability. The temperature increases measured by the thermistor are sent to an outside microcontroller (ATmega 324P, Atmel Corporation. San Jose, US) for recording and real-time processing. The thermistor is sealed in the sensor to remove any temperature influence from outside.

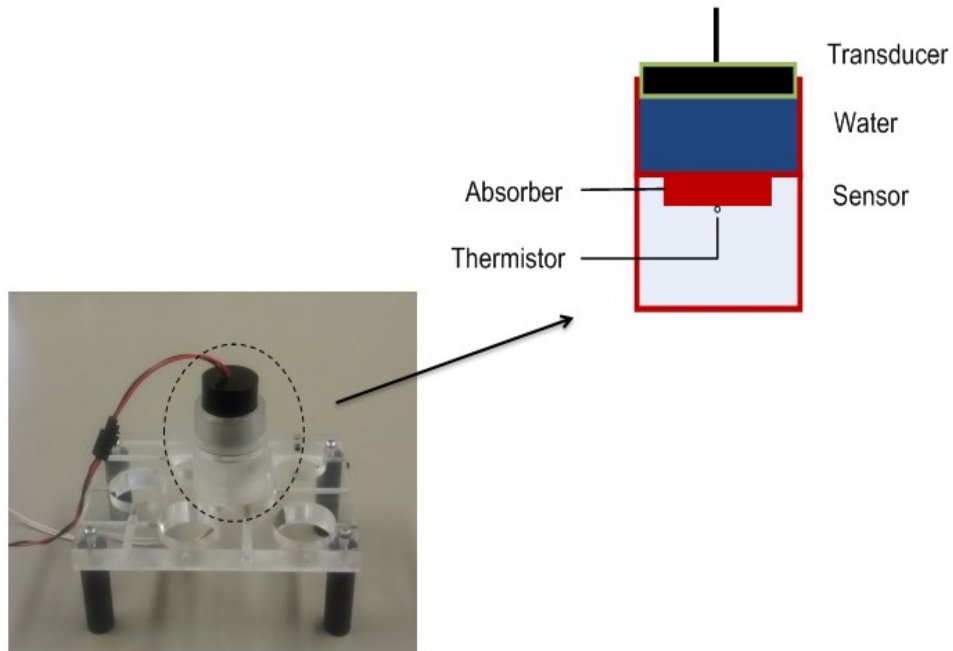


Figure 2.3: Close proximity setup of the thermoacoustic sensor. The sensor is placed in direct contact with the ultrasound transducer via degassed water as medium.

The "close proximity" nature of the sensor design makes the measurements be easily affected by the transducer's self-heating effect, which occurs when electrical energy is not fully converted to mechanical energy but partially turns into heat. The degassed water layer in between the transducer and the sensor largely mitigates the self-heating effect, where it not only works as coupling medium, but also disperses the heat generated by the transducer during measurements given its high specific heat capacity.

The selection of absorber material is important, because the acoustic impedances of the ultrasound medium (degassed water) and sensor will determine the amount of ultrasonic wave reflected at the water- interface, and the amount of wave transmitted through. Plexiglass is a low-cost material, which can be easily

processed with common mechanical machines. The acoustic impedance match between plexiglass and water is investigated to decide whether it is a good choice for the thermoacoustic sensor design. Acoustic properties of degassed water and plexiglass are shown in Table 2.1.

Table 2.1: Acoustic properties of ultrasound medium and plexiglass (20°C) [69-72].

Material	Attenuation Coefficient	Density	Speed of Sound in Media
Degassed Water	0.002 dB cm <sup>-1</sup> MHz <sup>-1</sup>	1000 kg/m <sup>3</sup>	1481 m/s
Plexiglass	1.13 dB cm <sup>-1</sup> MHz <sup>-1</sup>	1180 kg/m <sup>3</sup>	2730 m/s

Based on the acoustic properties from Table 2.1 and equation (2.3), the acoustic impedances of the plexiglass and water can be calculated, which are  $3.22 \times 10^6$  kg•m<sup>2</sup>/s and  $1.48 \times 10^6$  kg • m<sup>2</sup>/s, respectively. Using equation (2.4), the percentage of the ultrasound energy reflected at the boundary is calculated, which is 13.7%. That means 86.3% of the ultrasound wave can be transmitted into the sensor made by plexiglass. In addition, plexiglass has a relatively high attenuation coefficient of 1.13 dB cm<sup>-1</sup> MHz<sup>-1</sup>. Therefore, plexiglass was finally chosen as the material of this thermoacoustic sensor design, since it not only is low-cost and easy-to-process material, but also achieves good acoustic impedance matching and acoustic absorbance. The thickness of the sensor absorber is 2 mm, and its diameter is 20 mm.

## 2.2 Sensor Calibration and Algorithm Design

### 2.2.1 Calibration for Thermistor Data

After making the sensor, a quantitative relationship between the temperature of the sensor and the readout of the thermistor needs to be determined. The thermistor, as a temperature measurement unit, is a special resistor. Its resistance changes according to the temperature changes. The Honeywell thermistor used in this design is a negative temperature coefficient thermistor, which means the resistance of thermistor increases with the decline of the temperature. To find the relationship between the resistance of the thermistor and the temperature of the sensor, a calibration for the thermistor is required.

Thermistor calibration was carried out by placing the sensor in a heated water bath in order to record the value changes of the thermistor with respect to changes in temperature. The rising sensor temperature was recorded by a thermocouple with a sensitivity of 0.1°C, while the corresponding voltage value of the thermistor was measured and converted into a digital number through a microcontroller's analog to digital converter.

The measured thermistor data are shown in Figure 2.4. As indicated in the figure, a negative temperature coefficient can be observed from the thermistor data. To determine the quantitative relationship, a quadratic model is adopted to fit the thermistor data:

$$y(x) = ax^2 + bx + c \quad (2.6)$$

where  $y(x)$  is the sensor temperature ( $^{\circ}\text{C}$ ) and  $x$  is the digital readout of the thermistor.

MATLAB's curve fitting toolbox is used to find best estimates for the constants  $a$ ,  $b$ , and  $c$  in equation (2.6). The final parameter values obtained from curve fitting are  $a=2.25\times 10^{-6}$   $^{\circ}\text{C}$ ,  $b=-0.284$   $^{\circ}\text{C}$ ,  $c=91.42$   $^{\circ}\text{C}$ . Figure 2.4 shows the curve fitting results of the measurement data based on the quadratic model. Table 2.2 shows the parameters of curve fitting accuracy.

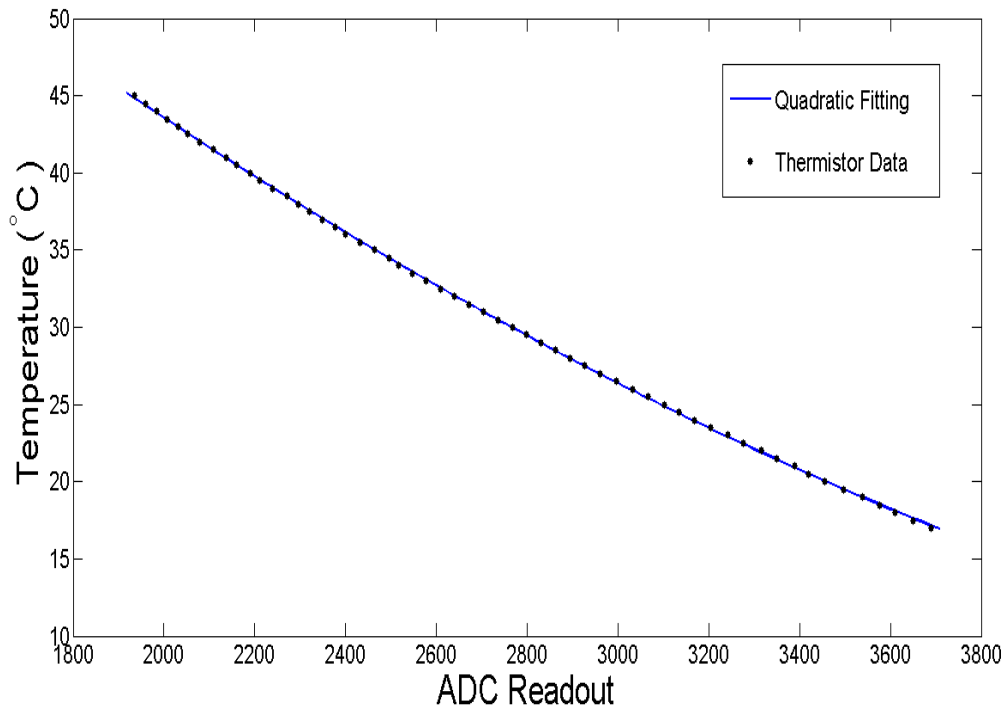


Figure 2.4: Thermistor curve fitting based on the quadratic model.

Table 2.2: Curve fitting accuracy of thermistor calibration.

	SSE	R-squared	RMSE
Quadratic Model	0.3335	0.9999	0.07859

SSE is the sum of squared errors of the best-fit curve: the smaller the SSE value, the better the model fits the data. R-squared represents the percentage of the sum of squares in a data set accounted for by the model. A value of R-squared equal to one indicates that the model fits the data perfectly. The root-mean-square error (RMSE) provides a measure of the difference between values predicted by the model and the observed values. From Figure 2.4 and Table 2.2, it is evident that the quadratic model exhibits excellent performance for thermistor data fitting.

### 2.2.2 Substitution Calibration

After thermistor calibration, the thermoacoustic sensor is able to measure the temperature changes induced by the applied ultrasound. For the sensor design to measure the applied ultrasound intensity, a substitution calibration procedure is required to correlate applied ultrasound intensities and temperature changes of the sensor. After the substitution calibration, the sensor is able to process the temperature data based on the correlation between temperature changes and applied ultrasound intensities and calculate the incident intensity.

The substitution calibration implemented after thermistor calibration includes two steps. First, a standard ultrasound measurement technique, such as a radiation force balance or a hydrophone, is employed to calibrate the ultrasound generator

device to desired ultrasound intensities. The ultrasound generator device was then applied to the thermoacoustic sensor to collect temperature data and correlate the sensor's temperature increases with the applied ultrasound intensities. The SonaCell ultrasound generator system was used in the calibration, which generates several rectangular waveform signals with a frequency of 1.5 MHz. The generated signal has a pulse repetition rate of 1 kHz and a duty cycle of 20%, which is converted to ultrasound waves through the transducer. A radiation force balance (UPM-DT-1AV, Ohmic Instruments, St. Charles, US) was used as the benchmark ultrasound measurement technique in the design to calibrate the ultrasound generator. The benchmark measurement device has a minimal measurement uncertainty of 3%.

The operation of the radiation force balance is according to the instruction of the user manual strictly [73]. The radiation force balance was placed in an environment free from vibrations, air currents, corrosives or magnetic fields. Degassed water was made by heating the distilled water for around one hour to remove the remaining gas. After the hot degassed water cooled down, the prepared degassed water was poured into the tank of the radiation force balance slowly to merge the cone target. The ultrasound transducer was also placed into the water tank above the center of the cone target so that the target can collect the whole ultrasonic beam for measurement. A short period of time is required for a force balance to settle down before starting the measurement. During the measurement, ultrasound generator is turned on until a stable reading is obtained by the radiation force balance. The measurement procedure is repeated as required.

It takes around 10~15 seconds for the radiation force balance to take a measurement and 10~20 seconds between measurements to wait for a force balance to settle down. The measurement result by the radiation force balance is the output power of the ultrasound transducer. To obtain the ultrasound intensity, the measured power was divided by the beam area of  $3.5 \text{ cm}^2$  generated by the transducer. The beam area was directly measured by a needle hydrophone system (Precision Acoustics Inc. Dorchester, UK) [74]. The ultrasound generator system was calibrated to intensities of 40, 60, 80 and  $100 \text{ mW/cm}^2$ .

The following step of the calibration was carried out using the designed thermoacoustic sensor. The sensor was coupled directly to the transducer of the ultrasound generator through the ultrasound medium to measure the temperature increase due to the applied ultrasound. The setup is shown in Figure 2.3. When the ultrasound was applied to the thermoacoustic sensor through the transducer, the temperature of the absorber began to increase. Under various ultrasound intensities, the temperature data over time were measured and recorded by the sensor. Figure 2.5 shows the temperature data over time measured by the thermoacoustic sensor at ultrasound intensities of 40, 60, and  $80 \text{ mW/cm}^2$ .

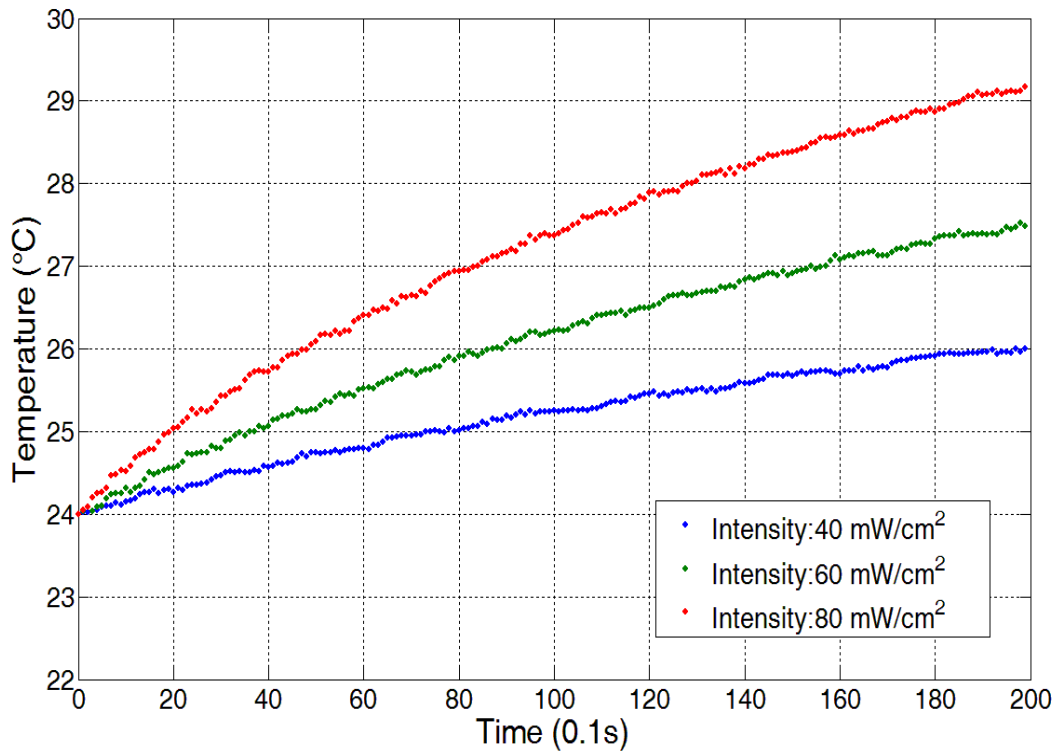


Figure 2.5: Temperature data over time at intensities of 40 mW/cm<sup>2</sup>, 60 mW/cm<sup>2</sup>, and 80 mW/cm<sup>2</sup>.

### 2.2.3 Approach for Relating Temperature Rise to Ultrasound Intensity

Once the temperature data are collected and correlated to the applied ultrasound intensities, the next step is to find the relationship between the sensor's temperature increases and applied ultrasound intensities. Almost all the previous thermoacoustic designs employed an equilibrium temperature approach to relate a temperature increase to an applied ultrasound intensity, which models the heat generated by ultrasound energy and the heat expelled to the surrounding medium [39-42]. When ultrasound wave propagates into the thermoacoustic sensor, the temperature of the absorber begins to increase because of the generated heat from the incident ultrasonic energy; meanwhile, part of the generated heat flows to the

water due to the direct contact between the sensor and water. After a while, a thermal equilibrium is reached in the absorber as long as the ultrasound intensity is constant, and the equilibrium temperature is proportional to the applied ultrasound intensity. Thus, the ultrasound intensity can be inferred from the equilibrium temperature.

Figure 2.6 shows a temperature vs. time curve of the sensor measured at intensity of  $40 \text{ mW/cm}^2$ . The ultrasound generator was turned on at time  $t = 0$ , and remained on throughout the whole measurement process. Temperature rises rapidly at the early stage of the curve between  $t = 0$  and  $t = 150$  seconds, after which the increase slows down, and finally reaches equilibrium at  $t = 400$  seconds. If the thermoacoustic sensor design uses the method of equilibrium temperature, the sensor's response time would be longer than 400 seconds, which prevents a rapid determination of ultrasound intensities. If the sensor design can implement an algorithm that relates the incident ultrasound intensity to the temperature rising trend at the very beginning of the temperature vs. time data curve, a rapid measurement of the applied ultrasound intensity would be possible. Myers and Herman proposed such a transient temperature model to describe the sensor's temperature increase induced by ultrasound energy and investigated it in a theoretical assessment [43].

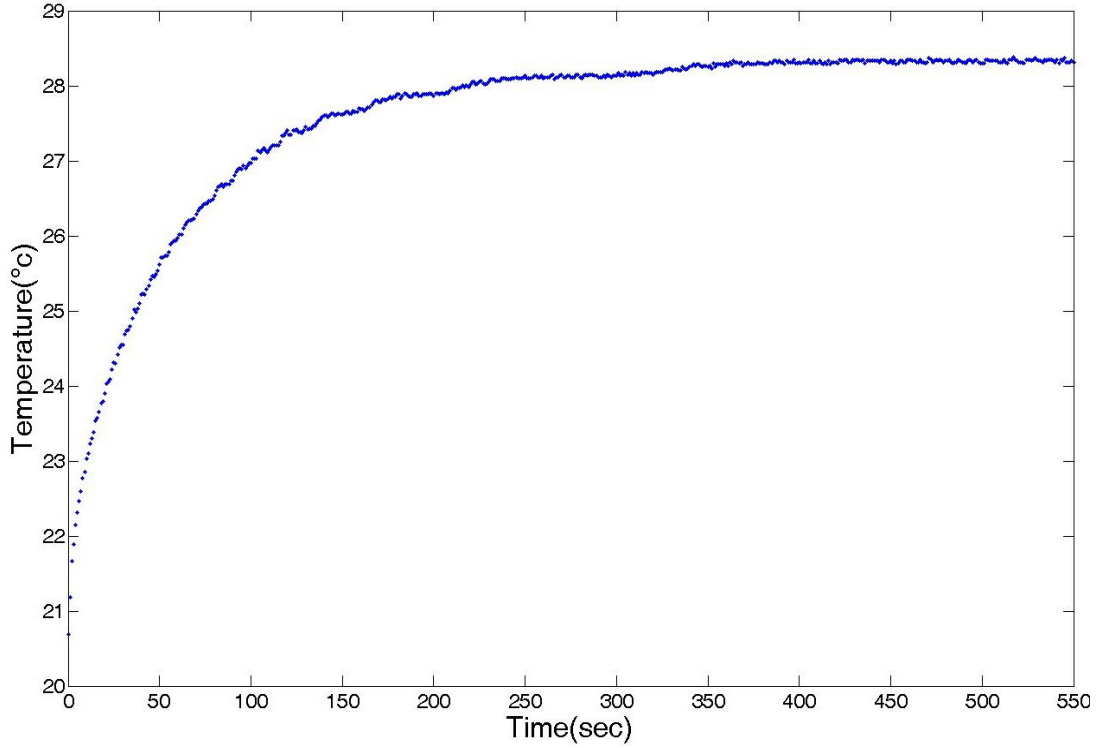


Figure 2.6: Temperature vs. Time curve measured by the sensor at  $40 \text{ mW/cm}^2$ .

The transient temperature model is built upon a single reflecting approximation, in which the ultrasound beam is transmitted through the absorber until being reflected at the back of it, and then returns to the water through the front face of the sensor [43]. They studied the parameters affecting the temperature rise in a cylindrical absorber in a theoretical assessment and built a transient energy equation. Finite-element and analytical solutions were obtained for the equation to describe the temperature rise over the absorber's cross-section, which is given by equation (2.7)

$$T_{\text{ave}}(t) = \sum_{n=0}^{\infty} \frac{16I_0}{k\pi\alpha} \frac{(1+e^{-2\alpha l})}{(2n+1)(4\alpha^2 l^2 + (2n+1)^2 \pi^2)} \left(1 - e^{-\frac{t}{\tau}}\right) \quad (2.7)$$

$$\tau = \frac{4l^2 \rho C}{(2n+1)^2 \pi^2 k} \quad (2.8)$$

In equation (2.7) and (2.8),  $T_{ave}(t)$  is the average temperature over the absorber's cross-section,  $I_0$  is the incident ultrasound intensity,  $\alpha$  is the absorption coefficient of the absorbing material,  $k$  is the thermal conductivity of the material,  $l$  is the length of the absorber,  $C$  is the heat capacity of the material, and  $\rho$  is the density of the material.

Using curve fitting approaches, parameters that represent the rise trend in temperature changes can be estimated, enabling a rapid determination of ultrasound intensity after calibration.

The equilibrium temperature approach and transient temperature profile are two methods for relating a temperature increase to the applied ultrasound intensity. Each method has its merits and demerits. The equilibrium temperature method, the most commonly used one, has the advantage of a simple measurement algorithm at the cost of a long equilibrium and measurement time. The sensor's transient temperature method, on the other hand, has the merit of a short measurement time at the cost of having a more complicated measurement algorithm.

#### **2.2.4 Transient Temperature Model**

To provide a rapid measurement, the transient temperature method describing the time dependent profile of the spatially averaged temperature at the

absorber's back face was investigated and evaluated in the sensor design. The first mode of transient profiles ( $n=0$ ) can be represented by equation (2.9).

$$T(t) = T_s + C \left( 1 - e^{-\frac{t}{\tau}} \right) \quad (2.9)$$

where  $T(t)$  is the measured temperature of the absorbing cylinder,  $T_s$  is the starting temperature,  $C$  represents the temperature-rise coefficient determined by the ultrasound intensity,  $\tau$  is a time constant determined during curve fitting procedure and  $t$  represents measurement time.

To evaluate the performance of the transient temperature model, the temperature data measured by the designed sensor at different intensities were used to fit the model. Figure 2.7 shows temperature data over time measured by the thermoacoustic sensor at ultrasound intensity of  $80 \text{ mW/cm}^2$ . The ultrasound intensity of  $80 \text{ mW/cm}^2$  is generated by the SonaCell generator and calibrated using a radiation force balance (UPM-DT-1AV, Ohmic Instruments).

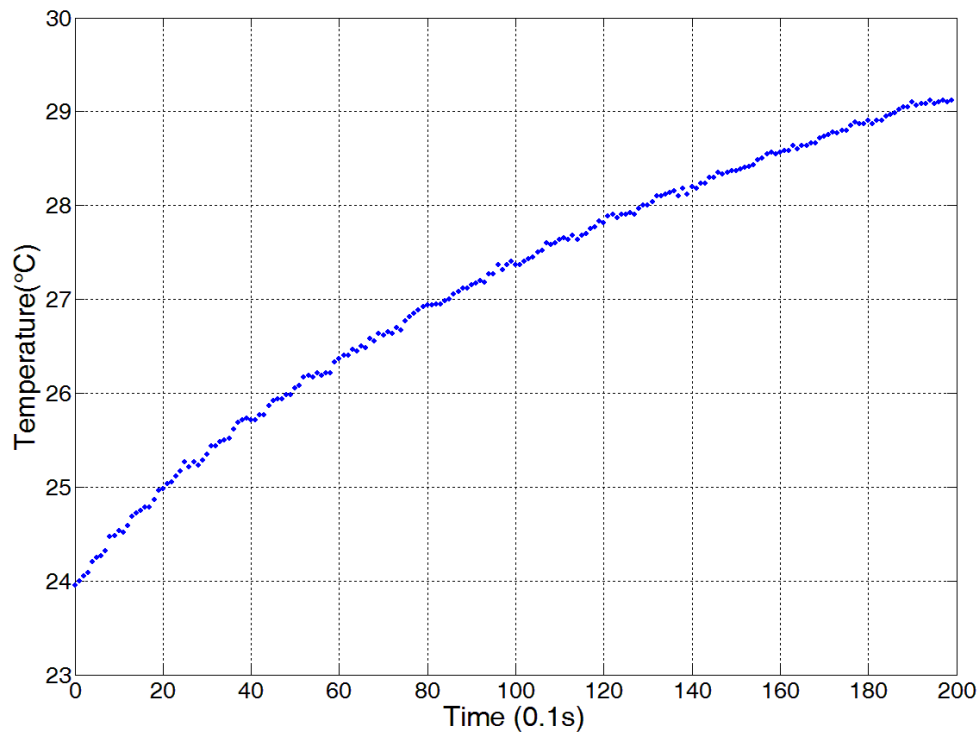


Figure 2.7: Temperature data over time measured by the thermoacoustic sensor under ultrasound intensity of  $80 \text{ mW/cm}^2$ .

The measured temperature data over time at intensity of  $80 \text{ mW/cm}^2$  were used to fit the first mode of transient profiles as shown in equation (2.9). MATLAB's curve fitting toolbox was employed to evaluate the curve fitting based on the measured data. The least squares fitting method was used during the process of curve fitting to find the optimum fitting curve by minimizing the sum of squared errors.

Figure 2.8 shows the curve fitting results for temperature increases in the sensor with the ultrasound intensity of  $80 \text{ mW/cm}^2$ . The curve based on equation (2.9) was fit to the measured temperature data with prediction bounds with 95% certainty (calculated using the MATLAB curve fitting toolbox). The 95%

confidence interval means that the mean value of the data will fall in the lower and upper boundaries of the model in probability distribution with 95% confidence. Table 2.3 shows the coefficients of the fitting curve based on equation (2.9), and Table 2.4 shows its curve fitting accuracy for the temperature rise data. From Figure 2.8 and Table 2.4, we conclude that the fitting curve based on equation (2.9) does conform to the measured temperature data at the ultrasound intensity of  $80 \text{ mW/cm}^2$ .

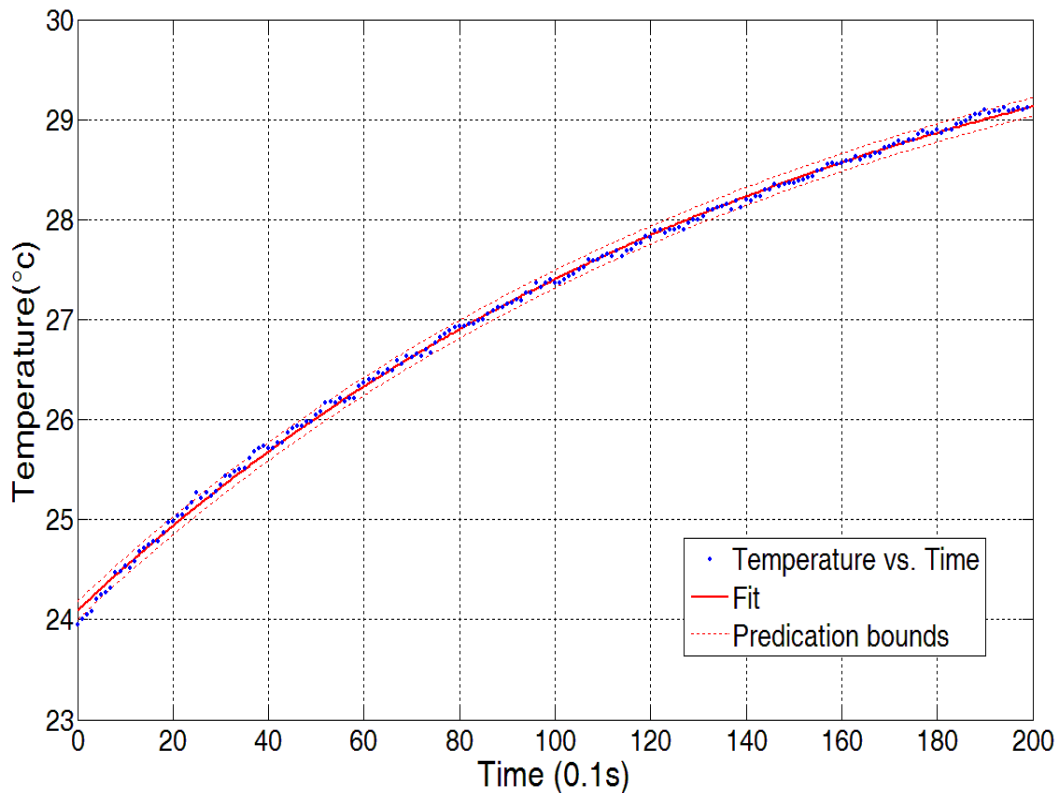


Figure 2.8: Temperature vs. time data measured by the thermoacoustic sensor for an applied ultrasound intensity of  $80 \text{ mW/cm}^2$ . Data was fit with equation (2.9) using the least squares model with prediction bounds with 95% certainty.

Table 2.3: Coefficients of the transient model for the applied ultrasound intensity of 80 mW/cm<sup>2</sup>.

Ultrasound Intensity [mW/cm <sup>2</sup> ]	Coefficient C (95% Confidence Bounds) [°C]	Coefficient $\tau$ (95% Confidence Bounds) [sec]	Coefficient T <sub>0</sub> (95% Confidence Bounds) [°C]
80	6.905 (6.813, 6.997)	153.1 (148.9, 157.2)	24.09 (24.07, 24.11)

Table 2.4: Accuracy of fit analysis for temperature data at 80 mW/cm<sup>2</sup>.

Ultrasound Intensity	Sum of Squares	R-Squared Value	Root Mean Squared Error
80 mW/cm <sup>2</sup>	0.4077	0.999	0.04549

Further evaluation was performed to test whether the transient model also fits temperature data measured at different ultrasound intensities other than 80 mW/cm<sup>2</sup>. Therefore, the MATLAB's curve fitting toolbox was also employed to fit to the measured temperature data at other ultrasound intensities. The curve fitting was performed based on the least squares fitting method. The curve fitting results for temperature data at 40 mW/cm<sup>2</sup> and 60 mW/cm<sup>2</sup> are shown in Figure 2.9 and Figure 2.10, respectively. The curve based on equation (2.9) was fit to the measured temperature data with prediction bounds of 95% certainty. Table 2.5 shows the curve fitting accuracy for the temperature data at intensities of 40 mW/cm<sup>2</sup> and 60 mW/cm<sup>2</sup>. From the Table 2.5, Figure 2.9 and Figure 2.10, the curve fitting accuracy based on equation (2.9) for the temperature data at different

intensities was confirmed again, which validates the feasibility of the transient temperature model in this sensor design. The applied ultrasound intensity can be related to the temperature-rise coefficient  $C$  obtained through the curve fitting, which enables the sensor to quickly estimate the applied ultrasound intensity given the transient temperature increase.

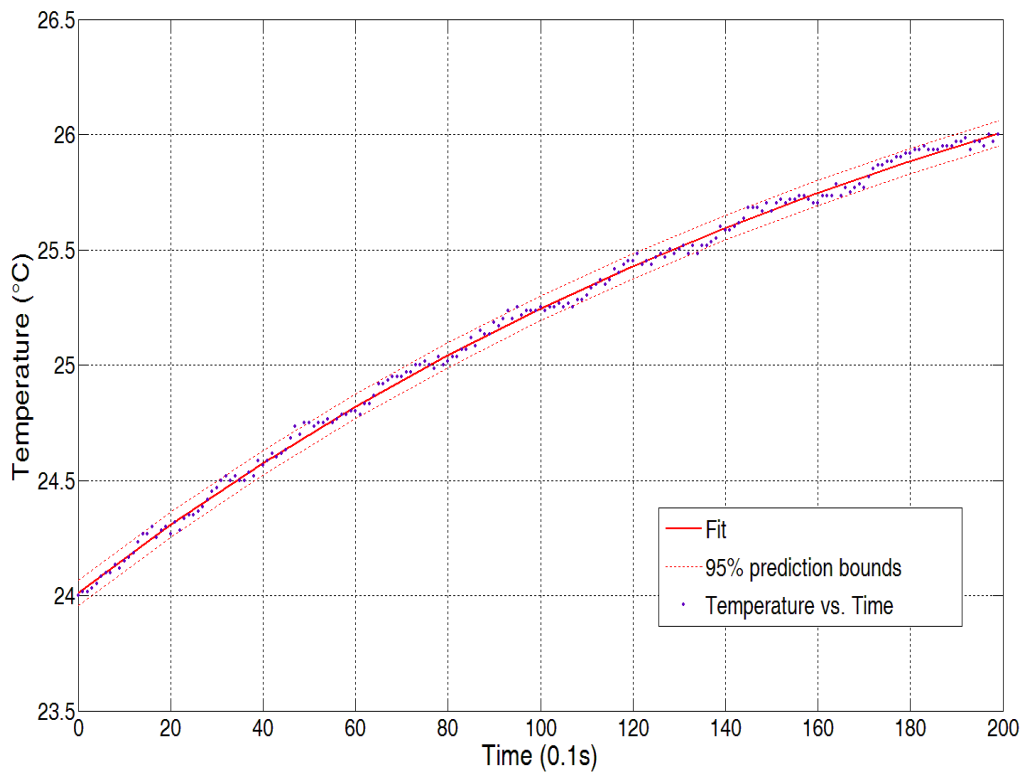


Figure 2.9: Temperature vs. time data measured by the thermoacoustic sensor at ultrasound intensity of  $40 \text{ mW/cm}^2$ .

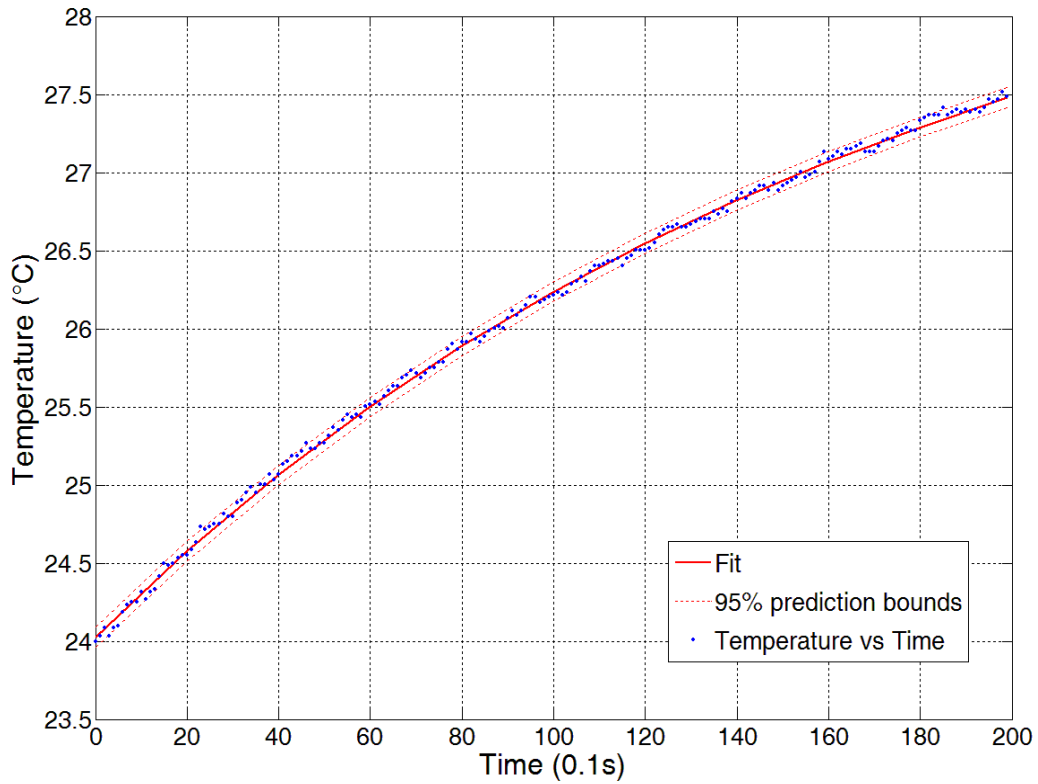


Figure 2.10: Temperature vs. time data measured by the thermoacoustic sensor at ultrasound intensity of  $60 \text{ mW/cm}^2$ .

Table 2.5: Accuracy of fit analysis for data for applied ultrasound intensities of  $40 \text{ mW/cm}^2$  and  $60 \text{ mW/cm}^2$ .

Ultrasound Intensity	Sum of Squares	R-Squared Value	Root Mean Squared Error
$40 \text{ mW/cm}^2$	0.146	0.998	0.0272
$60 \text{ mW/cm}^2$	0.199	0.999	0.0318

### **2.2.5 Relationship Between Coefficient C and Ultrasound Intensity**

Based on the substitution calibration procedure, the thermoacoustic sensor was calibrated to build the mathematical relationship between the recorded temperature data of the sensor and the applied ultrasound intensity. Using the least squares curve-fitting method, a series of parameters  $C$  representing temperature rise trend can be derived from the recorded temperature data. Since the value of  $\tau$  also influences the value of  $C$  during the curve fitting procedure, a fixed  $\tau$  must be determined during the curve fitting to get a series of correlated  $C$  values. The optimum value of constant  $\tau=130$  was determined experimentally and applied in the curve fitting procedure. The values of the coefficient  $C$  related to different intensities with various starting ambient temperatures were obtained based on the curve fitting of temperature data. Figure 2.11 depicts the relationship between the calculated  $C$  coefficient and the applied ultrasound intensity.

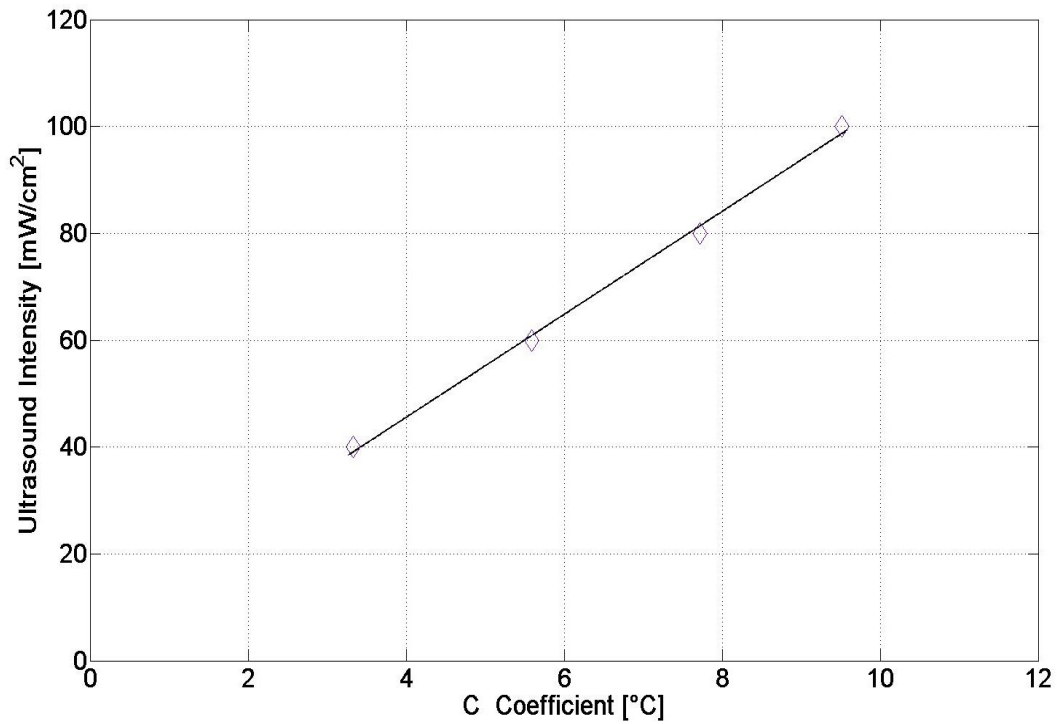


Figure 2.11: Linear relationship between applied ultrasound and the calculated  $C$  coefficient.

A linear relationship between the applied ultrasound intensities and the  $C$  coefficients can be observed from the data shown in Figure 2.11, which proves the validity of the transient temperature model method to build the relationship between the transient temperature rise of the sensor and the applied ultrasound intensity. A linear curve fitting is performed to evaluate the linearity between the applied ultrasound intensity ( $I$ ) and the calculated coefficient ( $C$ ). Equation (2.10) shows the linear relationship.

$$I = 9.637 \times C + 6.973 \quad (2.10)$$

## 2.2.6 Effect of Ambient Temperature

The thermoacoustic sensor's operation relies on the accurate quantitation of the temperature changes generated from the absorbed ultrasonic energy. Through the measurement of temperature increases, the ultrasound intensity can be determined by fitting transient temperature model [43, 68]. However, the sensor's temperature changes not only depend on the ultrasound intensity, but also are affected by the ambient temperature. Although the thermistor in the sensor is insulated to remove the influence from the outside room temperature, the front face of the sensor is still affected by the ambient temperature. The ambient temperature in the sensor design is the temperature of ultrasound medium shown in Figure 2.3. With different starting ambient temperatures, the temperature curves of the sensor are not the same even when the incident ultrasound intensity is the same. Figure 2.12 shows two temperature curves with different ambient temperatures at the same intensity of  $100\text{mW}/\text{cm}^2$ . Large differences can be observed from the figure. One temperature curve under ambient temperature of  $22.0^\circ\text{C}$  started at  $24.4^\circ\text{C}$  and ended at  $30.8^\circ\text{C}$  with an increment of  $6.4^\circ\text{C}$  in 20 seconds, while the other curve under ambient temperature of  $24.0^\circ\text{C}$  started at  $24.4^\circ\text{C}$  and ended at  $31.5^\circ\text{C}$  with an increment of  $7.1^\circ\text{C}$  in 20 seconds. As indicated in the figure, the ambient temperatures significantly impact the measured temperature curve, which would finally impair the measurement accuracy of the sensor.

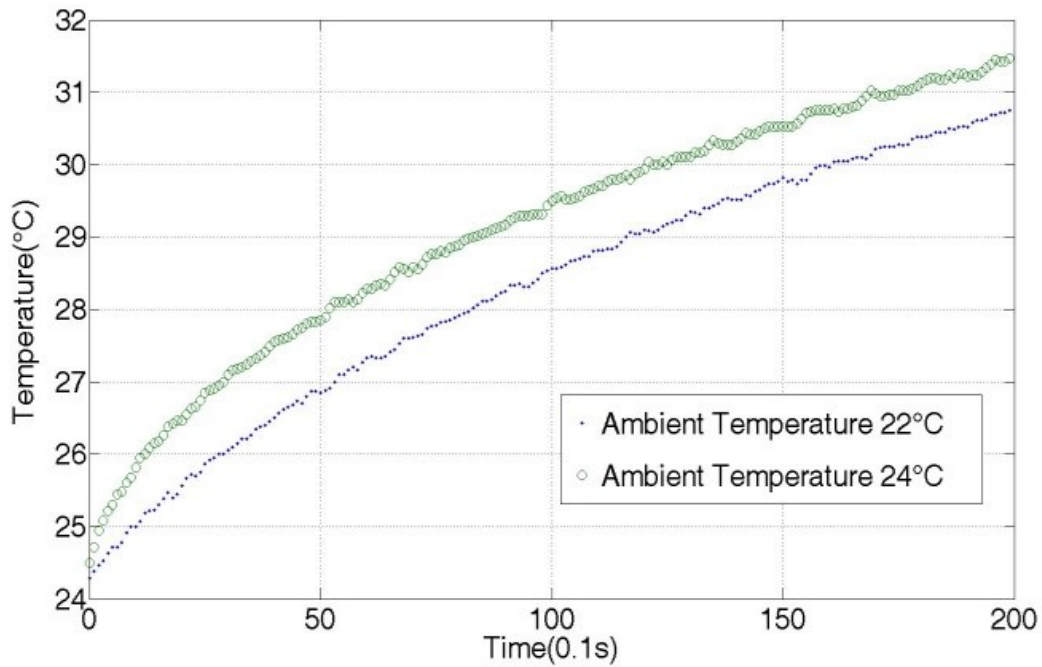


Figure 2.12: The sensor's temperature curves at ambient temperature 22°C and 24°C under the same ultrasound intensity 100 mW/cm<sup>2</sup>.

To make the measurement results accurate and consistent, the effect of ambient temperatures should be taken into consideration for the thermoacoustic sensor design. A range of measured temperature data with different ambient temperatures were used to examine their effect on the value of the  $C$  coefficient. Table 2.6 outlines the measured  $C$  value at different starting ambient temperatures between 21°C and 26°C under the same ultrasound intensity of 60 mW/cm<sup>2</sup>. The difference between the  $C$  values at various starting temperatures indicates that a direct correlation between measured  $C$  coefficient values and starting ambient temperatures. Figure 2.13 shows the relationship between starting ambient temperatures and coefficient  $C$  values. The linear relationship was found through

the curve fitting. From the figure, a good linearity between starting ambient temperature and C value for the intensity can be observed.

Table 2.6: Calculated *C* coefficients at various ambient temperatures.

	21.0°C	22.0°C	23.0°C	24.0°C	25.0°C	26.0°C
C Value [°C]	3.21	4.08	4.66	5.59	6.25	6.91

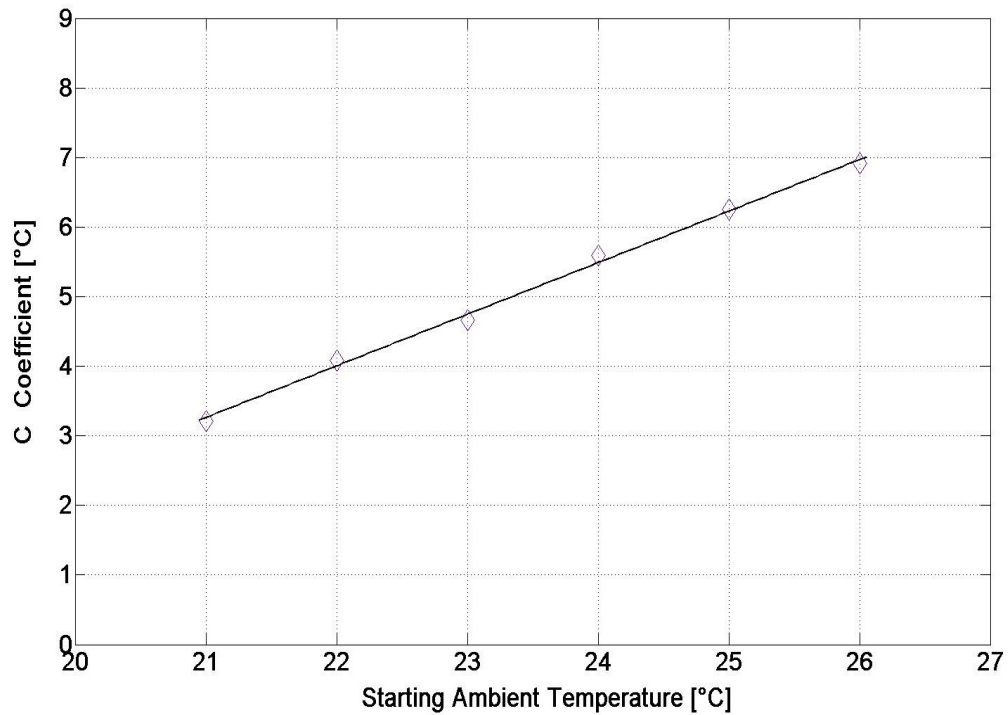


Figure 2.13: Linear relationship between starting ambient temperatures and the calculated *C* coefficient under intensity of 60 mW/cm<sup>2</sup>.

### 2.2.7 Sensor Algorithm

After obtaining a series of correlated  $C$  values at certain ultrasound intensities and ambient temperatures through calibration, the next step is to make the sensor recognize arbitrary ultrasound intensity at a random ambient temperature based on the calibration values. The final version of the thermoacoustic sensor was calibrated using substitution calibration methods, which took the effect of ambient temperatures into consideration. A temperature compensation method through extrapolation or interpolation based on the calibration values was used to estimate the applied ultrasound intensities. The linear fitting was carried out under different intensities to find the influence of the ambient temperatures to the value of the coefficient  $C$ .

Equation (2.11), (2.12), (2.13) and (2.14) are the linear fitting equations for ultrasound intensity 100, 80, 60 and 40 mW/cm<sup>2</sup> respectively.

$$C_1 = 0.714 \times T - 7.67 \quad (2.11)$$

$$C_2 = 0.767 \times T - 10.75 \quad (2.12)$$

$$C_3 = 0.747 \times T - 12.4 \quad (2.13)$$

$$C_4 = 0.569 \times T - 10.40 \quad (2.14)$$

After the calibration, the algorithm was designed and implemented to realize the function of the thermoacoustic sensor based on the above equations. When no ultrasound energy is applied to the sensor, the temperature that the sensor measured is the starting ambient temperature, since the ultrasound medium is in

contact with the absorber and their temperatures are the same. The program in the microcontroller can monitor the temperature changes and decide when to start a new measurement and record the starting ambient temperature. When ultrasound is applied, there will be obvious temperature increases in the sensor, and the starting ambient temperature before the obvious temperature changing is recorded. With the recorded starting ambient temperature, the equations (2.11), (2.12), (2.13) and (2.14) are used to calculate the values of coefficients  $C_1$ ,  $C_2$ ,  $C_3$  and  $C_4$  at the ambient temperature, which correspond to ultrasound intensities of 100, 80, 60 and  $40\text{mW/cm}^2$ , respectively. Meanwhile, the coefficient  $C$  related to the applied ultrasound intensity can be calculated through curve fitting of the measured temperature data based on the transient temperature model. After the value of coefficient  $C$  is obtained, the calculated values of coefficients  $C_1$ ,  $C_2$ ,  $C_3$  and  $C_4$  are compared with the obtained value of  $C$  to choose two parameters among them with closer values. Through interpolation or extrapolation based on the two chosen parameters and their correlated ultrasound intensities, the applied ultrasound intensity related to  $C$  can be finally evaluated based on the algorithm. The algorithm flowchart of the thermoacoustic sensor design is shown in Figure 2.14

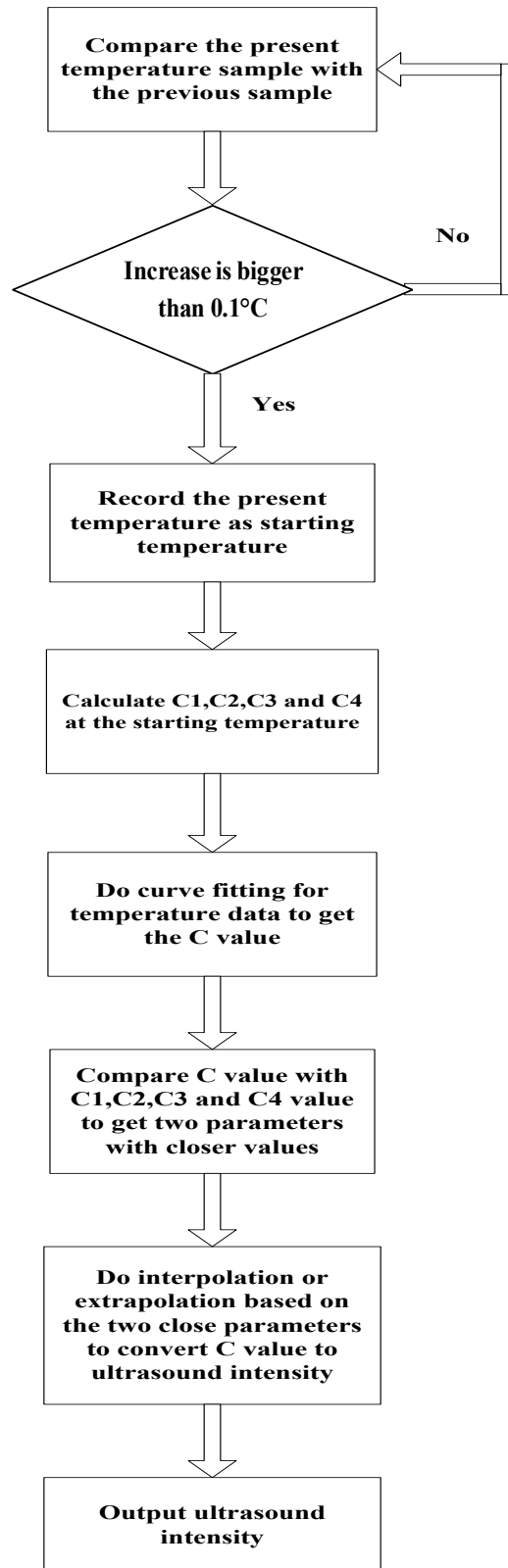


Figure 2.14: The thermoacoustic sensor's algorithm flowchart.

## **2.3 Sensor Performance Evaluation**

### **2.3.1 Ultrasound Medium Temperature**

In the sensor design, a small compartment was designed to hold a layer of ultrasound medium, which helps the ultrasound beam to transmit from the transducer to the absorber of the sensor. In addition to the coupling function, the medium layer also works as a buffer to distribute the heat generated by the transducer itself. The heating problem of the transducer comes from the energy lost during the conversion from electrical energy to acoustic energy. Without the medium layer, the generated heat by the transducer will flow to the sensor directly and greatly affect the sensor's measurement accuracy. Although the medium layer works as a buffer to distribute the generated heat of the transducer, its temperature should be carefully monitored and evaluated when ultrasound is applied, since any big temperature drift of the ultrasound medium will also influence the sensor's temperature measurement and eventually affect the accuracy of the measurement results. To monitor the temperature condition of the medium layer, a thermocouple was placed in the compartment when ultrasound was applied. Figure 2.15 shows the temperature condition of the coupling medium under intensity of  $100 \text{ mW/cm}^2$ .

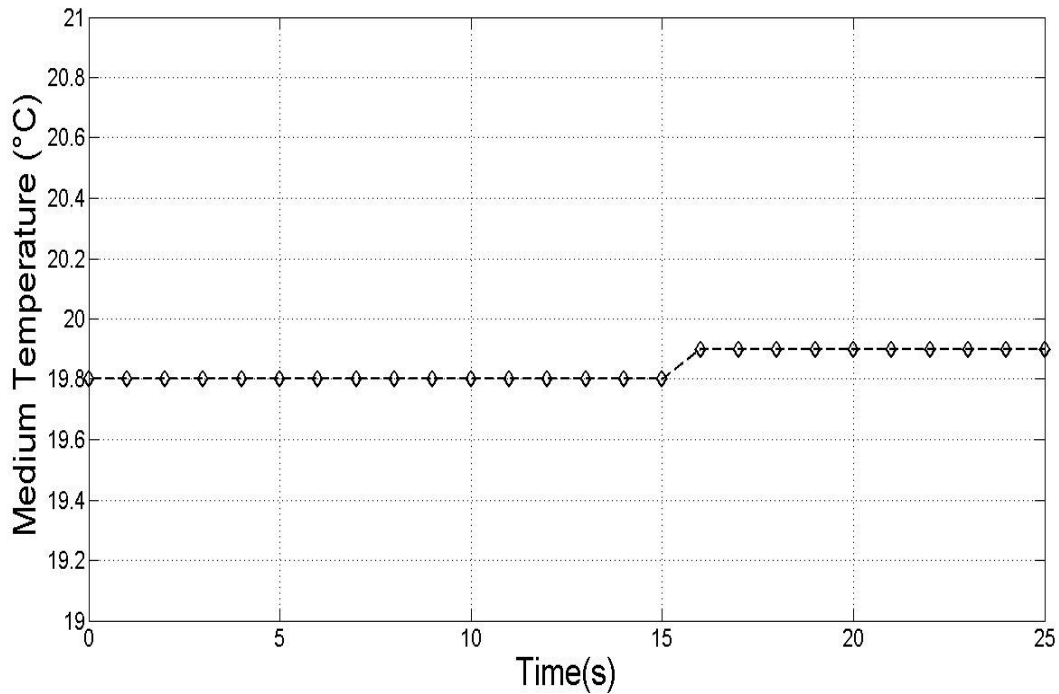


Figure 2.15: Temperature drift of the coupling medium under intensity of  $100 \text{ mW/cm}^2$ .

From the figure, we can observe that only  $0.1 \text{ }^\circ\text{C}$  temperature drift occurs in 25 seconds, which means the temperature of the ultrasound medium layer is very stable when ultrasound is applied. Compared to the big temperature rise in the sensor due to ultrasonic energy, the tiny temperature drift would not affect the sensor's measurement accuracy and its influence can be ignored.

### 2.3.2 Sensor Response Time

The design goal of the thermoacoustic sensor is to output an accurate measurement result of ultrasound intensity in a short response time. To evaluate the performance of the sensor design, the response time of the thermoacoustic

sensor were measured. The process evaluates the time for the sensor to get a reliable and accurate measurement result. Figure 2.16 shows the measurement error percentage of the sensor design at different time points under ultrasound intensity of  $40 \text{ mW/cm}^2$ . The error is the difference between the target intensity and the value measured by thermoacoustic sensors based on the curve fitting. By inspecting the errors in the figure, the response time required for the sensor to obtain a reliable measurement can be decided. The result shows that it takes around 20 seconds for the sensor to obtain a reliable measurement.

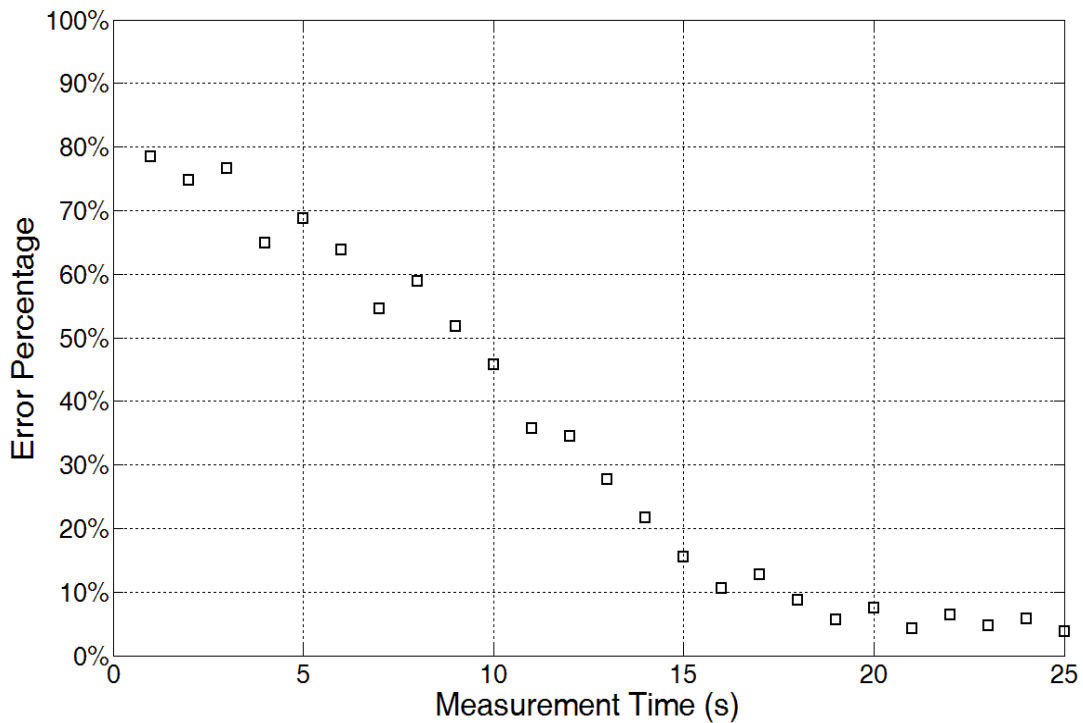


Figure 2.16: Response time of the thermoacoustic sensor with respect to measurement error percentage.

To further evaluate the improvement of the thermoacoustic sensor design in term of response time, the measure time using the transient temperature approach and the equilibrium temperature approach is compared based on the measured temperature data over time. Figure 2.17 shows the temperature rise curve measured by the thermoacoustic sensor at the ultrasound intensity of  $40 \text{ mW/cm}^2$ . The thermoacoustic sensor design utilizing the transient temperature approach can provide a reliable measurement in 20 seconds, whereas it takes more than 400 seconds to obtain a measurement if the thermoacoustic sensor design adopts the equilibrium temperature approach. The figure demonstrates that the sensor design using transient temperature approach can provide a rapid measurement of the applied ultrasound intensity, which greatly shortens the response time of the sensor compared to the equilibrium temperature approach.

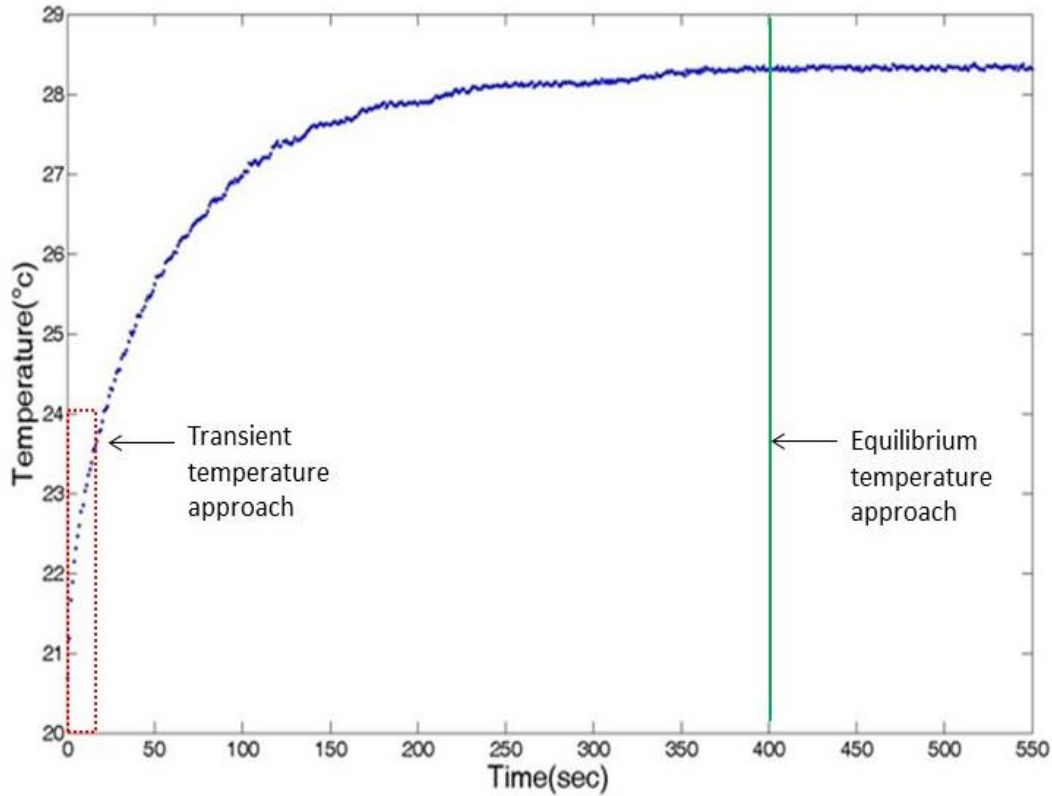


Figure 2.17: Response time of the thermoacoustic sensor design based on the transient temperature approach and the equilibrium temperature approach.

### 2.3.3 Intensity Measurement Result

The program based on the algorithm design was written into the microcontroller of the system to realize the sensor's function. The algorithm relates the applied ultrasound intensities to the  $C$  coefficients calculated from the measured temperature data through curve fitting. To test the measurement accuracy of the designed sensor, the radiation force balance was employed as a standard technique to evaluate its performance. By comparing readings taken

through a radiation force balance to the ones taken by the thermoacoustic sensor, the agreement between both techniques was examined.

The SonaCell ultrasound generator is calibrated by the radiation force balance (UPM-DT-1AV, Ohmic Instruments) in an environment without noise vibrations in order to generate ultrasound intensities of 30, 40, 60, 80, 100 and 120 mW/cm<sup>2</sup>. The output intensities were then measured by the thermoacoustic sensor. Table 2.7 shows measurement results of ultrasound intensities taken by the thermoacoustic sensor design. Table 2.8 compares the measurements obtained by the radiation force balance and the thermoacoustic sensor. The measurement results are plotted in Figure 2.18 for a better comparison and evaluation. In the figure, the linear fit represents a 1:1 relationship between the radiation force balance and the thermoacoustic sensor. The results show linearity between ultrasound intensity readings taken using a radiation force balance and measurements taken using the thermoacoustic sensor. The thermoacoustic sensor had an output with an average error of 3.97 mW/cm<sup>2</sup> across 18 measurements. The root-mean-square error (RMSE) of the measurement results is 4.49.

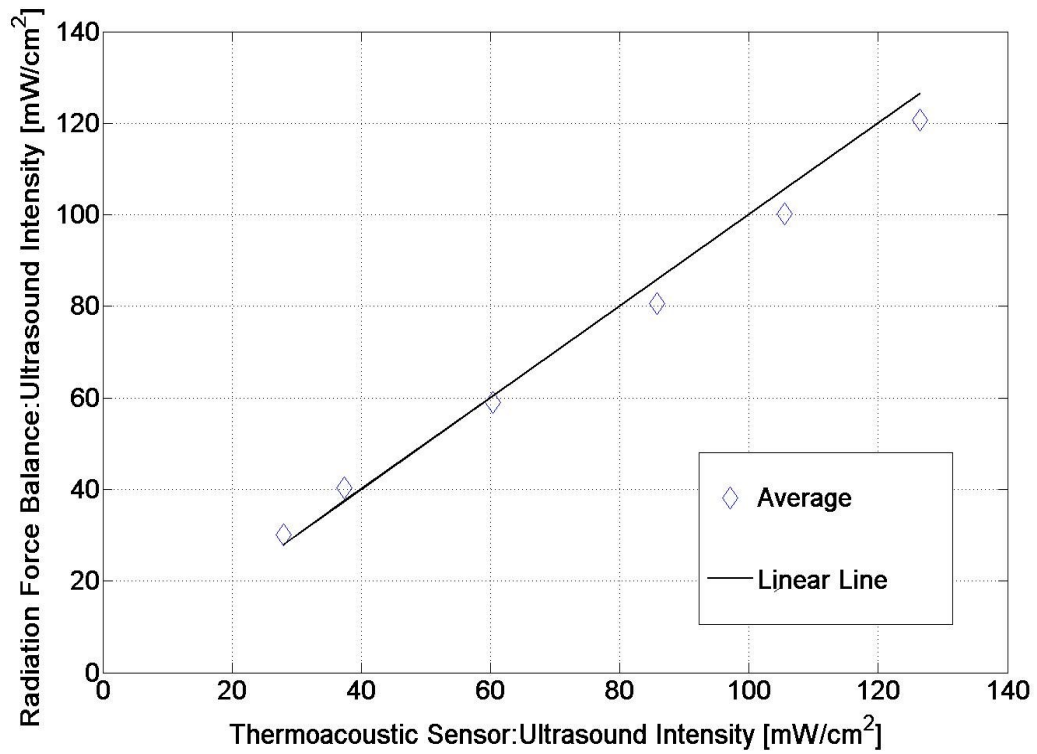


Figure 2.18: Evaluation of the thermoacoustic sensor by comparing measurements made with the thermoacoustic sensor with measurements taken using a radiation force balance. The linear line represents a 1:1 relationship between the Radiation Force Balance and the Thermoacoustic Sensor.

Table 2.7: Thermoacoustic sensor measurements.

		Measurements			
	Target [mW/cm <sup>2</sup> ]	#1 [mW/cm <sup>2</sup> ]	#2 [mW/cm <sup>2</sup> ]	#3 [mW/cm <sup>2</sup> ]	Average [mW/cm <sup>2</sup> ]
1	30	26.84	28.72	28.47	28.01
2	40	37.38	36.94	37.80	37.37
3	60	59.59	61.19	62.90	60.32
4	80	86.11	85.40	85.76	85.76
5	100	105.01	105.86	105.65	105.51
6	120	126.72	125.23	127.34	126.43

Table 2.8: Comparison between measurements made using a radiation force balance and measurements made using a thermoacoustic sensor.

	Radiation Force Balance	Thermoacoustic Sensor	Error
1	30.14 mW/cm <sup>2</sup>	28.01 mW/cm <sup>2</sup>	7.07%
2	40.28 mW/cm <sup>2</sup>	37.37 mW/cm <sup>2</sup>	7.22%
3	59.09 mW/cm <sup>2</sup>	60.32 mW/cm <sup>2</sup>	2.08%
4	80.58 mW/cm <sup>2</sup>	85.76 mW/cm <sup>2</sup>	6.43%
5	100.25 mW/cm <sup>2</sup>	105.51 mW/cm <sup>2</sup>	5.25%
6	120.73 mW/cm <sup>2</sup>	126.43 mW/cm <sup>2</sup>	4.72%

## 2.4 Discussion

A low-cost and easy-to-operate thermoacoustic sensor was designed, implemented and investigated for ultrasound intensity measurement. In this chapter, the prototype design has been demonstrated to measure ultrasound operating at 1.5 MHz frequency in low intensity range (30 mW/cm<sup>2</sup> to 120 mW/cm<sup>2</sup>), which is widely applied to biology experiments. The thermoacoustic sensor measures the temperature changes caused by incident ultrasound energy to determine the ultrasound intensity. To rapidly relate temperature rise to ultrasound intensity, the measured temperature data of the sensor was evaluated through the transient temperature model. The curve fitting results showed that the model can fit the temperature increase data very well. From the curve fitting, the sensor was able to relate a curve fitting coefficient  $C$  to the applied ultrasound intensity. Different ultrasound intensity levels radiated by transducers were calibrated by a radiation force balance to find the relationship between calculated coefficient  $C$  and the applied ultrasound intensity. This relationship yielded a linear equation used to correlate the  $C$  coefficients to ultrasound intensities. The final intensity measurement results indicate a good agreement between the thermoacoustic sensor and the radiation force balance. Due to the linearity observed, it is expected that the sensor can measure intensities even greater than 120 mW/cm<sup>2</sup>.

Thermal sensors, due to the relatively simple structure, have the advantages of simplicity and low cost over the other techniques used to measure the ultrasound intensity. The sensor design based on the close-proximity sensor concept further simplifies the set-up procedure through connecting the sensor to

the transducer directly, which gets rid of the complicated set-up to suspend and align the sensor and the transducer in a large de-gassed water tank used in the previous sensor design. Compared to the standard technique of radiation force balance, the accuracy of which is easily influenced by background vibrations in biology laboratory environment, the measurement of thermoacoustic sensor is not affected by the vibration due to its design principle. This thermoacoustic sensor offers a convenient alternative to the radiation force balance for determining ultrasound output intensity. However, the drawback of the thermoacoustic sensor is that a calibration using the transducer is needed beforehand. It is worth noting that the measurement accuracy of the thermoacoustic sensor is related with the measurement uncertainties of the radiation force balance, since the radiation force balance was used as a reference acoustic calibration technique in the sensor design. The measurement uncertainties of the radiation force balance in this sensor design are  $\pm 3\%$ .

## **Chapter 3**

### **Improved Thermoacoustic Sensor Design**

In the previous chapter, a preliminary sensor design based on a transient temperature model for quick intensity measurement was introduced. To make the sensor easy to operate while maintaining consistency during each measurement, the sensor set-up procedure is simplified using a concept of close-proximity where the designed sensor is directly coupled to the transducer through degassed water to perform the measurements. The preliminary sensor design conducts measurement in only 20 seconds while maintaining the maximum measurement error within 11% across 18 measurements, thus providing an easy and efficient alternative to the conventional set-up. However, when using the proposed sensor for intensity calibration, an enhancement in response time, accuracy, and consistency of measurements is further required. This chapter focuses on how to improve the performance of the sensor through a new structural design and an artificial neural network algorithm [75].

#### **3.1 Sensor Design**

The thermoacoustic sensor determines the ultrasound intensity based on the temperature rise caused by the heat converted from incident acoustic energy. The performance of the thermal sensor heavily depends on the conversion efficiency from low intensity ultrasonic energy into heat. In the previous study, a single layer of plexiglass was used as the absorber because it is a low-cost material with easy-to-process mechanical properties and a relatively high attenuation coefficient.

However, it is not enough for absorbing of all incident acoustic energy. To achieve much greater measurement efficiency, further design modifications are required. If a second layer of material with a high attenuation coefficient is employed to absorb extra ultrasound energy, the energy absorption rate of the sensor will be greatly improved.

The energy absorption rate of the sensor is important for accurate and rapid estimation of ultrasound intensities because higher absorption rates indicate: (1) more reliable estimations based on the amount of captured energy, and (2) more rapid measurement readout due to faster energy conversion rates. We propose to use a two-layer structural design as well as better absorbing materials to increase the absorption efficiency of the thermoacoustic sensor. Figure 3.1 illustrates the structure of the new two-layer sensor.

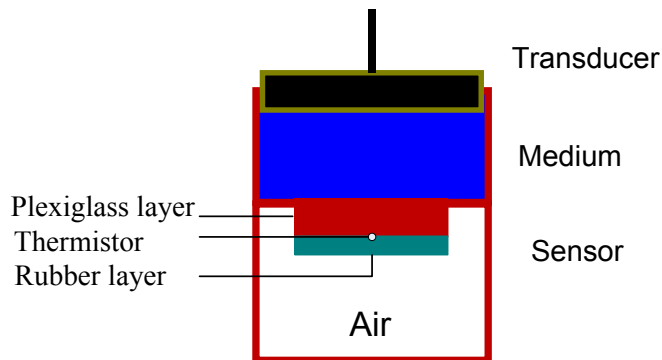


Figure 3.1: The structure of the two-layer thermoacoustic sensor.

For the new sensor design, the first layer is a cylindrical plexiglass absorber, the same as the previous design. Another absorber layer was added to the back of

the plexiglass layer, made of a highly attenuating polyurethane rubber APTFLEX F28 (Precision Acoustics Inc. Dorchester, UK) [76], in order to further increase the absorption of ultrasound energy. The thicknesses of the plexiglass and rubber layers are both 1mm, and the diameter of the absorber is 20 mm. The gap between the two absorber layers is filled with a very thin film of acoustically matched material APTFLEX F21 (Precision Acoustics Inc. Dorchester, UK). This film ensures that no air is trapped between the layers, since a large mismatch of the air and absorber impedance would reflect ultrasound waves before it enters the second layer of absorber. Two-layer design facilitates ultrasound to smooth transit from one layer to the next. This new sensor design adopts the close-proximity concept to simplify set-up procedures through the use of direct coupling between the sensor and transducer via a coupling medium as indicated in Figure 3.1. The micro thermistor (0.36mm in diameter, Honeywell Inc. Morristown, US) is used to measure temperature changes of the sensor. Silver particles are applied on the two-layer interface to equally distribute the generated heat around the thermistor. The temperature increase measured by the thermistor is sent to a microcontroller (ATmega 324P, Atmel Corporation. San Jose, US) for real-time processing and recording. The absorber is sealed in the sensor in order to reduce any outside interference. After sealing the absorber, the ultrasound medium temperature becomes the starting ambient temperature that affects the sensor's measurement accuracy, since the ultrasound medium is in contact with the absorber.

### **3.2 Simulation of Ultrasound Propagation in Sensor**

To evaluate the performance of the two-layer sensor, three-dimensional (3-D) simulation models of the ultrasound propagation was compared between the two-layer and the one-layer design using a K-wave toolbox (Version 1.1). The simulation computes the amount of ultrasonic energy absorbed by the sensors. K-wave is an open source Matlab and C++ toolbox designed for time domain ultrasound simulation in either 1-D, 2-D or 3-D domains, which can simulate ultrasound wave propagation including reflection, refraction and attenuation in both homogenous and heterogeneous media [77, 78].

K-wave is built on an advanced numerical model which is validated for both linear and nonlinear wave propagation simulation [79]. In the numerical model, a series of coupled first-order partial differential equations are built to describe acoustic changes when ultrasound propagates through a medium. Traditional numerical methods such as the finite-difference, finite-element, and boundary-element methods are available to solve the acoustic partial differential equations [77]. However, the traditional methods are bulky and slow for computers to calculate and simulate high-frequency acoustic wave propagation in the time domain, because their computations require that the continuous acoustic wave is divided into many discrete grid points in small time-steps to maintain simulation accuracy [79]. For instance, an ultrasound wave generated by a 3MHz curvilinear transducer has a penetration distance around 15 cm, which approximately equals to 600 wavelengths at the second harmonic. If the discretized approximation of 10 grid points per acoustic wavelength is used, more than  $10^{11}$  grid elements is

required in the 3-D computational domain, which needs several hundreds of gigabytes' computer memory to store and process each data matrix [79].

To reduce computation complexity and improve simulation efficiency, K-wave employs a k-space pseudo spectral method to solve the acoustic equations and implement the simulation [77]. The method uses a Fourier series to fit all the data and calculate spatial derivatives. The introduction of Fourier series improves efficiency, because fast Fourier transform (FFT) is able to provide a more efficient amplitude calculation and only two grid points per wavelength are needed due to its sinusoidal basis functions [77]. Through optimization of computational algorithm, K-wave provides a fast method to simulate the time evolution of an acoustic wave field without compromising accuracy. In addition, K-wave provides a wide selection of simulation functions, which brings convenience and flexibility for users to build models of acoustic wave propagation based on it.

The simulation in K-wave is implemented by dividing the built model into tiny computational grid points and computing the propagation of the wave field point by point. Therefore, the first step is to divide the computational domain and define the properties of the computational grids for models. Three Cartesian directions are represented by  $X$ ,  $Y$  and  $Z$  in the three-dimensional computational domain. Symbols  $dx$ ,  $dy$  and  $dz$  are used to define size of each grid in the  $X$ -direction,  $Y$ -direction and  $Z$ -direction, respectively. To accurately simulate ultrasound wave propagation, the size of grid should be chosen carefully. Based on the Nyquist limit of two grid points per acoustic wavelength, the maximum

supporting simulation frequency related to the grid size can be expressed by equation (3.1) [79].

$$f_{max} = \frac{c_{min}}{2dx} \quad (3.1)$$

where  $dx$  is the size of grid or the grid point spacing and  $c_{min}$  is the minimum value among different acoustic speeds when acoustic wave propagates through heterogeneous media .

The maximum size of computational grid supporting a simulation frequency of  $f_{max}$  can be derived from equation (3.1), which is given by equation (3.2).

$$dx = \frac{c_{min}}{2f_{max}} \quad (3.2)$$

Using the equation (3.2), the maximum size of computational grid can be calculated from the simulation frequency and the minimum acoustic speed. The simulation is based on an acoustic frequency of 1.5 MHz. The minimum acoustic speed occurs when ultrasound propagates through air as shown in Table 3.1, which is 343 m/s. Therefore, the maximum size of grid can be calculated, which is equal to 0.113mm. To guarantee the simulation accuracy, a grid spacing used in the simulation must be smaller than the maximum grid size of 0.113mm. In the simulation, a high-resolution grid spacing of 0.05mm was chosen in the ultrasound propagation direction.

$N_x$ ,  $N_y$  and  $N_z$  represent the number of grid points in the  $X$ -direction,  $Y$ -direction and  $Z$ -direction, and the total number of grid points in the three-dimensional computational domain is  $N_x \cdot N_y \cdot N_z$ . Since the total size of the

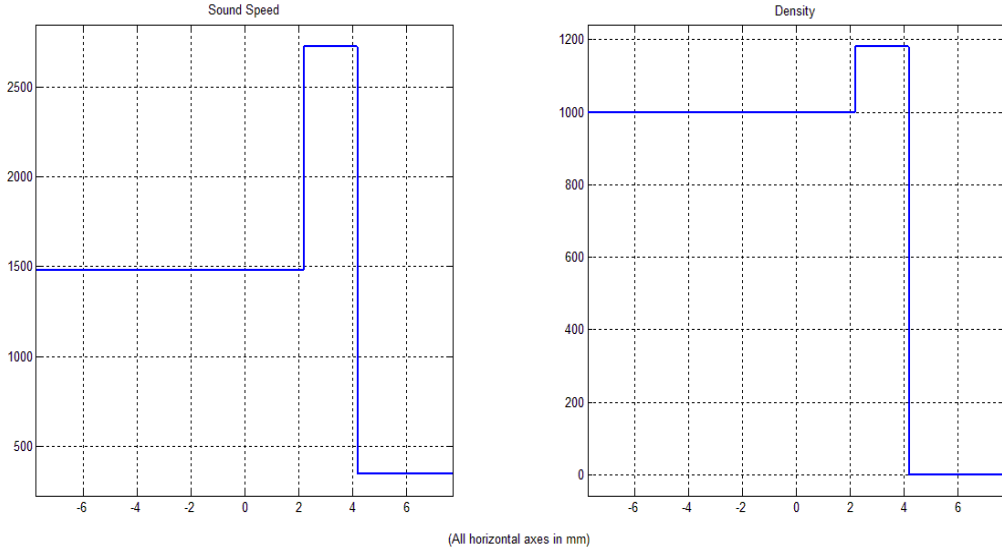
computational domain in the  $x$ -direction  $X_{size}$  equals to  $Nx \cdot dx$ , according to the real dimension of computational domain in the  $X$ -direction, the number of grid points in the  $x$ -direction  $Nx$  can be calculated. Similarly, the number of grid points in the  $Y$ -direction and  $Z$ -direction,  $Ny$  and  $Nz$ , can also be determined through calculation. Finally, the number of grid points in the three-dimensional computational domain is set to be  $256 \times 256 \times 256$  for the simulation.

The properties of medium and materials are required to set for the models in k-wave simulation, after the dimension of computational domain and the size of computational grid for the models are determined. The medium setting defines the acoustic properties of the medium or material at each grid point, which includes sound speed, material density and attenuation coefficient. Table 3.1 lists the acoustic properties of the media and materials included in the 3-D models.

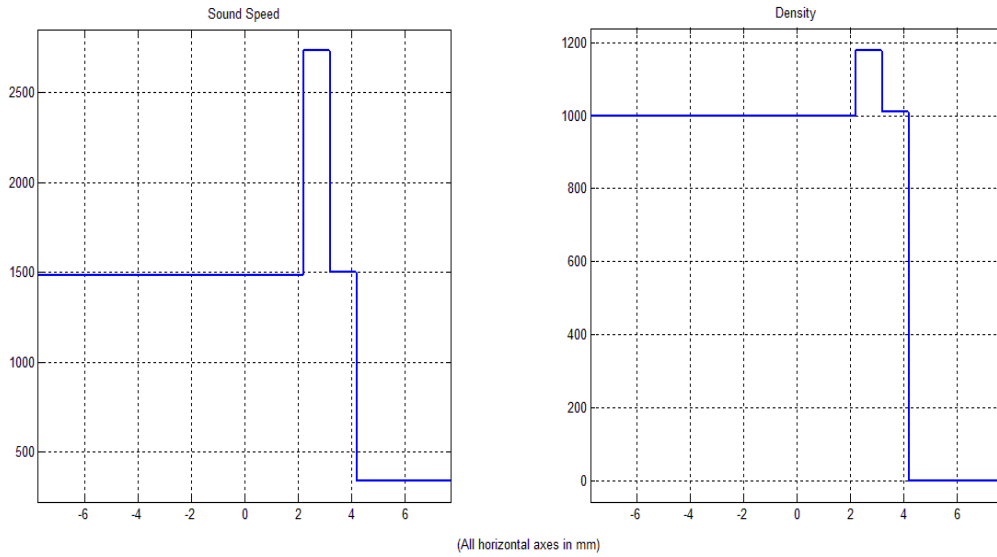
Table 3.1: Acoustic properties of media and materials (20°C) [69-72, 76].

Material	Attenuation Coefficient	Density	Speed of Sound in Media
Ultrasound Medium	0.002 dB cm <sup>-1</sup> MHz <sup>-1</sup>	1000 kg/m <sup>3</sup>	1481 m/s
Air	1.64 dB cm <sup>-1</sup> MHz <sup>-1</sup>	1.204kg/m <sup>3</sup>	343 m/s
Plexiglass	1.13 dB cm <sup>-1</sup> MHz <sup>-1</sup>	1180 kg/m <sup>3</sup>	2730 m/s
Polyurethane Rubber	30 dB cm <sup>-1</sup> MHz <sup>-1</sup>	1010 kg/m <sup>3</sup>	1500 m/s

The 3-D models for the one-layer and two-layer sensors were separately built based on sensor structure, acoustic properties of media and materials used in the designs. For the one-layer sensor model, the ultrasound wave propagates through the ultrasound medium and plexiglass absorber, and then reflects back at the absorber-air interface whereas, in the two-layer sensor model, the ultrasound wave propagates from the first plexiglass layer to a second polyurethane layer after transmitting from the ultrasound medium into the sensor. Figure 3.2 illustrates the distributions of the medium parameters for the one-layer and two-layer sensor models in the ultrasound propagation direction.



(a)



(b)

Figure 3.2: The distributions of the medium and material parameters for sensor models in the ultrasound propagation direction. (a) The one-layer sensor model, (b) the two-layer sensor model.

In the 3-D models, building a source mask is the next step for the simulation after the parameters of acoustic medium are set. The source mask defines the properties of an acoustic source including the size, location and pressure distribution. A circular source mask was used to simulate the circular transducer in the real application that generates ultrasound wave. The height of the source mask is the same in the two models, which is set to 20 grids; the diameter of the source mask is equal to 190 grids. Figure 3.3 shows the source mask built for the acoustic source simulation in the 3-D model.

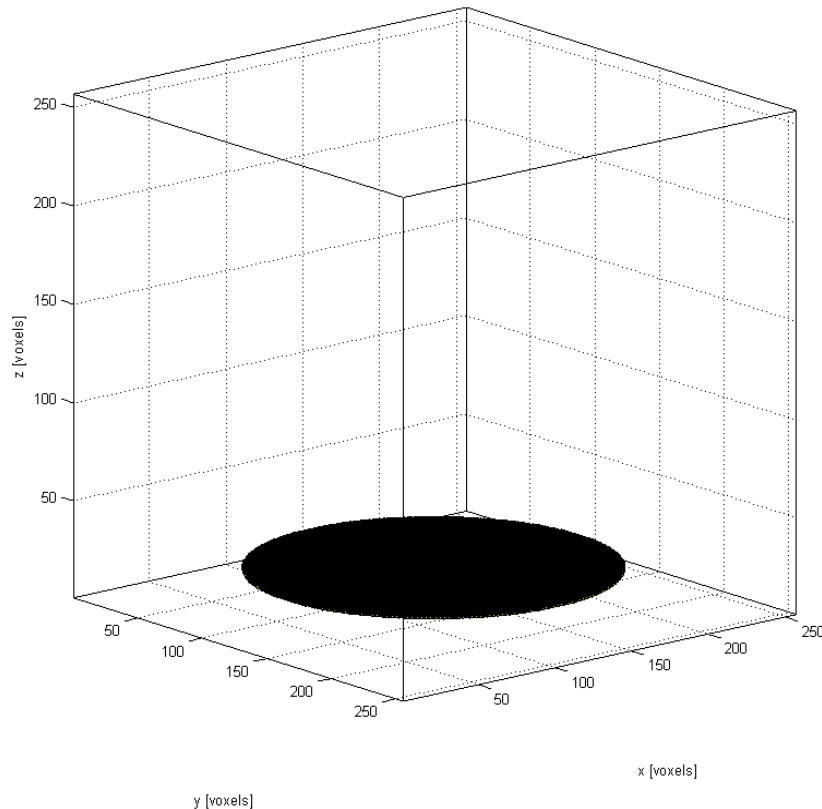


Figure 3.3: The source mask built for the acoustic source simulation in the 3-D model.

A simulated planar sensing array was set as a detector mask in the 3-D models, which measures and records ultrasound pressure distribution during the simulation. The shape of the detector array is a square; the side of the square takes 256 grids; and the height of the detector array is equal to 170 grids. Figure 3.4 shows the detector array built to record output ultrasound pressure during the simulation in the 3-D model.

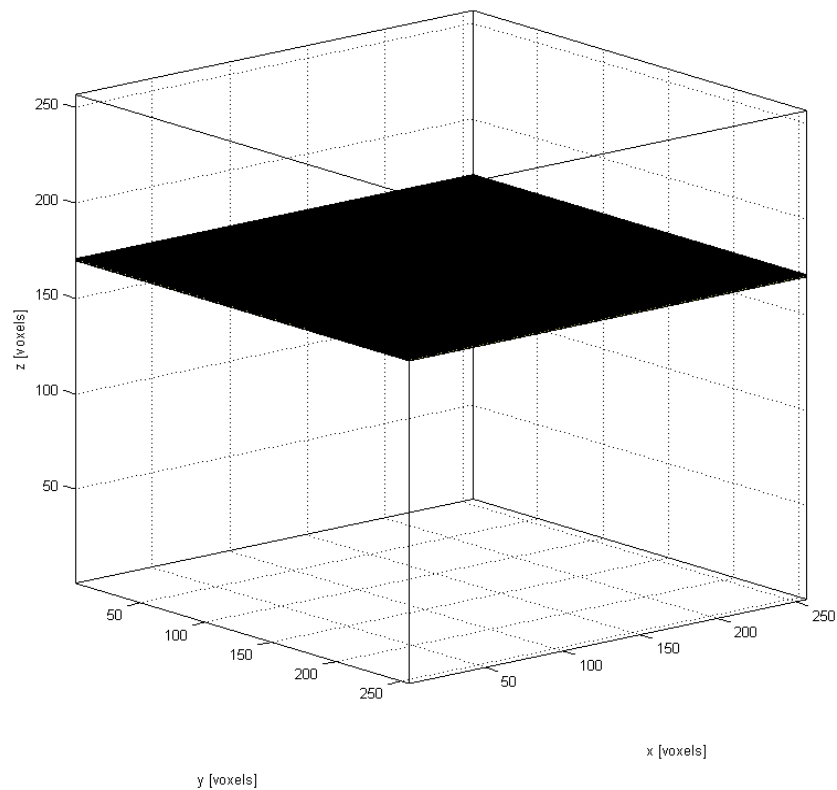


Figure 3.4: The detector array built in the 3-D model to record output ultrasound pressure during the simulation.

The same ultrasound wave in the 3-D models is generated by the source mask and transmits to sensors. The pressure distribution of the ultrasound wave is shown in Figure 3.5, where the  $X$  and  $Y$  axes represent spatial coordinates on section position, and the  $Z$  axis represents the ultrasound pressure which is scaled using jet colormaps. The amplitude of the acoustic wave increases as the colour changes from blue to red. The ultrasound wave is a plane-wave, which in turn is an approximation of the realistic ultrasound wave generated by the transducer of the SonaCell ultrasound generator.

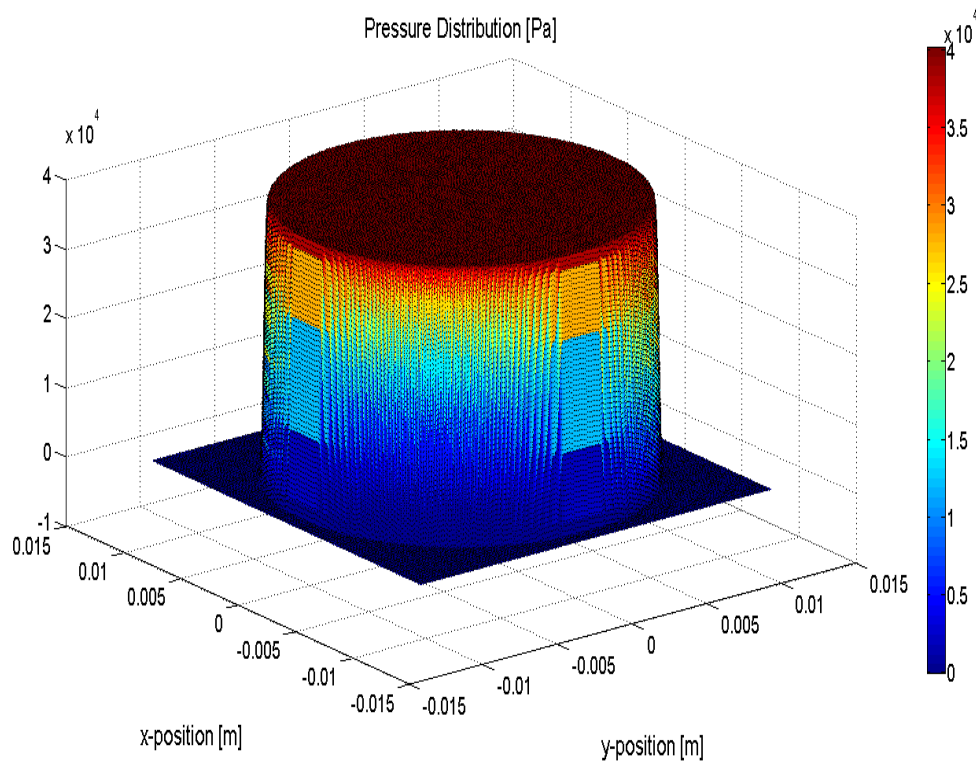


Figure 3.5: Pressure distribution of the generated ultrasound wave.

The majority of the ultrasound energy is transmitted into the sensors, reflected at the back of the sensor, and then propagates through the front face back to the medium. In the simulation, the remaining ultrasound energy after passing through each sensor is measured by the planar detector array. Acoustic attenuation of a material is represented by equation (3.3):

$$I(x) = I_0 e^{-\alpha f x} \quad (3.3)$$

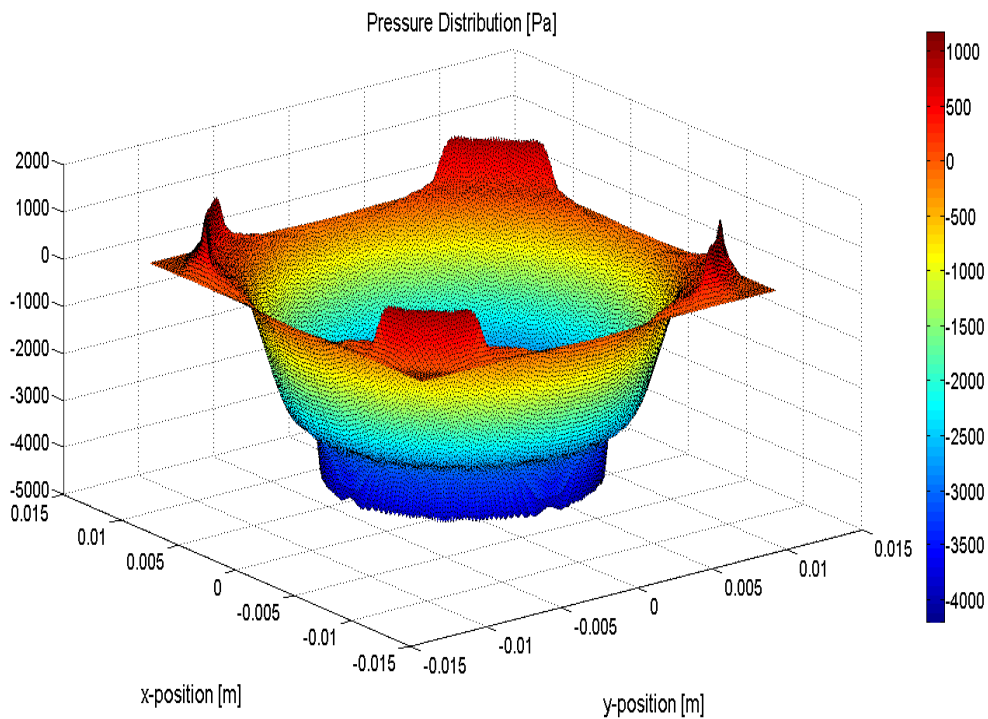
where  $I_0$  represents the incident ultrasound intensity,  $I(x)$  is the ultrasound intensity after attenuation,  $x$  is the thickness of the material,  $\alpha$  is the attenuation coefficient of the material and  $f$  is the frequency of the incident ultrasound.

Equation (3.3) shows that acoustic attenuation is not only a function of a material property, but also a function of frequency. The absorption rate of the sensor increases with the acoustic frequency. The simulation is based on an acoustic frequency of 1.5 MHz, which has been widely used in therapeutic applications.

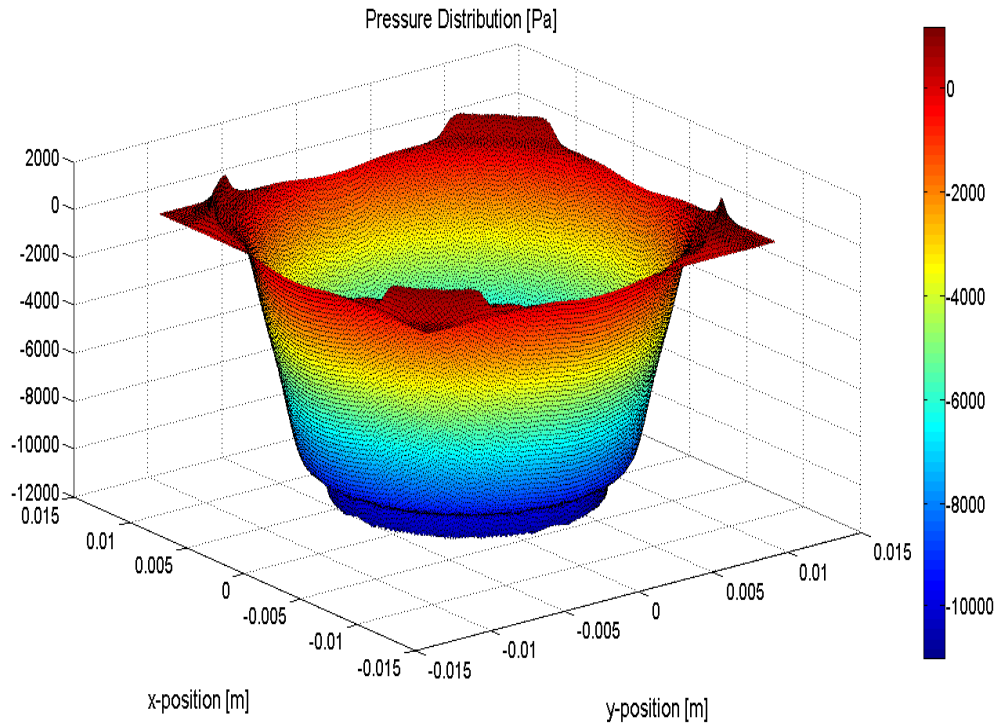
Figures 3.6 (a) and 3.6 (b) show the ultrasound pressure distributions of the remaining waves after attenuation by the two-layer and one-layer sensors respectively, where the  $X$  and  $Y$  axes represent section position, and the  $Z$  axis represents the ultrasound pressure of the corresponding position. Jet colormaps shows the relationship between ultrasound amplitudes and colours. The amplitude of the acoustic wave decreases as the colour changes from red to blue. In Figure 3.6, it can be observed that the maximum amplitude of the remaining ultrasound

after attenuation by the two-layer structure is about 4000 Pa, while the maximum amplitudes of the remaining ultrasound after attenuation by the one-layer is around 12000 Pa, which is three times larger than the two-layer structure.

The absorption efficiency of the two sensors is evaluated by calculating and comparing the average pressure of the remaining waves after attenuation by the sensors with the average pressure of the input wave. The evaluation results show that approximately 7.5% and 22.5% of the input ultrasound energy are transmitted after passing through the two- and one-layer sensors respectively, thus establishing the two-layer sensor as the better of the two.



(a)



(b)

Figure 3.6: Ultrasound pressure distributions of the remaining waves for (a) the two-layer sensor after attenuation, and (b) the one-layer sensor after attenuation.

### 3.3 Transient Temperature Model Evaluation

After the sensor manufacture, a calibration for the thermistor is required to find a quantitative relationship between the temperature of the sensor and the resistance of the thermistor. Thermistor calibration was implemented as the method introduced in the previous chapter. After thermistor calibration, the thermoacoustic sensor is able to measure the temperature changes induced by the

applied ultrasound intensities. Based on the measured temperature changes, the temperature data are related with the incident ultrasound intensities.

To evaluate the performance of the two-layer sensor compared to the one-layer sensor, the same ultrasound intensity was applied to the two sensors to observe their thermal response. Figure 3.7 shows the comparison of the two sensors' thermal response at the same intensity level of  $60 \text{ mW/cm}^2$  in 30 seconds. The ultrasound intensity of  $60 \text{ mW/cm}^2$  was generated by the SonaCell generator and calibrated using the radiation force balance (UPM-DT-1AV, Ohmic Instruments.). It can be observed that the two-layer sensor has more temperature increase than the one-layer sensor under the same ultrasound intensity, indicating that the two-layer structure can greatly improve energy absorption rate of the thermoacoustic sensor.

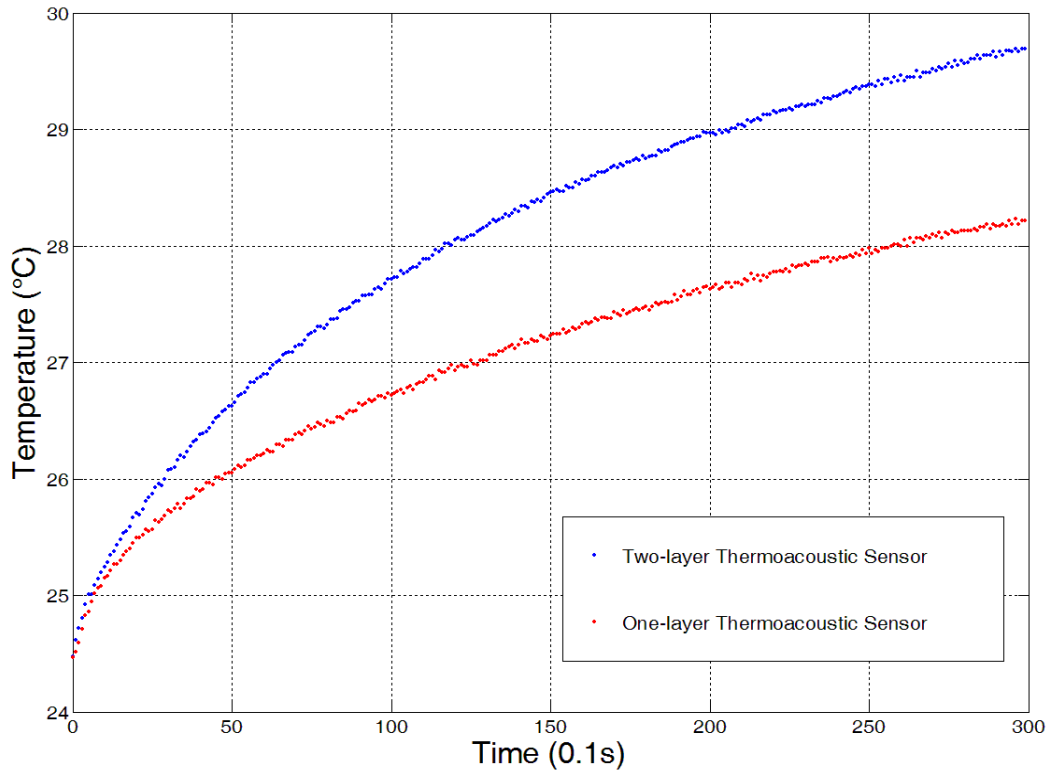


Figure 3.7: Thermal response comparison between the two-layer sensor and the one-layer sensor under the same intensity level of  $60 \text{ mW/cm}^2$ .

As discussed in the previous chapter, the equilibrium temperature approach and transient temperature profile are two methods for relating a temperature increase to the applied ultrasound intensity. To provide a rapid measurement, the transient temperature method was also employed to evaluate temperature data measured by the two-layer sensor design, which quickly relates the given transient temperature increase to the applied ultrasound intensity in the sensor. This approach enables rapid readouts of the applied ultrasound intensity based on a temperature-rise coefficient [43, 44]. The first mode of transient profiles is given by equation (3.4).

$$T(t) = T_s + C \left( 1 - e^{-\frac{t}{\tau}} \right) \quad (3.4)$$

where  $T(t)$  is the measured temperature of the absorbing cylinder,  $T_s$  is the starting temperature,  $C$  represents the temperature-rise coefficient determined by the ultrasound intensity,  $\tau$  is a time constant determined during curve fitting procedure and  $t$  represents measurement time.

Data fitting was performed based on the first mode of transient profiles using MATLAB's curve fitting toolbox. Figure 3.8 shows the curve fitting results for temperature increases in the sensor under an ultrasound intensity of 60 mW/cm<sup>2</sup>. Table 3.2 shows the coefficients of the fitting curve based on equation (3.4), and Table 3.3 shows its curve fitting accuracy for the temperature rise data. From Figure 3.8 and Table 3.3, we conclude that the fitting curve based on equation (3.4) does conform to the measured data, which validates the feasibility of the transient temperature model in this sensor design.

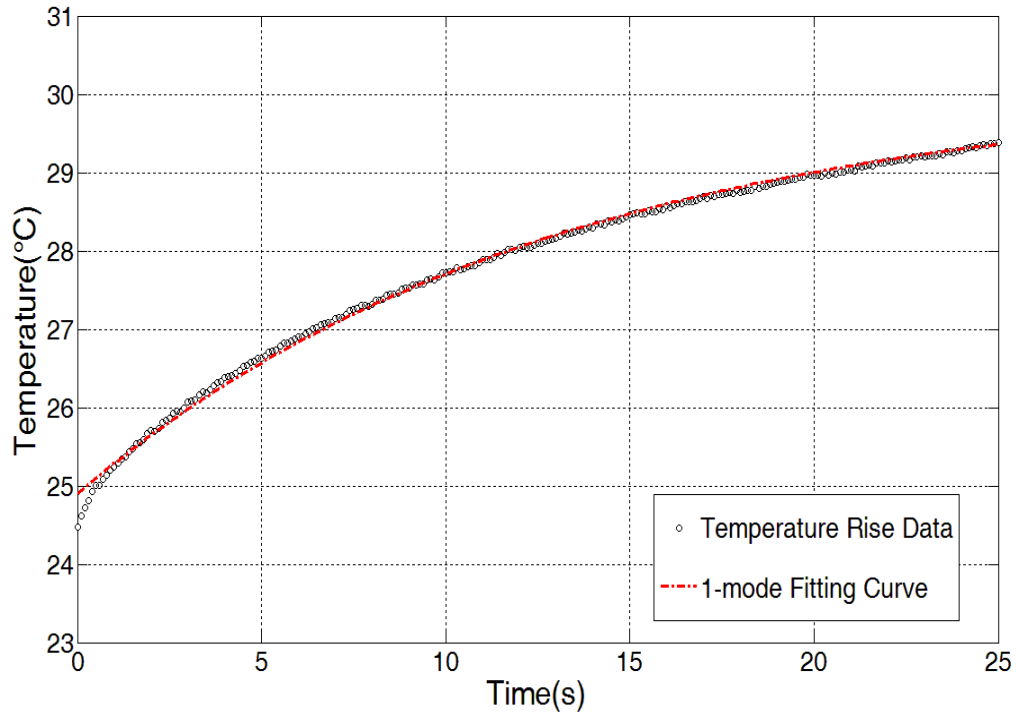


Figure 3.8: Curve fitting results for temperature rise data based on the first transient model.

Table 3.2: The coefficients of the first transient model curve fitting.

Ultrasound Intensity (mW/cm <sup>2</sup> )	Coefficient C (°C)	Coefficient $\tau$ (s)	Coefficient T0 (°C)
60	4.847 (4.798,4.895)	10.75 (10.46,11.04)	24.9 (24.88, 24.93)

Note that the numbers in the brackets indicate prediction bounds with 95% certainty.

Table 3.3: Curve fitting accuracy of the first transient model curve fitting.

SSE	R-square	RMSE
0.4923	0.9982	0.04999

It is worthy to note that an obvious deviation of the first-mode fitting curve from the measured data exists at the very beginning in Figure 3.8. Reference [35] shows that three modes of transient temperature profiles can improve the fitting accuracy of the steep rising part at the very beginning, therefore, the fitting curve based on the three modes of transient profiles is also included for a comparison.

The three modes of transient profiles are represented by equation (3.5).

$$T(t) = T_s + C_1 \left[ \left( 1 - e^{-\frac{t}{\tau_1}} \right) - C_2 \left( 1 - e^{-\frac{t}{\tau_2}} \right) + C_3 \left( 1 - e^{-\frac{t}{\tau_3}} \right) \right] \quad (3.5)$$

where  $\tau_1$ ,  $\tau_2$  and  $\tau_3$  are the time constants,  $C_2$  and  $C_3$  are the coefficients and  $C_1$  is the only coefficient related to the ultrasound intensity.

MATLAB's curve fitting toolbox was employed to do the curve fitting for the measured temperature data based on the three modes of transient profiles. The curve fitting results for temperature data of the sensor at ultrasound intensity of 60 mW/cm<sup>2</sup> is shown in Figure 3.9. Table 3.4 shows the coefficients of the fitting curve based on the three modes of transient temperature profiles, and Table 3.5 shows its curve fitting accuracy for the temperature rise data. Figure 3.9 demonstrates that the fitting curve based on equation (3.5) does have a better approximation of measured data of the steep rising part at the very beginning. In

the sensor design, the approach based on the three modes of transient profiles was not used, since the model with so many parameters makes data evaluation and calibration much more difficult, if not possible, in the real application. Especially, the embedded system based a microcontroller cannot accurately fitting the temperature data based on the model in real-time due to its complexity. On the other hand, curve fitting based on the first transient model can be effectively and accurately implemented in the embedded system to fit the temperature curve in real-time. Curve fitting based on equation (3.4) suggests that the coefficient  $C$  at a specific ambient temperature is directly related to the applied ultrasound intensity; this relationship is applied to the following neural network training.

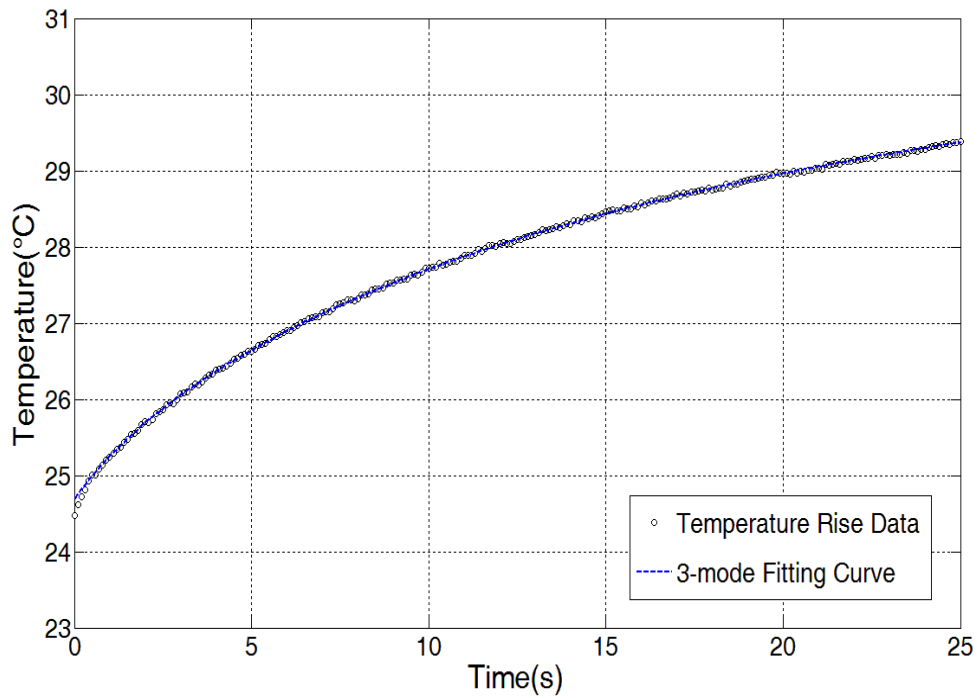


Figure 3.9: Curve fitting results for temperature rise data based on the three modes of transient profiles ( $60 \text{ mW/cm}^2$ ).

Table 3.4: The coefficients of the curve fitting based on the three modes of transient profiles.

Ultrasound Intensity (mW/cm <sup>2</sup> )	Coefficient C <sub>1</sub> (°C)	Coefficient C <sub>2</sub> (°C)	Coefficient C <sub>3</sub> (°C)
60	5.083	-0.0374	0.1819
Coefficient $\tau_1$ (s)	Coefficient $\tau_2$ (s)	Coefficient $\tau_3$ (s)	Coefficient T <sub>s</sub> (°C)
18.28	0.00274	2.706	24.47

Table 3.5: Curve fitting accuracy of the three modes of transient profiles.

SSE	R-square	RMSE
0.1142	0.9998	0.01974

### 3.4 Artificial Neural Network in Sensor Design

The thermoacoustic sensor measures the temperature increase caused by incident ultrasound energy to determine the ultrasound intensity. However, the sensor characteristics are not only dependent on applied ultrasound intensity, but also on ambient temperature and the slightly changing acoustic properties of absorber materials as the absorber heats up, which create a complex problem in sensor design. To obtain an accurate and consistent measurement, these effects should be considered and compensated for in the thermal sensor design. The

traditional computational method usually identifies a deterministic mathematical relationship through data interpolation; however, this method is inadequate for solving the problem, since it is extremely difficult to resolve the mathematical formula, if not impossible, among multiple confounding variables such as the temperature change of the sensor, applied ultrasound intensity and ambient temperature from measured data. A solution using extrapolation and interpolation based on calibration values is proposed in the previous sensor design, but the method is still unsatisfactory due to the requirement of complex calibration, calculation procedures, and limited improvement in accuracy.

In the improved sensor design, we propose the implementation of an artificial neural network to identify the relationship and solve the problem. Artificial neural networks, as an artificial intelligence technique, have been widely applied in engineering for function approximation, classification, clustering and regression, due to its adaptive ability for modeling. Function approximation is a very important application of artificial neural networks to provide an effective approximation for multivariable functions when a deterministic mathematical relationship is too complicated to be identified by the computational method. An artificial neural network maps the implicit relationship of inputs and outputs through the training and testing of measured data, which has been applied to compensate for the various nonlinear errors in system designs [45-50]. In addition to the universal approximation ability, the advantages of artificial neural networks also include good capability for generalization and reliability [82]. Through proper training, the artificial neural network can compensate for the

temperature drifts, enabling a direct read-out of the applied ultrasound intensity in the sensor design.

### **3.4.1 Artificial Neural Network Structure and Back Propagation Algorithm**

The back propagation (BP) neural network is one of the most widely used artificial neural network models based on a multi-layer perceptron structure and a gradient descent optimization method [45]. The algorithm is an iterative gradient search technique, which calculates gradient descent and iteratively updates network weights in order to minimize error between the network output and the desired output [81, 82]. The artificial neural network consists of three layers: the input layer, one or more hidden layer(s), and the output layer. An illustrative three-layer artificial neural network is shown in Figure 3.10. As illustrated in the figure, each layer has a number of nodes (neurons) that fully connect to adjacent layers, and each node receives the outputs from the previous layer with a distinct set of weights.

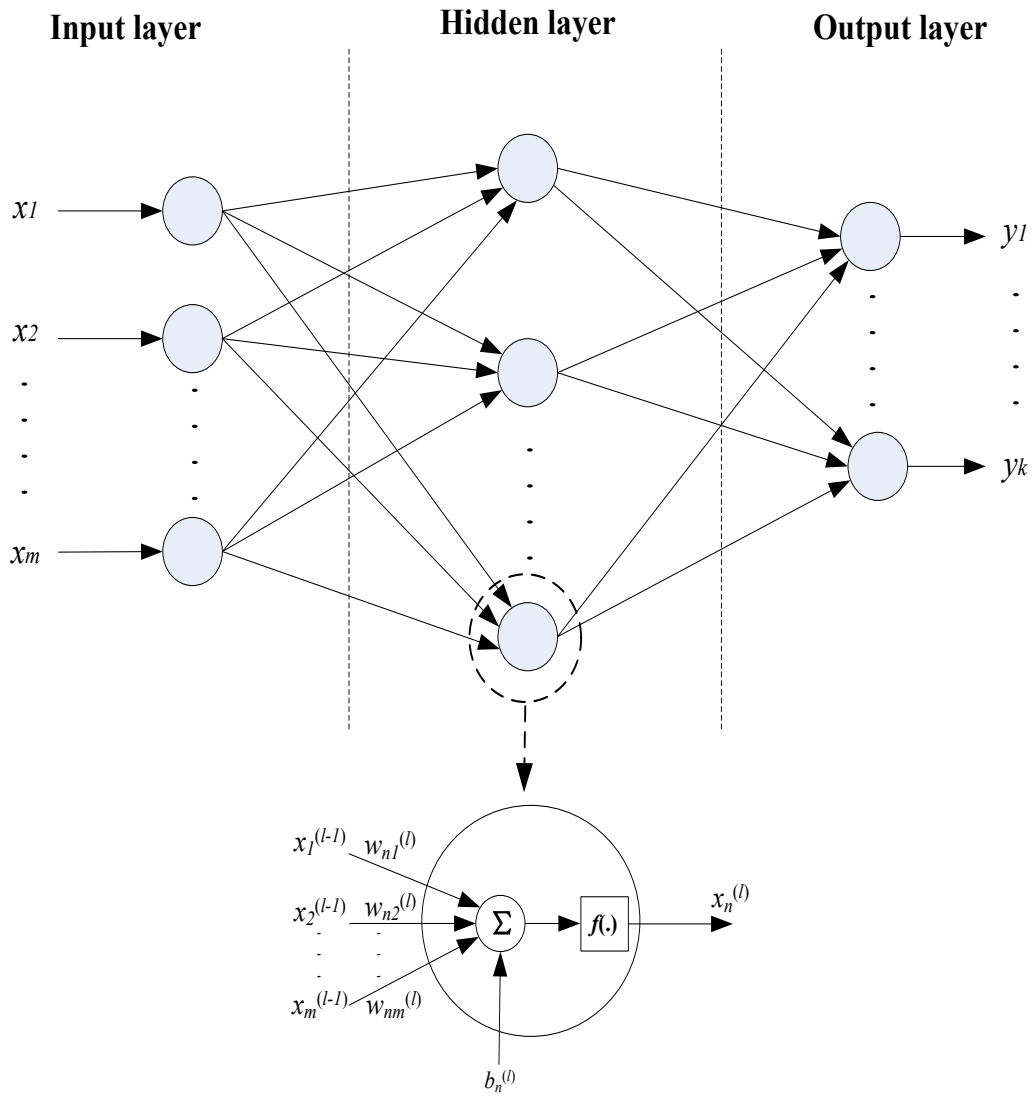


Figure 3.10: Schematic of a three-layer artificial neural network.

The output of the  $n^{th}$  neuron in layer  $l$  is represented by equation (3.6)

$$x_n^{(l)} = f[Sum_n^{(l)}] \quad (3.6)$$

where  $Sum_n^{(l)}$  is the sum of the outputs from the previous layer with a distinct set of weights, which is given by the equation (3.7)

$$Sum_n^{(l)} = \sum_{m=1}^M w_{nm}^{(l)} x_m^{(l-1)} + b_n^{(l)} \quad (3.7)$$

In the equation,  $x_m^{(l-1)}$  is the output of the  $m$ th neuron in the layer  $(l-1)$ ,  $w_{nm}^{(l)}$  is the weight between the  $n$ th neuron in layer  $l$  and the  $m$ th neuron in the layer  $(l-1)$ ,  $b_n^{(l)}$  is the bias for the  $n$ th neuron in layer  $l$  ( $l=1, 2, 3$ ), and  $f(\cdot)$  is the activation function of the neuron.

The mathematic model of a BP network with a single hidden layer is illustrated in Figure 3.11.

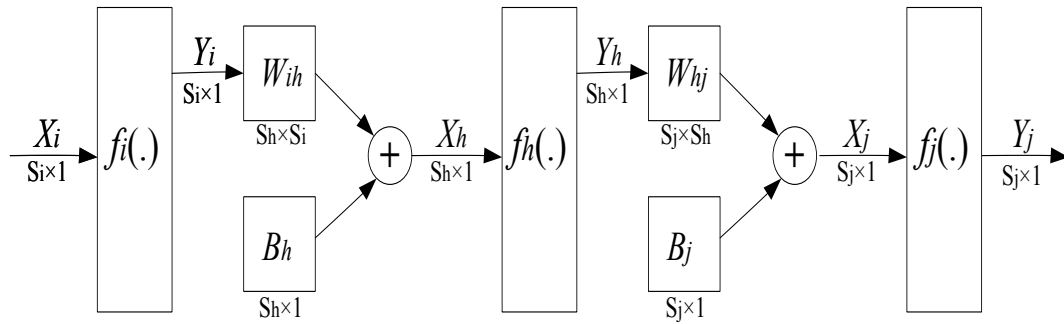


Figure 3.11: The mathematic model of a BP network.

In the mathematic model,  $S_i$  represents the number of elements of input vectors  $X_i$ ,  $S_h$  and  $S_j$  represent the number of neurons in the hidden layer and the output layer, respectively.  $W_{ih}$  denotes the weight vector between the input layer and the hidden layer, and  $W_{hj}$  denotes the weight vector between the hidden layer

and the output layer,  $B_h$  and  $B_j$  respectively stand for the bias value vector of the hidden layer and the output layer.  $f_i(\cdot)$ ,  $f_h(\cdot)$  and  $f_j(\cdot)$  represent the activation function of the input layer, the hidden layer and output layer, respectively. For the back propagation neural network, the activation functions of the input and output layer are both linear function, while the activation function of the hidden layer is a hyperbolic tangent function.

### **3.4.2 Artificial Neural Network Model in Sensor Design**

For each of the various discrete values of the starting ambient temperature and ultrasound intensity, the thermal characteristic of the sensor is stable and its coefficients through curve fitting are unique. The identification of the relationship among the parameters is the basis of the thermoacoustic sensor design. It is extremely difficult to use traditional computational methods to resolve the mathematical formula and identify the relationship. To solve this problem, the artificial neural network method is introduced to map the relationship and compensate for temperature drifts in the improved sensor design. The compensation model using a neural network is shown in Figure 3.12.

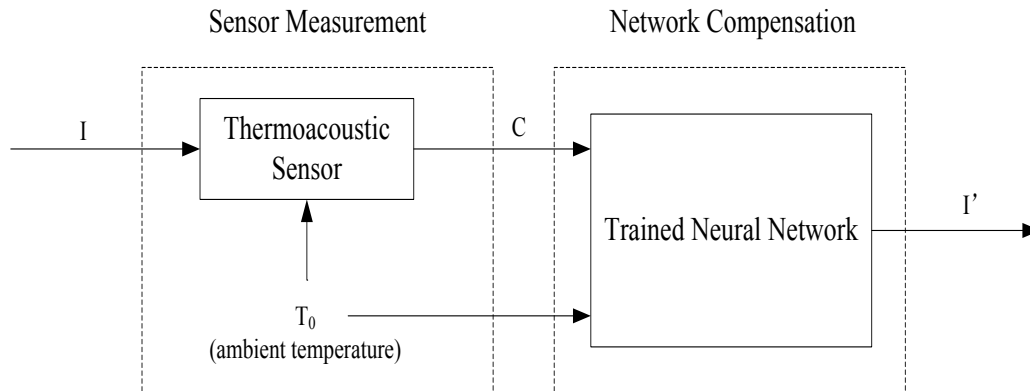


Figure 3.12: Model of the thermoacoustic sensor compensation using a neural network. The neural network algorithm is implemented using the microcontroller.

In this model,  $I$  is the applied ultrasound intensity to be measured.  $T_0$  is the ambient temperature that affects the sensor measurement accuracy.  $C$  is the temperature rising coefficient calculated by the sensor, which is affected by the ambient temperature.  $I'$  is the adjusted ultrasound intensity after neural network compensation. The proper parameters of the neural network are trained with 50 pairs of measurements (refer to the later discussion in section 3.4.3). Once the parameters are determined after the neural network has been well trained, the sensor characteristics are learned by the trained neural network, which allows for both rapid and accurate estimations of  $I$  based on  $C$  and  $T_0$ .

### 3.4.3 Artificial Neural Network Training

To target low ultrasound intensities commonly set for biomedical applications at regular room temperatures, we took measurements on a range of

intensities within  $30 \text{ mW/cm}^2$  to  $120 \text{ mW/cm}^2$  with an increment of  $10 \text{ mW/cm}^2$  at ambient temperatures  $20 \text{ }^\circ\text{C}$ ,  $21.5 \text{ }^\circ\text{C}$ ,  $23 \text{ }^\circ\text{C}$ ,  $24.5 \text{ }^\circ\text{C}$  and  $26 \text{ }^\circ\text{C}$ . The values of  $C$  corresponding to each ultrasound intensity and room temperature were obtained through curve fitting based on the transient temperature model. The three parameters of coefficient  $C$ , ultrasound intensity, and ambient temperature comprise a data set, and a total of 50 data sets were obtained and recorded for network training.

For neural network training, the available data sets are usually divided into three groups: training, validation and testing. The training data are used to directly train the network to learn the sensor characteristics, while the other data are set aside for validation and testing purposes. The validation and testing data are employed to check and avoid the problem of over-training, in which the trained network works well for the training data with minimum error, but cannot be generalized to the untrained data well. During the training process, the input of a training data set is imported to the neural network, and the output of the network is calculated. After that, the calculated output is compared with the target output of the training data set to obtain the error, which is used to update network weights and biased interactively based on the gradient calculations as described in section 3.4.1. Application of all training data sets to train the network constitutes one training epoch or iteration. The training performance after each epoch was evaluated using mean squared error between the current estimation and the target output. The generalization error of the validation sets is monitored during the training process and used to decide the time to stop training. Similar as the

training data sets, the error of validation sets usually goes down dramatically at the initial phase of training, but the error goes up when the network is over-trained based on the training data [82]. For testing data sets, although they are not involved in the training process, the error of test data sets is useful to independently evaluate the training performance in term of generalization. The training process continues epoch after epoch until a best validated performance is found.

The neural network training was implemented through the MATLAB Neural Network toolbox. 88% of the total data sets were randomly selected for training, 6% for validation and 6% for testing. After the data classification, the next step for the neural network training is to determine the network architecture. Theoretically, it had been demonstrated that three layers of neural network could approximate any complex function with accuracy [83]. Therefore, a three-layer neural network as indicated in Figure 3.10 was applied in the sensor design. The network structure is further determined by specifying the number of nodes in each layer. The number of nodes in the input layer and output layer were chosen to be 2 and 1, respectively, according to the sensor model. For the nodes in the hidden layer, no theory is available to demonstrate the best number of the nodes should be chosen in the real application. If the number of the nodes in the hidden layer is too small, both training error and generalization error will be high because of underfitting; however, if the number of hidden neurons is too large, the training error will be very low, but the generalization error will still be high due to overfitting [84].

Therefore, the number of nodes in the hidden layer should be determined experimentally.

To determine the optimal number of hidden neurons, neural networks with different structures in the hidden layer were trained and tested with the back propagation algorithm, and the training error and generalization error of each network were calculated for evaluation and comparison. In the sensor design, the network training was implemented by starting from 1 hidden neuron and adding hidden neurons sequentially up to 8 neurons. The performance of the network training was evaluated by mean square error (MSE). Figure 3.13 shows variations of mean squared error with training epochs, when the neural network has three hidden neurons. The errors of the training data, validation data, and training data keep decreasing at the beginning stage of training. Although the error of the training group still decreases after epoch 28, the errors of the validation and testing groups begin to increase, which indicates the network has been over-trained after epoch 28. Therefore, the trained network with three hidden neurons has the best validated performance at epoch 28.

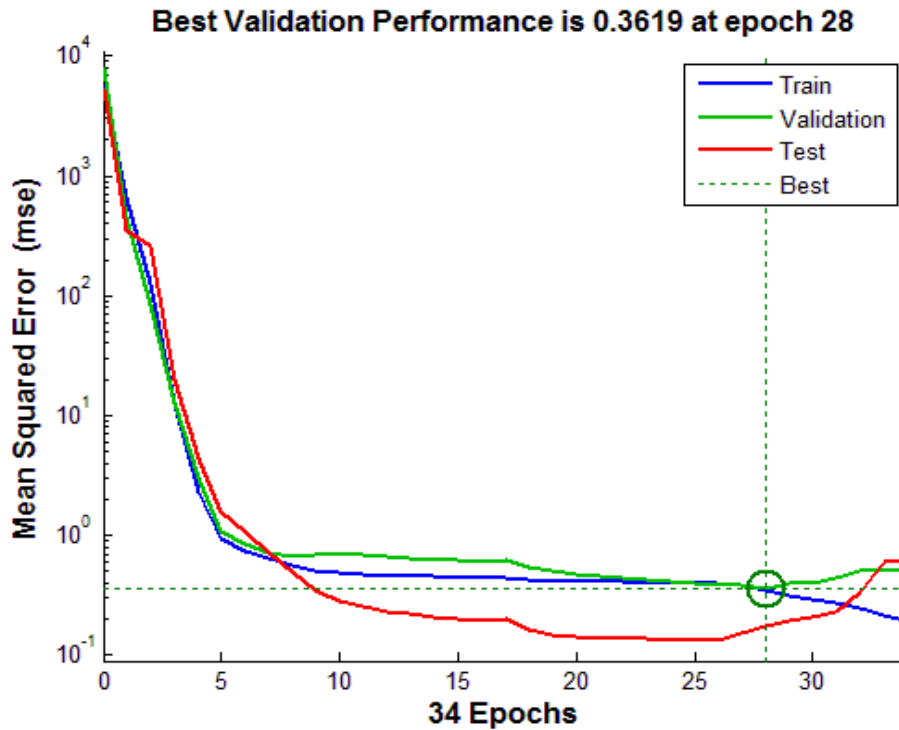


Figure 3.13: Variation of mean squared error with training epochs (three hidden neurons).

The performance of the trained networks with different numbers of neurons in the hidden layer is plotted in Figure 3.14. For different architectures, mean square errors (MSEs) of training, validation and testing data sets were compared and evaluated. As indicated in the figure, when the number of the hidden neurons is not significant, the training error and generalization errors from validation and testing data sets are high. On the other hand, when the number is too large, although the training error is very low, the generalization error of the testing data sets becomes high. The number of nodes in the hidden layer was chosen to be 3 in the sensor design, since the neural network structure has a good combination of

training error and generalization error, which indicates a good capacity of generalization.

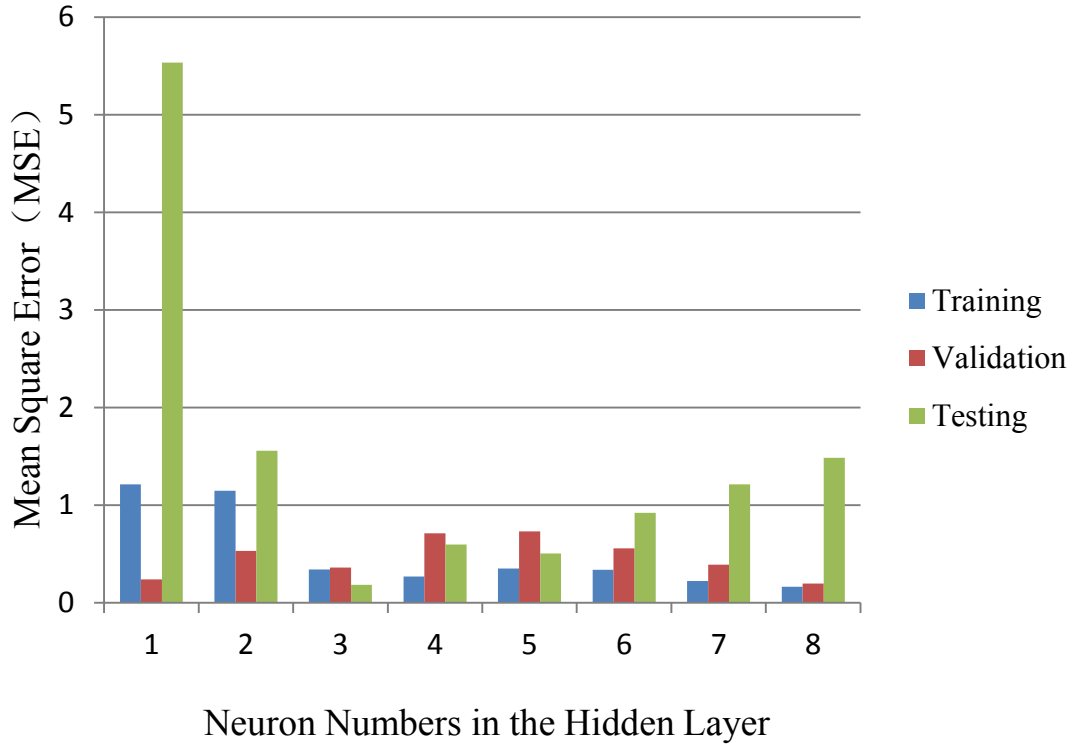


Figure 3.14: MSE vs number of hidden neurons in a three-layer neural network.

From the network training, a structure of 2-3-1 was finally adopted in the proposed three-layer neural network. The weight and bias matrices for the trained neural network with three hidden neurons at epoch 28 are shown in (3.8)–(3.11), which were saved and programmed into the micro-controller in order to realize the temperature compensation.  $W_{ih}$  denotes the weight between the input layer and the hidden layer,  $W_{ho}$  denotes the weight between the hidden layer and the output layer,  $B_h$  and  $B_o$  represent the bias of the hidden layer and the output layer respectively.

$$W_{ih} = \begin{bmatrix} 3.5008 & 5.0117 & 0.47412 \\ -1.3035 & 4.4669 & -0.10647 \end{bmatrix} \quad (3.8)$$

$$B_h = [-3.3727 \quad 1.8568 \quad 0.086394] \quad (3.9)$$

$$W_{ho} = [0.1084 \quad 0.014241 \quad 2.8166]^T \quad (3.10)$$

$$B_o = [-0.079312] \quad (3.11)$$

The network training results for training data, validation data, testing data, and all data are shown in Figure 3.15. The performance of the trained network is evaluated by comparing its output intensity based on the input of C and ambient temperature with the real applied intensity (target intensity). If the output of the trained network matches with the actual applied intensity closely, it can be concluded that the network has learned the sensor characteristics satisfactorily. Linear lines are used to fit all data and evaluate their correlation. As shown in the figure, regardless of various ambient temperatures and applied intensities, a very good agreement between the network's output intensity and target intensity for all data can be observed, the good agreement is also demonstrated from the correlation factor  $R$  among training data, validation data and testing data, which are all higher than 0.999. Overall, the estimated output intensity by the trained neural network matches the target intensity very well, which verifies that the trained neural network can effectively correct ambient temperature effects and accurately measure the ultrasound intensity.

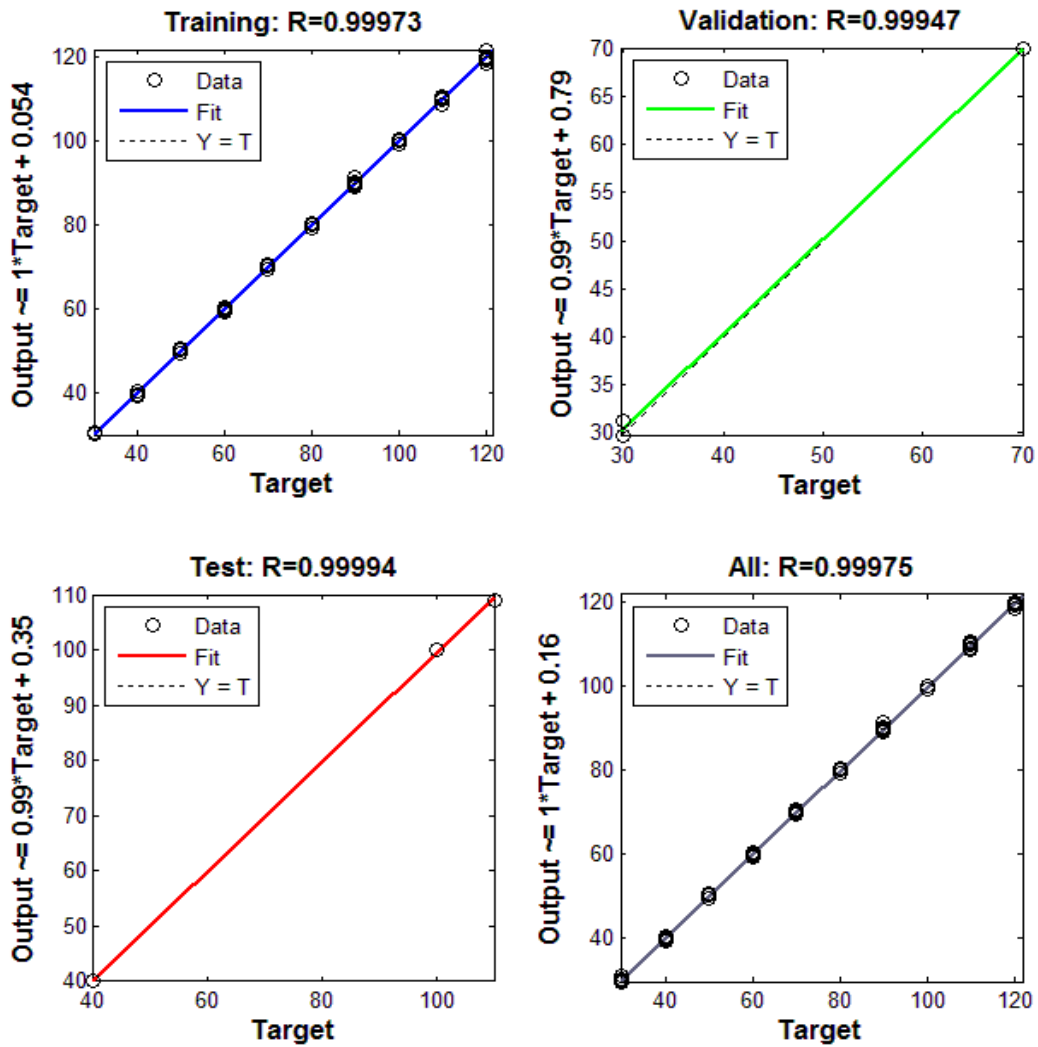


Figure 3.15: The agreement between the network's output intensity and target intensity.

### 3.5 Sensor Performance Evaluation

#### 3.5.1 Neural Network Evaluation with Untrained Data Sets

The performance of the trained network is further evaluated at two ambient temperatures on  $C$  that has never been trained and tested. At 20 °C, a set of  $C$

from 1 to 8.5 in 0.5 increments are given to the neural network, and estimated ultrasound intensities are generated as output. Figure 3.16 shows the estimated and real measured data sets at temperatures of 20 °C. As indicated in the figure 3.16, the estimated intensities and the real measurements almost entirely overlap at 20 °C.

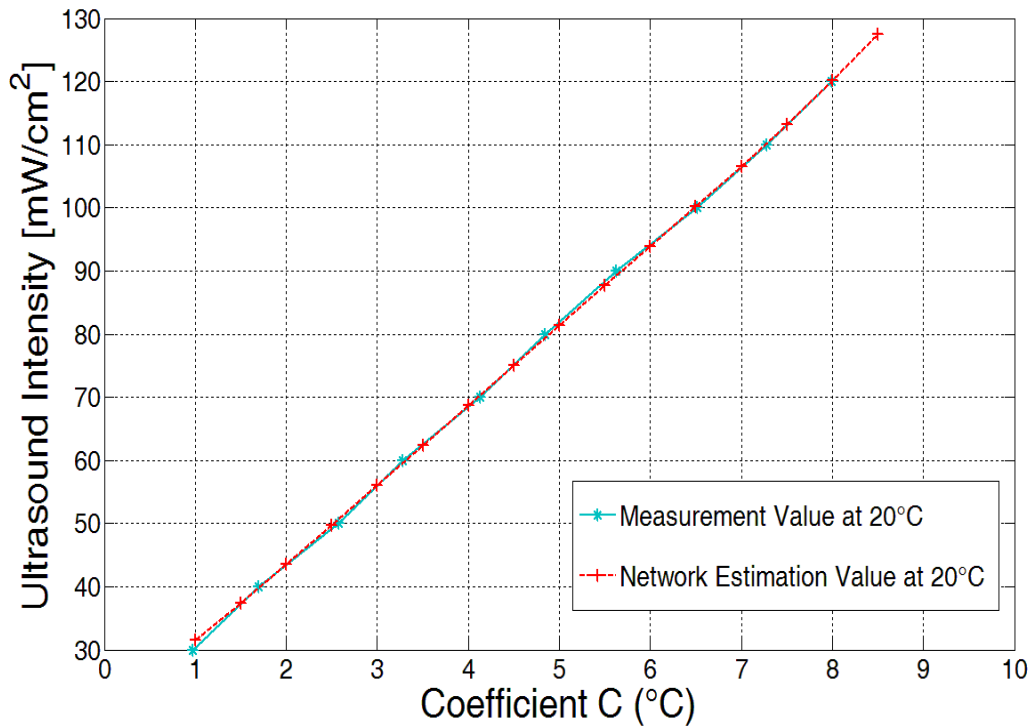


Figure 3.16: Comparison between the estimated data sets by the neural network and the real measurement data sets at 20 °C.

At 25 °C, a temperature that has never been trained, another set of  $C$  from 2 to 10.5 in 0.5 increments were fed into the neural network. The estimated ultrasound intensities and real measurements were compared with each other to further evaluate the performance of the neural network. The estimated and real measured data sets at temperatures of 25 °C were plotted in Figure 3.17. As

illustrated in the figure, the estimated intensities and the real measurements also have a good agreement at that temperature, thus verifying that the trained network not only works for trained data sets, but is also valid for untrained data sets.

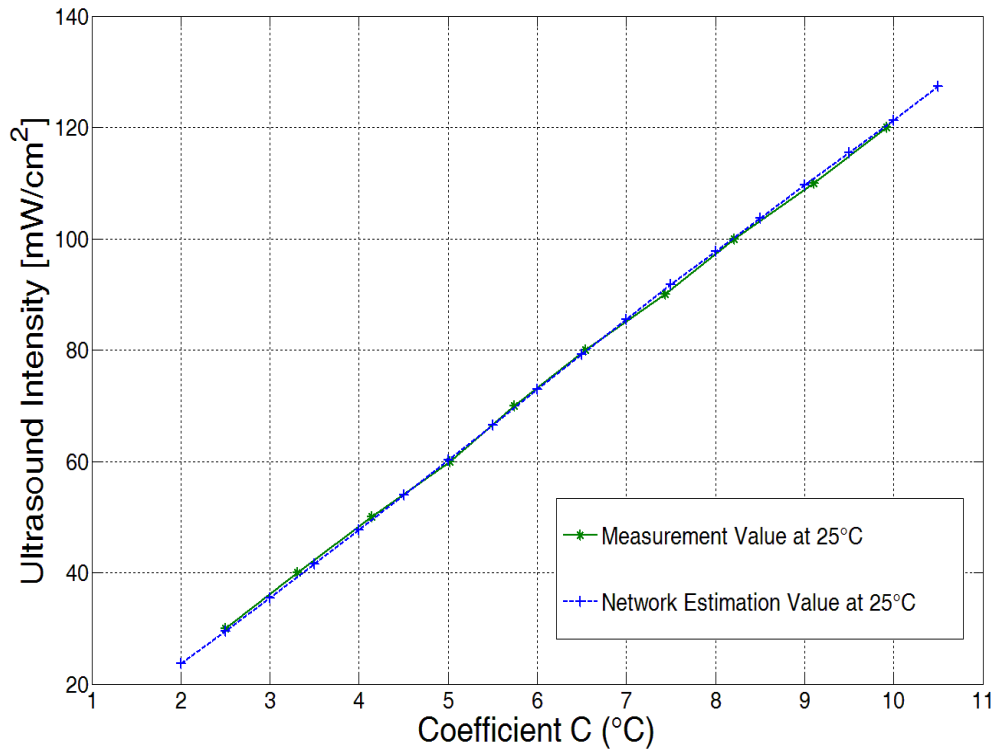


Figure 3.17: Comparison between the estimated data sets by the neural network and the real measurement data sets at 25 °C.

### 3.5.2 Network Temperature Compensation Performance

To evaluate the performance of network temperature compensation, a comparison of the measurement results with and without the network temperature compensation was conducted. Figure 3.18 shows measurement errors with and without network temperature compensation over a range of ambient temperatures

at intensity of  $50 \text{ mW/cm}^2$ . The measurement error with network compensation is the difference between the applied intensity and the trained network output intensity, while the measurement error without compensation is obtained by comparing the applied intensity with the estimated intensity based on values of the corresponding  $C$  and the reference  $C$  at a temperature of  $23 \text{ }^\circ\text{C}$ . The evaluation results show that the average error with network compensation is around 1%, while the average error without network compensation is above 15%. The measurement error with network compensation is insensitive to the temperature drift, while the measurement error without network compensation increases with the temperature drift.

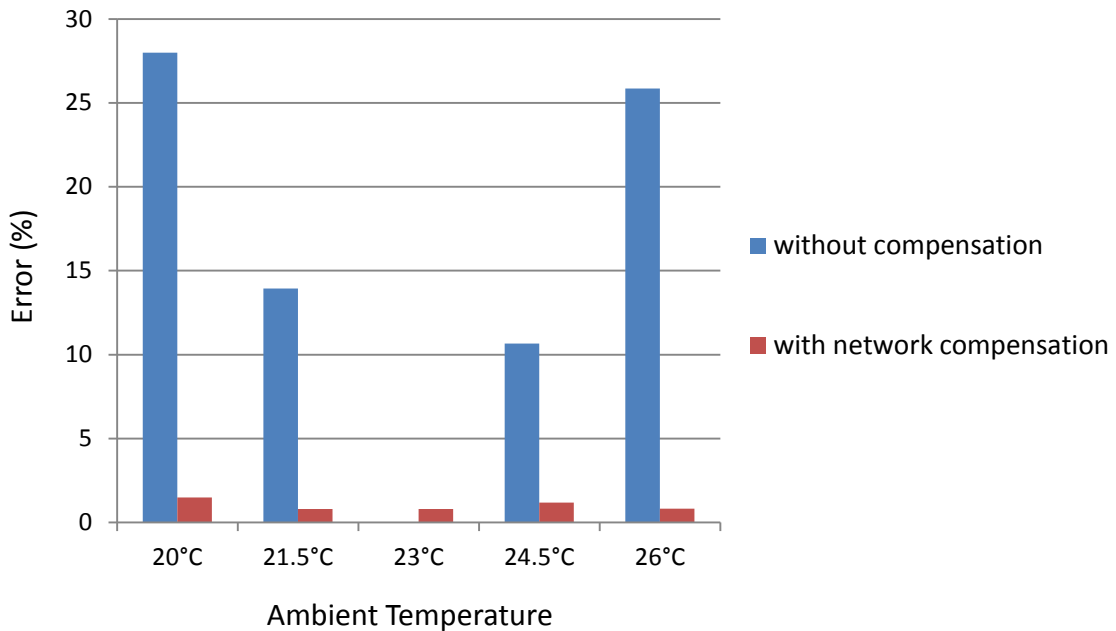


Figure 3.18: Ultrasound intensity error with and without network temperature compensation.

### 3.5.3 Sensor Response Time

It is important to design a sensor capable of producing an accurate measurement in a short response time. The new two-layer structure improves the absorption efficiency of the sensor design, and provides a more rapid and reliable estimation of ultrasound intensity based on faster energy conversion rates and a greater amount of captured energy. To evaluate the improvement of the two-layer sensor design, the response time of the one- and two-layer sensors were measured and evaluated. Figure 3.19 shows the measurement error percentage of the sensor designs at different time points under ultrasound intensity of  $40 \text{ mW/cm}^2$ . The error is the difference between the target intensity and the value measured by thermoacoustic sensors based on curve fitting. By inspecting the figure, we can determine the response time required for the two types of sensors to obtain a reliable measurement. The two-layer sensor can provide a reliable measurement in approximately 12 seconds, whereas it takes roughly 20 seconds for the one-layer sensor to obtain an acceptable measurement.

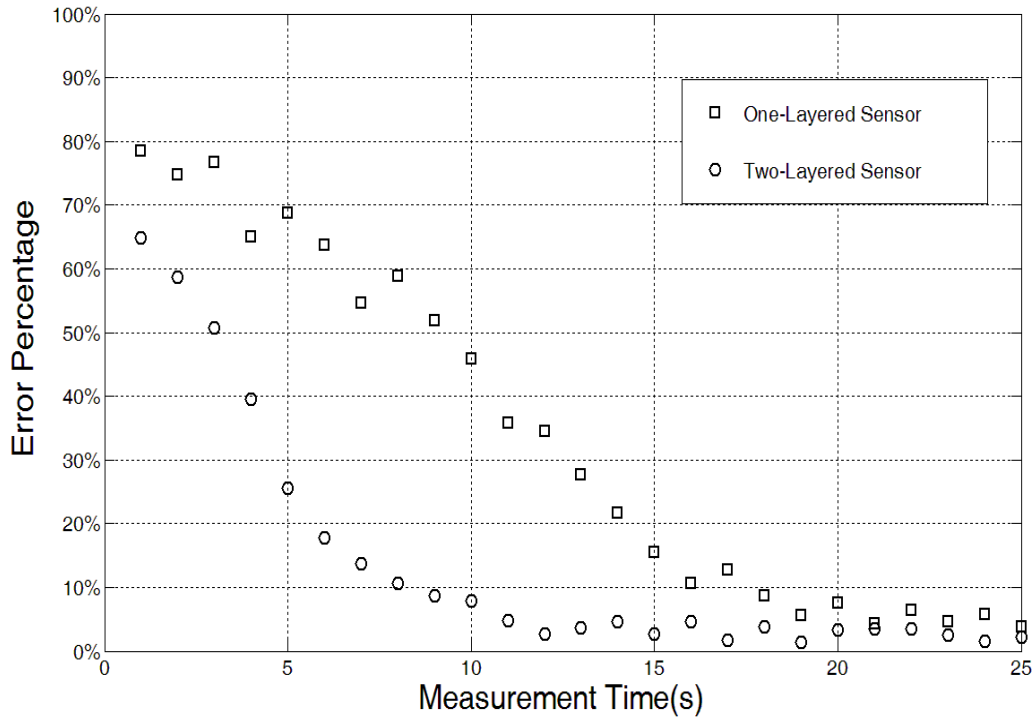


Figure 3.19: Response time of the one- and two-layer sensors with respect to measurement error percentage.

### 3.5.4 Measurement Comparison with the Previous Design

To extensively evaluate the improvement in measurement accuracy of the new two-layer sensor design, the SonaCell ultrasound generator was calibrated by the radiation force balance (UPM-DT-1AV, Ohmic Instruments) in an environment without noise vibrations in order to generate ultrasound intensities of 30, 40, 60, 80, 100 and 120  $\text{mW}/\text{cm}^2$ . The intensities are derived by dividing the measured power by the beam area of  $3.5 \text{ cm}^2$ , and the beam area was directly measured by a needle hydrophone system (Precision Acoustics Inc. Dorchester, UK) [74]. The ultrasound intensities generated by the SonaCell generator are

constant at room temperature. The improved sensor design was employed to measure each intensity at ambient temperatures of 22 °C, 23 °C, and 24 °C in order to investigate the agreement between the two techniques. Table 3.6 outlines measurement results of ultrasound intensities obtained by the two-layer sensor design based on the artificial neural network. The measurement results given by the previous one-layer sensor design are also included for better comparison. In the previous sensor design, a temperature compensation method through extrapolation or interpolation based on the calibration values was used to estimate the applied ultrasound intensities. All the measurement results are plotted in Figure 3.20 for comparison and evaluation. In the figure, the linear fit represents a 1:1 relationship between the radiation force balance and the thermoacoustic sensor. The excellent measurement agreement between the improved sensor design and the radiation force balance technique confirms that the sensor's measurements are accurate. Over the 18 measurement samples, the previous sensor design has an average error of 3.97 mW/cm<sup>2</sup>, while the improved sensor design has an average measurement error of 1.31 mW/cm<sup>2</sup>. Root-mean-square error (RMSE) of the previous design is 4.49, whereas RMSE of the improved sensor design is 1.63. Therefore, by evaluating the average error and RMSE of the measurement results, the great improvement in measurement accuracy of the new sensor design has been demonstrated.

Table 3.6: Measurement results of the improved sensor design.

Target I (mW/cm <sup>2</sup> )	Thermoacoustic Sensor I (mW/cm <sup>2</sup> )		
	#1	#2	#3
30	28.85	30.74	29.68
40	40.33	39.42	39.06
60	61.66	60.37	59.82
80	77.33	80.22	83.03
100	101.78	99.12	101.9
120	123.26	118.86	122.43

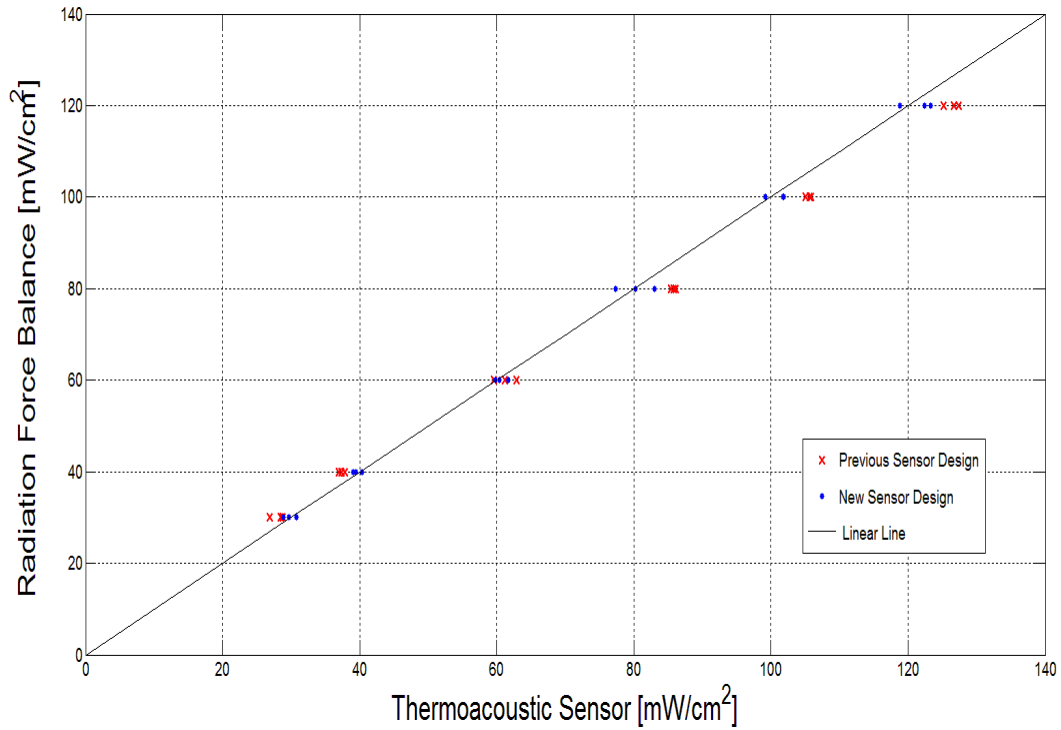


Figure 3.20: Comparison of the new sensors design measurements with that of the radiation force balance as a means to conduct a performance evaluation.

### 3.6 Discussion

A novel two-layer thermoacoustic sensor based on an artificial neural network as a means to adapt to temperature drifts was proposed, implemented, and investigated in order to measure low ultrasound intensities. Compared to the previous sensor design where only one layer of plexiglass absorber is used, the new sensor design employed two absorber layers with a plexiglass layer in the front and a rubber layer at the back. The current design has improved the sensor's absorption efficiency, as demonstrated by simulation, thus resulting in a more rapid and reliable estimation of ultrasound intensity. The two-layer sensor design

demonstrates that sensor performance can be improved by optimizing its physical structure.

The temperature increase of the sensor depends not only on the ultrasound intensity, but also on the ambient temperature and the slightly varying acoustic properties of the absorber materials with temperature, which makes sensor measurements a complicated inverse problem. It is extremely difficult to resolve the exact mathematical relation, which makes the traditional analytical method very complicated and inefficient. To overcome this difficulty, the method of artificial neural networks was proposed and applied into the thermoacoustic sensor design. As an experiment-based method, artificial neuronal networks provide a more reliable and effective solution. Application of the artificial neural network method requires training the data in a proper manner. The data are divided into two groups. Most of the data are used to directly train the network, while the other data are set aside for validation and testing purposes. If all the data are used to train the network, the problem of over-training appears, in which the trained network works well for the training data with minimum error, but cannot be generalized to the untrained data well. Therefore, some data are set aside to check for the presence of over-training and to decide when to stop training in order to obtain an optimal network that has the ability for generalization. Through proper training, the artificial neural network can learn the sensor characteristics and compensate for measurement errors caused by temperature drifts, which enables the sensor to directly measure the applied ultrasound intensity. The experimental results demonstrate that the trained network not only validates on

the data sets with training, but also is adaptive to the untrained data sets in the training range. The experimental results show that measurement error is reduced from greater than 15% without network compensation, to 1% with network compensation. The current design trained the network to adapt to room temperatures ranging from 20 °C to 26 °C, however, the adaptive temperature range of the sensor design can easily be extended by training more data sets in a wider temperature range.

Thermoacoustic sensors, due to their relatively simple structure, have the advantage of low cost and simplicity over the other techniques used to measure ultrasound intensities. The sensor design is based on the close-proximity sensor concept as a means to measure spatial-average temporal-average intensity ( $I_{sata}$ ), which not only simplifies the set-up, but also guarantees the consistency of each measurement. For the  $I_{sata}$  measurement, radiation force balance is a benchmark technique and has a minimal measurement uncertainty (3%) without vibration noises. The radiation force balance is used to calibrate the ultrasound generator for the sensor design, which would link the thermoacoustic sensor's measurement error to the radiation force balance's uncertainty, and the uncertainty of the beam area used to derive ultrasound intensity also contributes to the absolute calibration uncertainty of the thermoacoustic sensor, therefore, the sensor design cannot provide more accurate measurements than the radiation force balance in a vibration-free environment. However, in an environment with vibration noises, such as in a biology laboratory, the error of a radiation force balance can easily surpass 20% for low ultrasound intensity measurements, whereas our sensor

design only has an overall measurement uncertainty of 5%. For thermoacoustic sensors, it is better to let the sensor cool down before beginning the next measurement in order to maintain measurement accuracy. However, the cool-down time between measurements should not be considered as a disadvantage for the thermoacoustic sensor design, since the radiation force balance, as the benchmark technique, also needs a short period of time between measurements while it waits for a force balance. It takes around 10~15 seconds for the radiation force balance to take a measurement and 10~20 seconds between measurements to wait for a force balance to settle down, while it takes 12 seconds for our sensor to take a measurement and around 13 seconds for the sensor to cool down between measurements. Table 3.7 shows advantages and disadvantages of both techniques for further comparison. The designed thermoacoustic sensor can provide a real-time measurement and process of sensor's temperature change, since a microcontroller is used in the sensor design to form an embedded system, and the value of ultrasound intensity is obtained through measuring and processing temperature data in 12 seconds. The microcontroller is implemented in a printed circuit board outside the sensor to process the temperature data sent by the thermistor and to perform compensations based on the artificial neural network.

Table 3.7: Advantages and disadvantages of radiation force balance and the thermoacoustic sensor.

	Advantage	Disadvantage
Radiation Force Balance	<ul style="list-style-type: none"> <li>• A benchmark technique with minimal measurement uncertainty in a vibration-free environment</li> <li>• Versatile for a range of transducers in a wide intensity range</li> </ul>	<ul style="list-style-type: none"> <li>• Cannot provide accurate measurements with noise vibrations</li> <li>• Added complexity when measuring individual transducers in a transducer array</li> <li>• High cost</li> </ul>
Thermoacoustic Sensor	<ul style="list-style-type: none"> <li>• Measurements not affected by noise vibration</li> <li>• An easy-to-operate device for measuring individual transducers in a transducer array</li> <li>• Low cost</li> </ul>	<ul style="list-style-type: none"> <li>• A calibration process is needed for a particular transducer</li> <li>• Designed for low intensity ultrasound</li> </ul>

## **Chapter 4**

### **Increasing Vaccine Production Using Low Intensity**

#### **Pulsed Ultrasound**

Vaccination is a highly effective approach to prevent contagious diseases in humans and has contributed to the worldwide eradication of smallpox [51]. However, due to its manufactural costs, existing vaccines are often not available in the developing world, especially in economically underprivileged countries. Increasing vaccine production and lowering cost per unit becomes critical to promote universal vaccine immunization, which will further help to control healthcare spending associated with infectious diseases and ease the financial burden worldwide.

Our lab has developed a mechanical pulsed wave, especially low-intensity pulsed ultrasound (LIPUS) wave, that has shown great utility and promise in medical therapeutic treatments, including stem cell proliferation and differentiation [32], and antibody production [33-35]. Based on this technique, we hypothesize that a physical-based stimulation can enhance vaccine protein production and increase the rate of vaccine manufacture. In order to prove our concept, hepatitis B vaccines are chosen as a model system for vaccine production. LIPUS technology was employed to increase the production of hepatitis B vaccine based on baculovirus-insect cell expression systems (BCESs).

## **4.1 Materials and Methods**

### **4.1.1 Cell Culture and Infection**

Synthetic recombinant DNA technology based on protein expression systems is widely used for vaccine production. A pathogen comprises many subunits of proteins and only a portion of them plays an important role for inducing a protective immune response [85]. Subunit vaccines contain these components of a pathogen that elicit the immunological response. Recombinant protein production systems provide an efficient platform for the manufacture of subunit vaccines.

For the vaccine manufacture, recombinant protein production systems employ viral vectors to express the target proteins. Yeast, mammalian and insect expression systems are the most commonly employed recombinant protein production systems. Each expression system has its advantages and disadvantages, so the usage of system depends on the special requirements for the specific application. The yeast expression systems are of low cost and at low risk of contamination; yet, they lack the capacity to produce complex-structure proteins. For example, the system has previously failed to produce Pre-S2 antigen in Belgium, Japan, and the United States [56]. Compared to the yeast expression systems, the mammalian and insect expression systems are able to express complex-structure proteins, although with a higher cost. The mammalian expression systems, on the other hand, are at relatively high risk of contamination [85].

Balancing the pros and cons, we chose to use the insect cell expression systems for vaccine production. Although the cost of the systems is not as low as the yeast systems, the insect cell expression systems have several advantages: (1) The systems are highly versatile and can generate a wide range of complex-structure and biologically active proteins rapidly [61]. (2) The insect cell expression systems are also considered safe for humans because insects are the host for the baculoviruses in nature and the baculoviruses are non-pathogenic to humans [63]. (3) Unlike mammalian cells, insect cells can be cultivated without CO<sub>2</sub> incubator and they can easily withstand temperature variations [85]. (4) The insect cells can grow in serum-free culture media, which simplifies the purification process of the target recombinant proteins for vaccine production [62, 63]. Given these advantages, the baculovirus-insect cell expression systems have been used to achieve high levels of expression of recombinant proteins not only for exploratory research, but also for commercial production. Several insect-cell based proteins are currently used as therapeutic agents and vaccines (e.g. Provenge).

Sf9 insect cell line was chosen to produce the HBV S1/S2 protein in the experiment. Figure 4.1 shows the sf9 cells under a microscope stage. As a clonal isolate of Sf21 cells, Sf9 cell line is a continuous cell line developed from ovaries of the fall armyworm, which are relatively easy to maintain and can be cultivated well in suspension in large volumes at high densities. Therefore, the sf9 cells are commonly used for recombinant protein production through baculovirus. Akshaya Bio Inc. (Edmonton, AB, Canada) kindly provided Sf9 insect cells, which were

cultured and maintained in suspension in ESF 921 media (Expression Systems, Davis, CA95618, USA) in 125mL flasks at 27°C and 110 rpm. All shake flasks were purchased from Fisher Sci. (NH 03842 USA, Cat #: PBV125). The ESF 921 media is a serum-free, protein-free insect cell culture medium designed for robust growth and maximum expression of lepidopteran and dipteran cells [86].

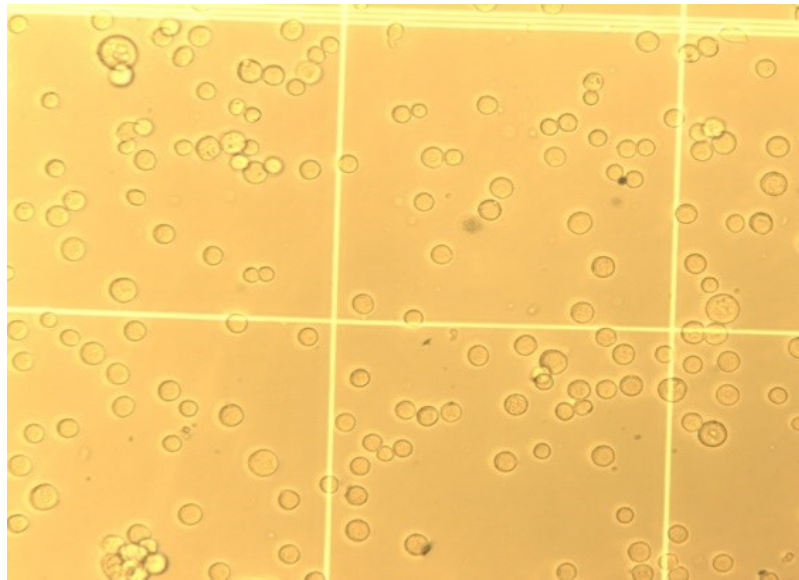


Figure 4.1: Sf9 cells observed under a microscope stage.

The baculovirus insect cell expression system employs recombinant baculoviruses to infect the cultured insect cells. Due to the rod shape of baculoviruses, a considerable amount of foreign gene can be accommodated within the virus particle [85]. Through the infection, expression vectors in the recombinant baculoviruses replicate and produce the target proteins in the cultured cells. In order to express the HBV S1/S2 protein, baculovirus encoding a 6×His-tag HBV S1/S2 protein sequence was used to infect the insect cell at a

Multiplicity of Infection (MOI) = 2, when the insect cell density reached  $2\sim 2.5 \times 10^6$  cells/mL. After 72 hours of infection the cell pellet was harvested by centrifugation.

#### **4.1.2 Ultrasound Treatment Method**

Low-intensity pulsed ultrasound (LIPUS) treatment was implemented using the LIPUS device (SonaCell) designed in our lab. The generated mechanical waves or ultrasound have a frequency of 1.5 MHz, a pulse repetition rate of 1.0 kHz, and a duty cycle of 20%. In our experiment, we used a circular transducer with an effective beam area of  $3.5 \text{ cm}^2$ . The beam area is the effective radiating area, which was directly measured by a needle hydrophone system (Precision Acoustics Inc. Dorchester, UK). Figure 4.2 shows the experimental setup, LIPUS device and ultrasound treatment process. After the insect cells were inoculated into shake flasks, LIPUS was applied to stimulate the insect cells in the shake flask through the ultrasound transducer placed underneath each flask. Ultrasound intensity, stimulation duration each time, and stimulation times per day are three ultrasound parameters in the biological experiments. The ultrasound intensity refers to spatially and temporally averaged intensity ( $I_{\text{sata}}$ ). The three ultrasound parameters were adjusted according to the designed experimental conditions. Following each stimulation, the culture flasks were placed back in the incubator-shaker as indicated in Figure 4.2.

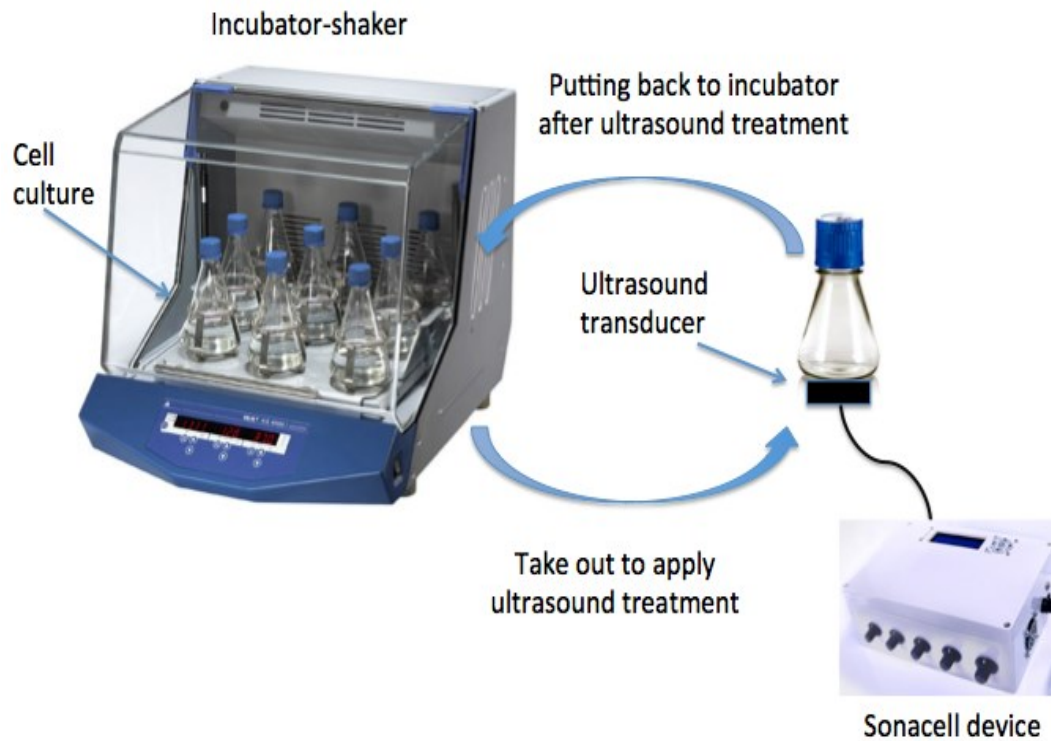


Figure 4.2: Experimental setup for increasing vaccine production. Here SonaCell is the device to generate low-intensity pulsed ultrasound (LIPUS).

### 4.1.3 Analysis Methods

#### 4.1.3.1 Cell Count

For many biological applications, such as microbiology, cell culture and blood test, it is required to determine the concentration of cells. The influence of ultrasound treatment toward insect cell growth was evaluated through cell count, expressed as the number of cells per unit of volume of the liquid media. The measurement infers the overall growth and liveliness of cells.

Viable and dead cells were counted using a hemocytometer with trypan blue staining. The hemocytometer was originally designed for blood cells count, but is employed to count all types of cells and particles in the fluid now [87]. A hemocytometer is a special type of glass microscope slide, which consists of two chambers. The chamber is engraved with a grid of perpendicular lines in the middle. The area bounded by the lines is known, since the grid is crafted with specified dimensions. There is coverslip over the chambers held at a height of 0.1mm, so the depth of the chamber is also known, when cell suspensions are loaded into the chamber, the volume of the cell suspension is known. Therefore, when the hemocytometer is placed on the microscope stage; the number of cells in a specific volume of the cell suspension can be counted [88].

To count cell number, the cell sample should be in an appropriate density. If the cell concentration level is too low, the number of cells loaded into the hemocytometer is limited and the accuracy of cell count would be affected, while an extreme high concentration induces cell overlaps, which pose challenges for accurate cell counting [88]. Therefore, it is necessary to dilute the cell sample when its concentration is too high for cell count. In this experiment, the insect cell sample was diluted four times, *i.e.* a 1:4 ratio, which was implemented by mixing one part of the cell sample with three parts of solution. Real cell concentration of the sample was calculated taking into account the dilution ratio after cell count. To distinguish dead cells from viable cells, trypan blue was added to the dilution solution. The special stain penetrates cell membranes of dead cells and colors them as blue, whereas it is not able to enter intact cell membranes of live cells.

The hemocytometer and its coverslip were cleaned with alcohol before use. Two identical samples were inserted into chambers of the hemocytometer and the averaged count was used in this study. When we compared the control (without ultrasound treatment) and ultrasound treated samples at each time point, we used the following equation to calculate the increase in cell count of ultrasound treated sample with respect to the control.

$$\text{Increase percentage} = \frac{(N_u - N_c)}{N_c} * 100\% \quad (4.1)$$

In the equation,  $N_u$  is the viable cell density with ultrasound treatment, and  $N_c$  is the viable cell density in control sample.

#### 4.1.3.2 Protein Analysis

Western blot was used to test the type and amount of proteins expressed by insect cells. Western blotting is a widely accepted technique in cell and molecular biology to determine the molecular weight of a protein and its relative amounts in different samples [89-99]. The technique employs gel electrophoresis to separate a mixture of proteins in a sample according to their molecular sizes [100, 101]. The proteins are then transferred from the gel to a membrane where the target protein is bound with label antibodies through incubation. The antibody has a reporter enzyme attached to it, which can generate light. So the target protein attached to the specific label antibody can be detected through optical equipment [102]. Western blot method provides a qualitative and quantitative measurement of a specific protein among a mixture. The procedure is described as follows.

- 1) Cell lysis: Cell lysis is a sample preparation process for the western blot, which extracts a mixture of proteins from cells. 5 mL sample of Sf9 cells was taken from cell cultures and centrifuged. The insect cells were then lysed in 250  $\mu$ L lysis buffer (50 mM Tris-HCl, pH 7.5, 150 mM NaCl, 1 mM EDTA, 1% TritonX-100, and protease inhibitor cocktail (Cat no.: 539134, Calbiochem, Gibbstown, NJ, USA)). The protease inhibitors were added to prevent the digestion of the proteins by the cell's enzymes. The lysate was then centrifuged at 12,000 rpm for 15 minutes at 4°C and the supernatant was collected for use.
- 2) Gel electrophoresis: Gel electrophoresis is used to separate the proteins of the sample based on molecular weight. In gel electrophoresis, the protein molecules are separated by applying an electrical field through a gel containing small pores. The speed of molecules to move through the gel is related to their lengths. Small molecules travel faster and migrate further distance through the gel than larger molecules because smaller molecules travel through the pores more easily [103]. Samples of the protein were run on 12% SDS-PAGE homogenous gel. A marker with a mixture of stained proteins was used to form colored bands, which defines molecular weights. The gel electrophoresis runs at a constant voltage of 100 V, until the bands of the colored mark separate and the front band reaches the bottom of gel.
- 3) Transfer: To make the proteins available for antibody detection, the proteins in the gel are required to transfer to a membrane made

of nitrocellulose or polyvinylidene difluoride (PVDF). The transfer of the proteins to the membrane is primarily accomplished through electroblotting, which employs an electrical current to pull proteins from the gel into the membrane and maintain the same organization [90]. In the experiment, the proteins in the gel were transferred to a polyvinyl difluoride membrane (Bio-Rad Laboratories, Richmond, CA).

- 4) Incubation: The purpose of incubation is to specifically bind an enzyme-labeled antibody to the protein of interest [104]. When exposed to an appropriate substrate, the reporter enzyme of the antibody can produce color or light for detection. The membrane was first blocked in 5% milk at 4°C overnight, which prevents any nonspecific binding of antibodies to the surface of the membrane to minimize background noise and get clearer result. The membrane was incubated for 1 h at room temperature with 1:2000 6×His mAb with HRP Conjugate (Cat no: 631210, Clontech, Mountain View, CA 94043, USA). After that, it was visualized using enhanced chemiluminescence assay (ECL kit, Amersham, London, UK)

To compare protein levels, the result of western blot is assessed via comparing protein bands of different samples. For quantitative determination, the blot image was analyzed with ImageJ, an image analysis software widely used by biologists in quantitating visual analysis (free software downloaded from: <http://rsbweb.nih.gov/ij/index.html>). Protein levels were quantified as the mean of integrated optical density.

## 4.2 Experiment Results

### 4.2.1 Screening LIPUS Conditions for Insect Cell Growth

We have applied LIPUS to various cell systems such as stem cells, hybridoma cells, and CHO cells [32-35]. We discovered that the ultrasound intensity ( $I_{sata} = 60 \text{ or } 80 \text{ mW/cm}^2$ ) with 10 minutes treatment was a better condition for cell growth [32-35]. In this study, a quick screening experiment was performed to compare the treatment effects with ultrasound intensity of 40, 60 and 80 mW/cm<sup>2</sup> on Sf9 insect cells. We found that applying ultrasound earlier is not good for cell growth, particularly right after inoculation, since the Sf9 cells are weak after inoculation and need time to adapt to the new environment, and immediate application of ultrasound has an adverse effect on cell growth. Therefore, in all the experiments, we applied the ultrasound stimulation one day after inoculation. Figure 4.3 shows the experiment result. As indicated in the figure, we found 60 mW/cm<sup>2</sup> was better than 40 and 80 mW/cm<sup>2</sup> for cell growth. Therefore, the ultrasound intensity was set to 60 mW/cm<sup>2</sup> in all experiments.

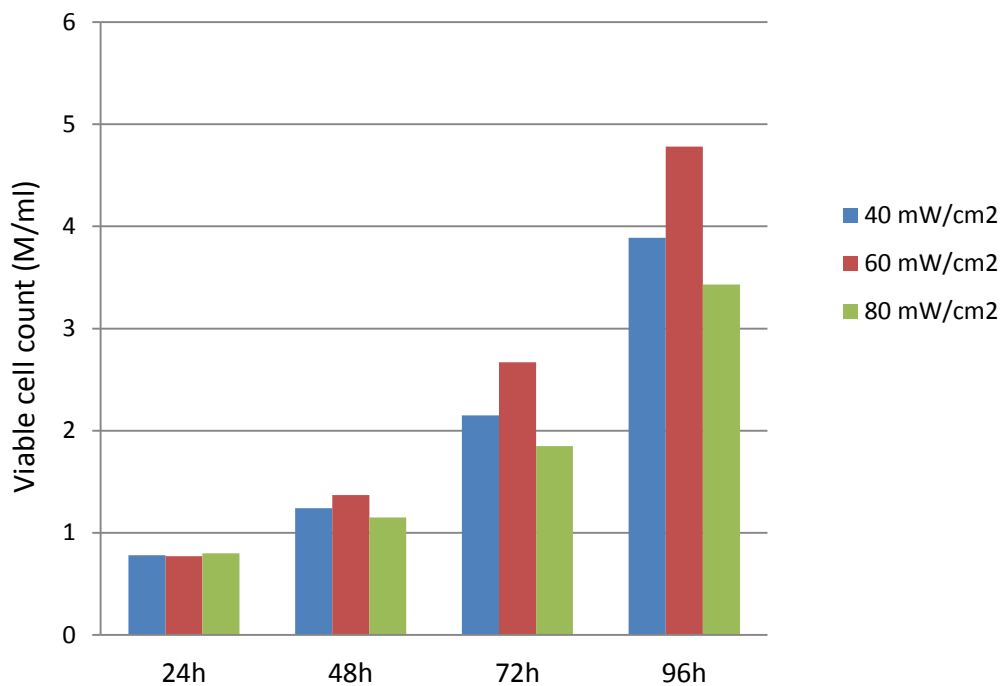


Figure 4.3: Insect cell growth under different ultrasound intensities at 40, 60 and 80 mW/cm<sup>2</sup>.

After the screening experiment, we designed another experiment to search for treatment duration and treatment times per day. Although 10 minutes per treatment and once a day is good for most cell systems such as stem cells, Hybridoma cells, and CHO cells [32-35] for their growth, we tested treatment frequency of two times per day to see whether more treatments per day can achieve better results. Three flasks were prepared to grow insect cells:

- one is the control (without ultrasound treatment),
- one is treated 10 minutes per treatment and once a day,
- the last flask is treated 10 minutes per treatment but twice a day.

The viable cell density at each time point was counted and compared. The results are shown in Figure 4.4. Overall, one treatment per day shows better results than two treatments per day for the growth of insect cells.

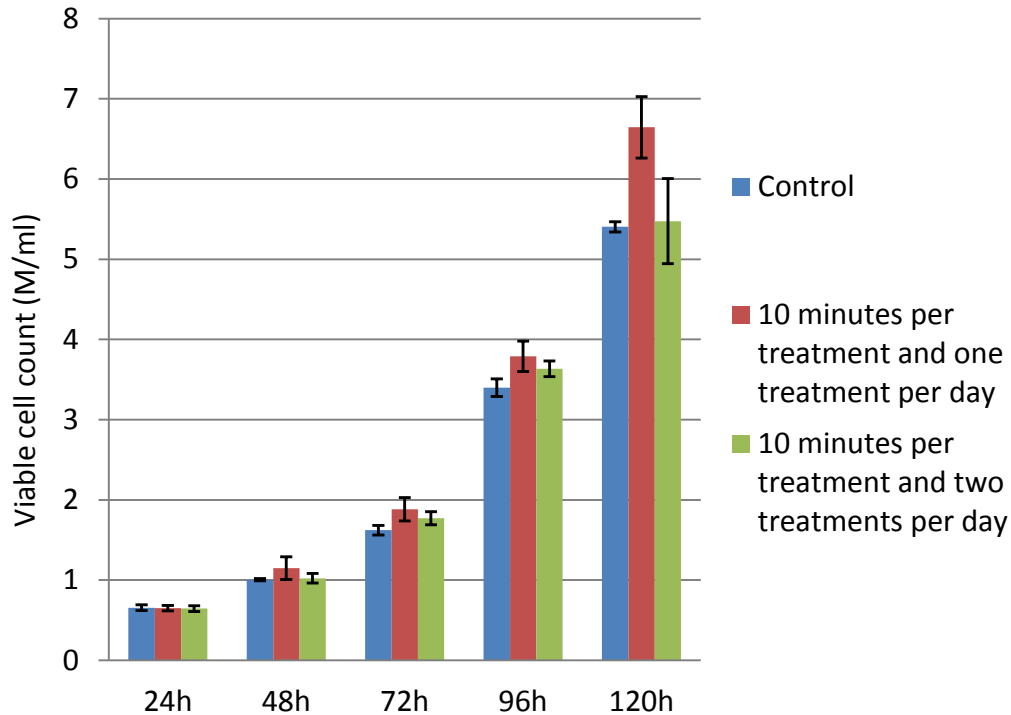


Figure 4.4: Insect cell growth in 30 mL media in shake flask with various ultrasound treatments. The control refers to insect cell culture without ultrasound treatment. The ultrasound intensity is set at  $60 \text{ mW/cm}^2$ .

We designed another experiment to further test if longer treatment duration could yield better results. Three flasks were prepared to grow insect cells:

- one is the control (without ultrasound treatment),
- one is treated 10 minutes per treatment and once a day,
- the last flask is treated 15 minutes per treatment and one treatment per day.

Figure 4.5 shows the result of the viable cell density at each time point in different flasks. The experimental result shows that 10 minutes per treatment is better than 15 minutes per treatment for the growth of insect cells.

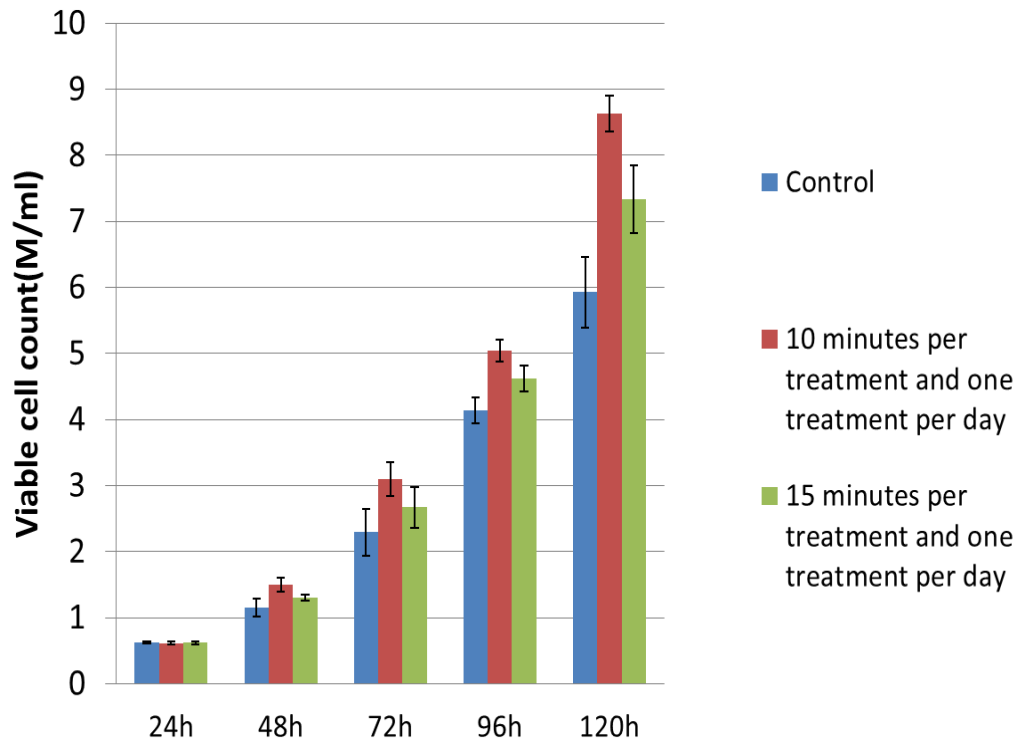


Figure 4.5: Insect cell growth in 30 mL media in shake flask with 10 minute and 15 minute ultrasound treatments. Control refers to insect cell culture without ultrasound treatment. The ultrasound intensity is set at 60 mW/cm<sup>2</sup>.

#### 4.2.2 LIPUS Stimulation and Infection

In this experiment, we used LIPUS to stimulate insect cell and then infected the cells with the recombinant baculovirus. The recombinant baculoviruses were used to infect the insect cells when they were cultured to  $2.0\sim 2.5 \times 10^6$  cells/mL. The cell samples were harvested after 144 hours before the number of cells started to drop. After that, the generated protein level of insect cells was determined by

the Western blotting. We designed the experiment with two ultrasound cultures to check ultrasound effect on protein production. LIPUS was used to stimulate cells to  $2.0\sim 2.5 \times 10^6$  cells/mL for both of the ultrasound cultures. After infection, one culture sample did not receive ultrasound treatment anymore, while the other culture was still stimulated until harvest. Figure 4.6 shows the cells' growth curve.

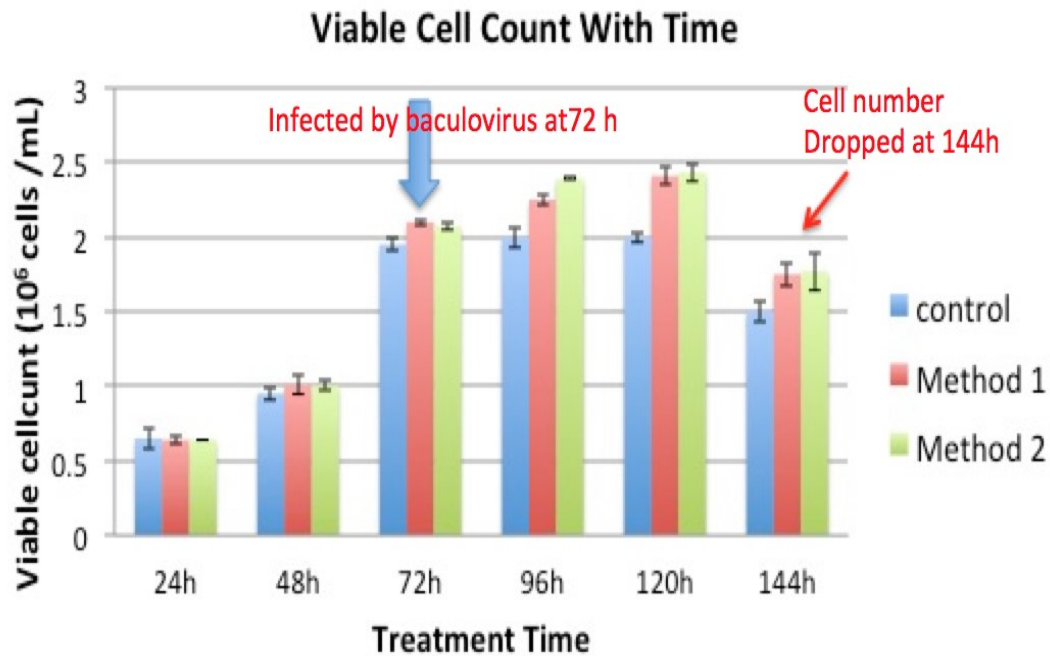


Figure 4.6: Cells' growth curve. Method 1 is the one that stops sonication after infection while method 2 is the one with continuous ultrasound stimulation. Cells were infected by baculovirus at 72 hours.

#### 4.2.3 Checking Protein Production Increase

Figure 4.7 shows the western blotting results. The target protein (HBV pre S1/S2 protein) expressed by Sf9 insect cells has the molecular weight of 25kDa. Sample 1 comes from insect cells without virus infection, sample 2 is the control sample that the cells were infected by virus but not stimulated by ultrasound,

sample 3 comes from an ultrasound culture for which ultrasound stimulation stopped after virus infection, and sample 4 is the other ultrasound culture for which ultrasound stimulation continued after virus infection. As indicated in the figure, there is no target protein shown in lane 1, since no virus was used to infect the cells in sample 1 to express the target protein. For the other three samples with virus infection, a band of target protein was evident in lane 2, 3 and 4. To quantitatively compare the protein expression levels, the result of western blot was assessed through ImageJ. The software was employed to estimate the change of band area density of protein in different samples. Results showed that protein production increased by 22% and 56% relative to the control after ultrasound treatment using method 1 and method 2, respectively.

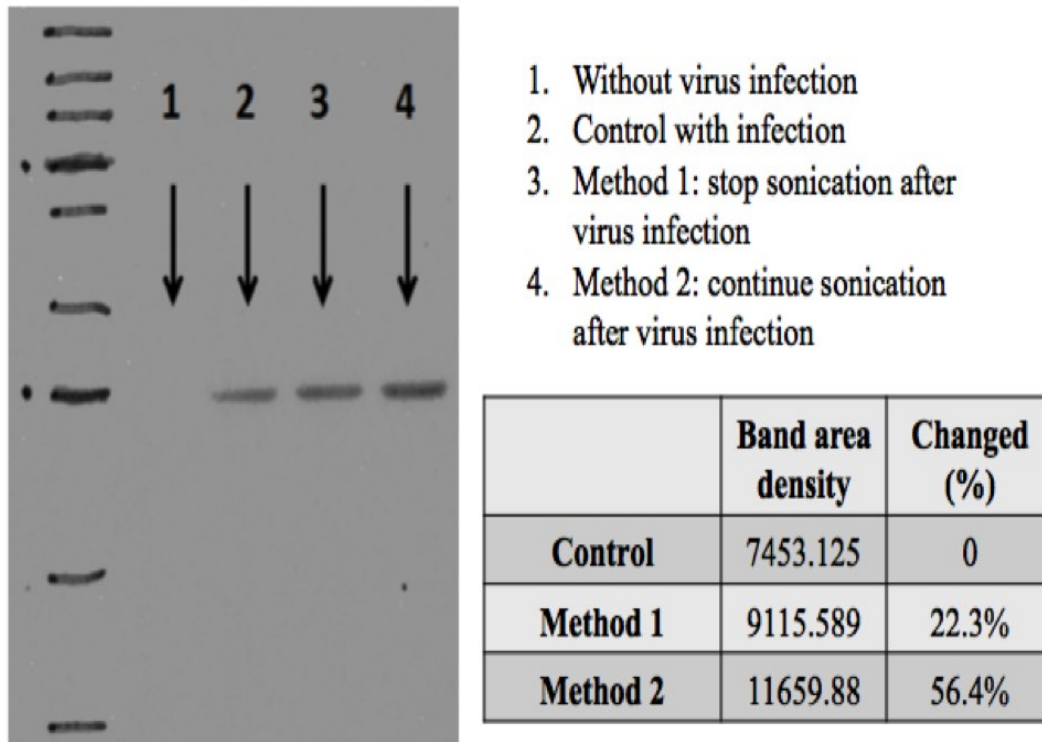


Figure 4.7: The Western blotting results. ImageJ software was used to measure the band area density change.

### 4.3 Discussions

#### 4.3.1 One Treatment Per Day is Better than Two Treatments Per Day

From Figure 4.4, we can see that cell density increased by a maximum of 23% than controls at 120 hours for the group with 10 minutes treatment per day. No significant increase, however, was observed for the group with 10 minutes per treatment and twice treatments per day. Overall, one treatment per day shows better results than two treatments per day for the growth of insect cells. One of the possible reason is the Sf9 cell membrane is delicate. Although the proper

ultrasound stimulation increases the cell membrane permeability, which promotes the cell metabolism and leads to the cell number increase, the *Sf9* cell membrane still needs a period of time to recover after the ultrasound treatment. Two treatments per day seem too many ultrasound treatments that can break cell membrane and affect the further increase of the cell number. We also found that applying ultrasound earlier is not good for the growth of insect cells, especially just after inoculation. The possible reason is also quite similar, since the *Sf9* cells are weak after inoculation and need time to get used to the new environment, and immediate application of ultrasound has an adverse effect on cell growth. Therefore, in all our experiments, we let the cell grow one day after inoculation and then we applied the ultrasound stimulation.

#### **4.3.2 Treatment of 10 Minutes Per Day is Better than that of 15 Minutes Per Day**

From the experiment results in Figures 4.5, we can come to the conclusion that 10 minutes treatment per day is better than 15 minutes treatment per day for the growth of insect cells. The experimental results also confirm that too much ultrasound treatment cannot further promote cell growth.

Ultrasound intensity, stimulation duration each time and stimulation times per day are key parameters in the ultrasound treatment. While it is challenging to find the combination of the parameters for optimal insect cell growth among unlimited possibilities, we demonstrated that the ultrasound treatment is effective on 30 mL working volume of cell culture for preliminary investigation, validating

our hypothesis that LIPUS is able to enhance protein production. In the future, scale-up experiments based on larger working volume are further required to obtain industry-level vaccine production; the corresponding ultrasound treatment conditions will be thoroughly investigated.

### **4.3.3 Continuous Ultrasound Stimulation is Better than No Stimulation After Infection**

Figure 4.6 show that the infection by baculovirus affects insect growth. After adding the virus at 72 hours, the cell number in all the groups begins to increase slowly: the nucleus of cells became larger, and the cell shape became more circular. At harvest (144 hours) or after 72 hours from adding the virus, we discovered that the cell number in all the groups dropped dramatically since a number of cells died due to the virus infection. Figure 4.6 and 4.7 show that method 2 (or continuous LIPUS stimulation after infection) is better than method 1 (or no stimulation after infection).

### **4.3.4 Protein Production Increase**

We define the Cell Productivity (CP) as the production of protein per cell, and we assume the blot band density is the concentration of protein produced from the insect cells. We can calculate the insect cell's CP by the following equation:

$$CP = \frac{\textit{Band density}}{\textit{Viable cell density at the time of infection}} \quad (4.2)$$

We can compare the CP of infected cells with and without ultrasound treatment, and the calculated CP values are listed in Table 4.1. Ultrasound stimulation can increase the cell's productivity.

Table 4.1: Cell productivity increase after sonication.

	Infection density (cells/mL)	Band area density	CP	Increase over control (%)
Control	$2.130 \times 10^6$	7453.125	0.03499	0
Method 1	$2.345 \times 10^6$	9151.589	0.03887	11.1
Method 2	$2.345 \times 10^6$	11659.88	0.04972	42.1

When cells were infected, we either continuously applied ultrasound (method 2) or stopped sonication (method 1). We did not observe significant differences in cell number between one with ultrasound stimulation until harvest vs. the one with continuous sonication (only at 96 hours, the cell number using method 2 is statistically better than that using method 1). However, from the western blotting results (refer to Figure 4.7), we indeed discovered that continuous ultrasound stimulation increased cell productivity to express target protein by 42% (method 2) while stopping sonication after viral infection (method 1) increased the cell productivity by 11%, a much lesser amount.

## **Chapter 5**

### **Conclusions and Future Work**

#### **5.1 Conclusions**

The low-intensity pulsed ultrasound (LIPUS) technology is a powerful tool for therapeutic treatment and has opened a promising interdisciplinary research field in biomedical engineering. Contributions were made to the field on two important frontiers: design of LIPUS sensor, and its applications on enhancing vaccine production for therapeutic application.

For the electrical design, to make the ultrasound platform work for various biological experiments, accurate measurement and calibration of ultrasound intensity is important. Although the radiation force balance is still the gold standard method for ultrasound intensity measurement with minimal error, the application of the technique is limited by the requirements of experience in equipment setup and operation and may not be justified in many cases. In addition, measurement accuracy is affected by background vibrations, which in turn limits its application in biology laboratories. Due to the limitations, a sensor based on the thermal method has been designed and implemented to measure and calibrate the intensity of LIPUS. The designed sensor determines the ultrasound intensity according to the temperature rise caused by the heat produced from incident acoustic energy, thus is vibration-resistant in nature. To make the sensor easy to operate and stable during each measurement, the sensor setup procedure is simplified by adopting a concept of close-proximity in new sensor design where a

sensor is directly coupled to the transducer through the ultrasound medium (ultrasound gel or degassed water) to perform the measurements. Therefore, the thermoacoustic sensor design provides an easy-to-operate and vibration-resistant alternative for rapidly measuring low ultrasound intensity (30 mW/cm<sup>2</sup> to 120 mW/cm<sup>2</sup>) with high accuracy, especially in a practical environment like a biology laboratory.

The designed two-layer thermoacoustic sensor based on an artificial neural network integrates several novel components. Compared to former thermoacoustic sensor design where only one layer of plexiglass absorber was used, the new sensor design employed two absorber layers with a plexiglass layer in the front and a rubber layer at the back. The proposed two-layer structure has markedly improved the absorption efficiency, resulting in a more rapid and reliable estimation of ultrasound intensity. The measurement time shortened from 20 seconds to 12 seconds. To correct for temperature drifts that have shown negative impact on measurement accuracy, an artificial neural network algorithm was proposed and applied in the new design to provide accurate and consistent measurements for a range of ambient temperatures. The experimental result shows that the compensation provided by the artificial neural network reduced the temperature drift errors from more than 15% to 1%. In addition, the sensor design is based on a close-proximity sensor concept to provide the measurement of spatial-average temporal-average intensity ( $I_{sata}$ ), which not only simplifies the setup, but also guarantees the consistency of each measurement without the use of

a positioning system. The final results show that the new sensor achieves an average error of  $1.31 \text{ mW/cm}^2$  over 18 measurement samples.

As indicated in Table 3.6, both the radiation force balance and the thermoacoustic sensor have their own advantages and disadvantages. Although thermoacoustic sensors are unlikely to replace the radiation force balance as the industry standard for ultrasound measurement and calibration, the designed thermoacoustic sensor, as a low-cost technique, can provide rapid ultrasound intensity measurements without any complex set-up procedure, which provides a convenient alternative or reciprocal technique to the standard technique, especially in a practical environment like a biology laboratory.

For biological experiments, low-intensity pulsed ultrasound (LIPUS) was employed to enhance vaccine production. Vaccines have been proven to be a highly effective and cost-efficient approach to control contagious diseases in humans. However, due to manufacturing costs, existing vaccines are often not widely available in the developing world, especially in economically underprivileged countries. Increasing vaccine production would reduce the costs of the vaccines and promote universal vaccine immunization, which can effectively control the infectious diseases worldwide. Different from other biological methods, LIPUS is a unique physical-based approach to increase the vaccine production, which has not been investigated in literature and in patents before.

In this study, hepatitis B vaccine based on baculovirus-insect cell expression systems (BCESs) was used as a model system to demonstrate how the LIPUS

technology can increase the vaccine production. Hepatitis B virus (HBV) S1/S2 proteins are the envelop proteins of the virus that play an important role in inducing an immune response to HBV. *Sf9* cells were chosen as the insect cell line for stimulation to express HBV S1/S2 proteins. The experimental results demonstrated that LIPUS stimulation of 10 minutes per day at a frequency of 1.5MHz, intensity of 60 mW/cm<sup>2</sup> significantly increased both cell growth and vaccine production. The tests also showed that continuous sonication is better than stopping LIPUS stimulation after viral infection. Continuous ultrasound stimulation can achieve about a 40% increase in HBV S1/S2 production, while stopping sonication after viral infection increased the cell productivity by almost 11%. This finding is very meaningful for efficiently shortening vaccine production time or increasing the yield of proteins for vaccine use to reduce the manufacture costs of the vaccines.

## **5.2 Future Work**

In this thesis, a sensor based on the thermal method has been successfully designed and implemented to measure and calibrate the intensity of LIPUS, which provides an easy-to-operate and low-cost alternative to the standard technique. The two-layer sensor design demonstrates that sensor performance can be improved by optimizing its physical structure. Although the sensor achieves a satisfying performance, the physical design of the sensor is still not optimal, and improvement can be made to achieve better performance. In this sensor design, plexiglass was selected as the material of the sensor's first layer, since it is low-cost and easy-to-process material available with good acoustic impedance

matching with ultrasound medium. However, the acoustic impedance matching between plexiglass and ultrasound medium is not perfect. As calculated in Chapter 2, around 14% of the ultrasound energy was reflected at the medium-sensor interface due to impedance mismatch. If a customized material with perfect acoustic impedance matching is synthesized, the ultrasound energy can be totally transmitted into the sensor, which would greatly improve the sensor's absorption efficiency, resulting in a more rapid and reliable estimation of ultrasound intensity.

For vaccine production, the experimental results demonstrated that LIPUS stimulation of 10 minutes per day at intensity of  $60 \text{ mW/cm}^2$  can significantly increase the production by 40%. In the experiments, ultrasound treatment was implemented based on 30 mL working volume of cell culture in a 125 mL shake flask. Scale-up experiments with more working volume would further increase vaccine production and reduce the cost. For the scale-up experiment, further investigation of ultrasound conditions or dose is necessary to accommodate the increased working volume. As the working volume of cell culture increases, each cell receives less ultrasound stimulation. In this case, an increase of ultrasound dose is needed to cover the whole working volume. Methods include using transducer array with more transducers, increasing output ultrasound intensity of the transducer and extending the ultrasound treatment duration.

## References

- [1] Jack Blitz, "Fundamental of Ultrasonics." Second Edition, Plenum Press, 1967.
- [2] Leighton, Timothy G. "What is ultrasound?." *Progress in biophysics and molecular biology* 93.1 (2007): 3-83.
- [3] Manbachi, Amir, and Richard SC Cobbold. "Development and application of piezoelectric materials for ultrasound generation and detection." *Ultrasound* 19.4 (2011): 187-196.
- [4] Harcke, H. T., and S. J. Kumar. "The role of ultrasound in the diagnosis and management of congenital dislocation and dysplasia of the hip." *J Bone Joint Surg Am* 73.4 (1991): 622-628.
- [5] Kothari, Shivangi, and Vivek Kaul. "Therapeutic Applications of Endoscopic Ultrasound." *Ultrasound Clinics* 9.1 (2014): 53-65.
- [6] Wood, Robert Williams, and Alfred L. Loomis. "The physical and biological effects of high-frequency sound-waves of great intensity." *The London, Edinburgh, and Dublin philosophical magazine and journal of science* 4.22 (1927): 417-436.
- [7] Ter Haar, Gail. "Therapeutic applications of ultrasound." *Progress in biophysics and molecular biology* 93.1 (2007): 111-129.
- [8] Ter Haar, Gail. "Therapeutic ultrasound." *European Journal of Ultrasound* 9, no. 1 (1999): 3-9.

- [9] Paliwal, Sumit, and Samir Mitragotri. "Therapeutic opportunities in biological responses of ultrasound." *Ultrasonics* 48.4 (2008): 271-278.
- [10] O'Brien, William D. "Ultrasound–biophysics mechanisms." *Progress in biophysics and molecular biology* 93.1 (2007): 212-255.
- [11] Di Lullo, Gloria A., et al. "Mapping the ligand-binding sites and disease-associated mutations on the most abundant protein in the human, type I collagen." *Journal of Biological Chemistry* 277.6 (2002): 4223-4231.
- [12] Chang, Chen-Jung, and Shan-Hui Hsu. "The effects of low-intensity ultrasound on peripheral nerve regeneration in poly (DL-lactic acid-co-glycolic acid) conduits seeded with Schwann cells." *Ultrasound in medicine & biology* 30.8 (2004): 1079-1084.
- [13] Mourad, Pierre D., et al. "Ultrasound accelerates functional recovery after peripheral nerve damage." *Neurosurgery* 48.5 (2001): 1136-1141.
- [14] Rantanen, Jussi, et al. "Effects of therapeutic ultrasound on the regeneration of skeletal myofibers after experimental muscle injury." *The American Journal of Sports Medicine* 27.1 (1999): 54-59.
- [15] Enwemeka, Chukuka S., Oscar Rodriguez, and Sonia Mendosa. "The biomechanical effects of low-intensity ultrasound on healing tendons." *Ultrasound in medicine & biology* 16.8 (1990): 801-807.
- [16] Reed, Brian, and Takamaru Ashikaga. "The effects of heating with ultrasound on knee joint displacement." *Journal of Orthopaedic & Sports Physical Therapy* 26.3 (1997): 131-137.

- [17] Demir, Huseyin, et al. "Comparison of the effects of laser and ultrasound treatments on experimental wound healing in rats." *Journal of rehabilitation research and development* 41 (2004): 721-728.
- [18] Mortimer, A. J., and M. Dyson. "The effect of therapeutic ultrasound on calcium uptake in fibroblasts." *Ultrasound in medicine & biology* 14.6 (1988): 499-506.
- [19] Chapman, I. V., N. A. MacNally, and S. Tucker. "Ultrasound-induced changes in rates of influx and efflux of potassium ions in rat thymocytes in vitro." *Ultrasound in medicine & biology* 6.1 (1980): 47-49.
- [20] Umemura, S., et al. "Recent advances in sonodynamic approach to cancer therapy." *Ultrasonics Sonochemistry* 3.3 (1996): S187-S191.
- [21] Lawrie, Allan, et al. "Ultrasound enhances reporter gene expression after transfection of vascular cells in vitro." *Circulation* 99.20 (1999): 2617-2620.
- [22] Tata, Darrell B., Floyd Dunn, and Donald J. Tindall. "Selective clinical ultrasound signals mediate differential gene transfer and expression in two human prostate cancer cell lines: LnCap and PC-3." *Biochemical and biophysical research communications* 234.1 (1997): 64-67.
- [23] Webster, D. F., et al. "The role of cavitation in the in vitro stimulation of protein synthesis in human fibroblasts by ultrasound." *Ultrasound in medicine & biology* 4.4 (1978): 343-351.

- [24] Webster, D. F., et al. "The role of ultrasound-induced cavitation in the 'in vitro' stimulation of collagen synthesis in human fibroblasts." *Ultrasonics* 18.1 (1980): 33-37.
- [25] Klopotek, Peter J. "Method and apparatus for therapeutic treatment of skin with ultrasound." U.S. Patent No. 6,113,559. 5 Sep. 2000.
- [26] Reher, Peter, et al. "The stimulation of bone formation in vitro by therapeutic ultrasound." *Ultrasound in medicine & biology* 23.8 (1997): 1251-1258.
- [27] K.N. Malizos, M.E. Hantes, V. Protopappas and A. Papachristos, "Low-intensity pulsed ultrasound for bone healing: An overview." *Injury* 37.1 (2006): S56-S62.
- [28] Anil Khanna, Richard T. C. Nelmes, Nikolaos Gougoulas, Nicola Maffulli, Jim Gray, "The effects of LIPUS on soft-tissue healing: a review of literature." *British medical bulletin* 89.1 (2009): 169-182.
- [29] El-Bialy, Tarek, Iman El-Shamy, and Thomas M. Graber. "Repair of orthodontically induced root resorption by ultrasound in humans." *American journal of orthodontics and dentofacial orthopedics* 126.2 (2004): 186-193.
- [30] Al-Daghreer, S., Doschak, M., Sloan, A.J., Major, P.W., Heo, G., Scurtescu, C., Tsui, Y.Y., El-Bialy, T., "Long term effect of Low Intensity Pulsed Ultrasound on a human tooth slice organ culture." *Archives of oral biology* 57.6 (2012): 760-768.
- [31] Marvel, Skylar, et al. "The development and validation of a LIPUS system with preliminary observations of ultrasonic effects on human adult stem

cells." *Ultrasonics, Ferroelectrics, and Frequency Control, IEEE Transactions on* 57.9 (2010): 1977-1984.

[32] Peng Xu, Hilal Gul-Uludag, Woon T. Ang, Xiaoyan Yang, Min Huang, Leah Marquez-Curtis, Locksley McGann, Anna Janowska-Wieczorek, James Xing, Eric Swanson, Jie Chen, " Low-intensity pulsed ultrasound-mediated stimulation of hematopoietic stem/progenitor cell viability, proliferation and differentiation in vitro." *Biotechnology letters* 34.10 (2012): 1965-1973.

[33] Yupeng Zhao, Woon T. Ang, James Xing, Jian Zhang, and Jie Chen, "Applications of ultrasound to enhance mycophenolic acid production." *Ultrasound in medicine & biology* 38.9 (2012): 1582-1588.

[34] James Xing, Xiaoyan Yang, Peng Xu, Woon T. Ang, and Jie Chen, "Ultrasound-enhanced monoclonal antibody production." *Ultrasound in medicine & biology* 38.11 (2012): 1949-1957.

[35] Yupeng Zhao, Jida Xing, James Z. Xing, Woon T. Ang, Jie Chen, "Applications of low-intensity pulsed ultrasound to increase monoclonal antibody production in CHO cells using shake flasks or wavebags." *Ultrasonics* 54.6 (2014): 1439-1447.

[36] Artho, Paul A., et al. "A calibration study of therapeutic ultrasound units." *Physical Therapy* 82.3 (2002): 257-263.

[37] Beissner, K. "On the plane - wave approximation of acoustic intensity." *The Journal of the Acoustical Society of America* 71.6 (1982): 1406-1411.

- [38] Zeqiri, Bajram, et al. "A novel pyroelectric method of determining ultrasonic transducer output power: Device concept, modeling, and preliminary studies." *Ultrasonics, Ferroelectrics, and Frequency Control, IEEE Transactions on* 54.11 (2007): 2318-2330.
- [39] Fay, Burkhard, and Michael Rinker. "The thermoacoustic effect and its use in ultrasonic power determination." *Ultrasonics* 34.2 (1996): 563-566.
- [40] Wilkens, V. "A thermal technique for local ultrasound intensity measurement: part 1. Sensor concept and prototype calibration." *Measurement Science and Technology* 21.11 (2010): 115805.
- [41] Wilkens, Volker, and Hans-Peter Reimann. "Output intensity measurement on a diagnostic ultrasound machine using a calibrated thermoacoustic sensor." *Journal of Physics: Conference Series*. Vol. 1. No. 1. IOP Publishing, 2004.
- [42] Wilkens, V. "A thermal technique for local ultrasound intensity measurement: part 2. Application to exposimetry on a medical diagnostic device." *Measurement Science and Technology* 21.11 (2010): 115806.
- [43] Myers, Matthew R., and Bruce A. Herman. "A theoretical assessment of a thermal technique to measure acoustic power radiated by ultrasound transducers." *Ultrasonics, Ferroelectrics, and Frequency Control, IEEE Transactions on* 49.5 (2002): 565-572.

- [44] Wilkens, Volker. "Thermoacoustic ultrasound power measurement using evaluation of transient temperature profiles." *Ultrasonics Symposium, 2002. Proceedings. IEEE*. Vol. 2.
- [45] M. Hagan, H. Demuth, M. Beale, "Neural Network Design" (PWS Publishing, Boston, 1996)
- [46] Noriega, Jose R., and Hong Wang. "A direct adaptive neural-network control for unknown nonlinear systems and its application." *Neural Networks, IEEE Transactions on* 9.1 (1998): 27-34.
- [47] Neelamegam, P., and A. Rajendran. "An approach to measure the densities of solids using an artificial neural network." *Instrumentation science & technology* 35.2 (2007): 189-199.
- [48] Jagdish C. Patra, Adriaan van den Bos, Alex C. Kot, "An ANN-based smart capacitive pressure sensor in dynamic environment", *Sensors and Actuators A: Physical* 86.1 (2000): 26-38.
- [49] Hafiane, Mohamed Lamine, Zohir Dibi, and Otto Manck. "On the capability of artificial neural networks to compensate nonlinearities in wavelength sensing." *Sensors* 9.4 (2009): 2884-2894.
- [50] Baha, Hakim, and Zohir Dibi. "A novel neural network-based technique for smart gas sensors operating in a dynamic environment." *Sensors* 9.11 (2009): 8944-8960.
- [51] Van Oers, Monique M. "Vaccines for viral and parasitic diseases produced with baculovirus vectors." *Advances in virus research* 68 (2006): 193-253.

- [52] Williams, Roger. "Global challenges in liver disease." *Hepatology* 44.3 (2006): 521-526.
- [53] Trépo, Christian, Henry LY Chan, and Anna Lok. "Hepatitis B virus infection." *The Lancet* 384.9959 (2014): 2053-2063.
- [54] Liaw, Yun-Fan, and Chia-Ming Chu. "Hepatitis B virus infection." *The Lancet* 373.9663 (2009): 582-592.
- [55] Chen, Ding-Shinn. "From hepatitis to hepatoma: lessons from type B viral hepatitis." *Science* 262.5132 (1993): 369-370.
- [56] Zanetti, Alessandro R., Pierre Van Damme, and Daniel Shouval. "The global impact of vaccination against hepatitis B: a historical overview." *Vaccine* 26.49 (2008): 6266-6273.
- [57] Jane N. Zuckerman, Arie J. Zuckerman, Ian Symington, Wei Du, "Evaluation of a new hepatitis B triple - antigen vaccine in inadequate responders to current vaccines." *Hepatology* 34.4 (2001): 798-802.
- [58] E. Hardy, E. Martínez, D. Diago, R. Díaz, D. González, L. Herrera, "Large-scale production of recombinant hepatitis B surface antigen from *Pichia pastoris*." *Journal of biotechnology* 77.2 (2000): 157-167.
- [59] Stephenne, J. "Development and production aspects of a recombinant yeast-derived hepatitis B vaccine." *Vaccine* 8 (1990): S69-S73.
- [60] I. Grotto, Y. Mandel, M. Ephros, I. Ashkenazi, J. Shemer, "Major adverse reactions to yeast-derived hepatitis B vaccines—a review." *Vaccine* 16.4 (1998): 329-334.

- [61] Cox, Manon MJ. "Recombinant protein vaccines produced in insect cells." *Vaccine* 30.10 (2012): 1759-1766.
- [62] van Oers, Monique M. "Opportunities and challenges for the baculovirus expression system." *Journal of invertebrate pathology* 107 (2011): S3-S15.
- [63] Farrell, P. J., L. Swevers, and K. Iatrou. "Insect cell culture and recombinant protein expression systems." *Comprehensive Molecular Insect Science. San Diego, USA: Elsevier* (2005): 475-507.
- [64] Hu, Yu-Chen, Kun Yao, and Tzong-Yuan Wu. "Baculovirus as an expression and/or delivery vehicle for vaccine antigens." *Expert review of vaccines* 7.3 (2008): 363-371.
- [65] NDT Resource Center. Near Field Calculation. [https://www.nde-ed.org/GeneralResources/Formula/UTFormula/near\\_field/near.htm](https://www.nde-ed.org/GeneralResources/Formula/UTFormula/near_field/near.htm).
- [66] NDT Resource Center. Ultrasonic Formula. <https://www.nde-ed.org/GeneralResources/Formula/UTFormula/ultrasonicFormula.htm>.
- [67] D. Ensminger, L. Bond, "Ultrasonics: Fundamentals, technology, applications." 3rd ed. Boca Raton, Florida: CRC Press, 2011.
- [68] Xing, Jida, Michael Choi, Woon Ang, Xiaojian Yu, and Jie Chen. "Design and characterization of a close-proximity thermoacoustic sensor." *Ultrasound in medicine & biology* 39.9 (2013): 1613-1622.
- [69] Wilson, J. Thermal Diffusivity. <http://www.electronics-cooling.com/2007/08/thermal-diffusivity>.

[70] Martin O. Culjat, David Goldenberg, Priyamvada Tewari, Rahul S. Singh. "A review of tissue substitutes for ultrasound imaging." *Ultrasound in medicine & biology* 36.6 (2010): 861-873.

[71] Wikipedia. Speed of sound. [http://en.wikipedia.org/wiki/Speed\\_of\\_sound](http://en.wikipedia.org/wiki/Speed_of_sound)

[72] NDT Resource Center. Material Properties Tables Acoustic Properties. [https://www.nde-ed.org/GeneralResources/MaterialProperties/UT/ut\\_matlprop\\_index.htm](https://www.nde-ed.org/GeneralResources/MaterialProperties/UT/ut_matlprop_index.htm).

[73] Ohmic Instruments. UPM-DT-1AV. <http://www.ohmicinstruments.com/pdf/Manuals/UPM-DT1AVand10AVman.pdf>.

[74] Needle hydrophones. <http://acoustics.co.uk/products/pressure-intensity-measurements/needle-hydrophones>.

[75] Xing, Jida, and Jie Chen. "Design of a Thermoacoustic sensor for low intensity ultrasound measurements based on an artificial neural network." *Sensors* 15.6 (2015): 14788-14808.

[76] AptFlex F28. <http://acoustics.co.uk/wp-content/uploads/2014/01/Apflex-F28.pdf>.

[77] Treeby, Bradley E., and Benjamin T. Cox. "k-Wave: MATLAB toolbox for the simulation and reconstruction of photoacoustic wave fields." *Journal of biomedical optics* 15.2 (2010): 021314-021314.

[78] Treeby, Bradley E., et al. "Modeling nonlinear ultrasound propagation in heterogeneous media with power law absorption using a k-space pseudospectral

method." *The Journal of the Acoustical Society of America* 131.6 (2012): 4324-4336.

[79] K-Wave User Manual. [http://www.k-wave.org/manual/k-wave\\_user\\_manual\\_1.0.1.pdf](http://www.k-wave.org/manual/k-wave_user_manual_1.0.1.pdf).

[80] Efendioglu, Hasan S., Tulay Yildirim, and Kemal Fidanboylu. "Prediction of force measurements of a microbend sensor based on an artificial neural network." *Sensors* 9.9 (2009): 7167-7176.

[81] Zurada, Jacek M. "Introduction to artificial neural systems." St. Paul: West, 1992.

[82] Hu, Y.H.; Hwang, J.N. "Handbook of Neural Network Signal Processing." CRC Press: Washington, DC, USA, 2002.

[83] Hornik, Kurt, Maxwell Stinchcombe, and Halbert White. "Multilayer feedforward networks are universal approximators." *Neural networks* 2.5 (1989): 359-366.

[84] Wefky, Ahmed M., et al. "Alternative sensor system and MLP neural network for vehicle pedal activity estimation." *Sensors* 10.4 (2010): 3798-3814.

[85] Van Oers, Monique M. "Vaccines for viral and parasitic diseases produced with baculovirus vectors." *Advances in virus research* 68 (2006): 193-253.

[86] ESF 921 media. <http://www.expressionsystems.com/products/00006/esf921.pdf>.

[87] Hemocytometer. <https://en.wikipedia.org/wiki/Hemocytometer>.

- [88] Cell Counting with a Hemocytometer. <http://bitesizebio.com/13687/cell-counting-with-a-hemocytometer-easy-as-1-2-3/>.
- [89] Dalmau, Josep, et al. "Detection of the anti - Hu antibody in the serum of patients with small cell lung cancer—a quantitative western blot analysis." *Annals of neurology* 27.5 (1990): 544-552.
- [90] Ida, Nobuo, et al. "Analysis of heterogeneous  $\beta$ A4 peptides in human cerebrospinal fluid and blood by a newly developed sensitive Western blot assay." *Journal of Biological Chemistry* 271.37 (1996): 22908-22914.
- [91] Ashley, Rhoda L., et al. "Comparison of Western blot (immunoblot) and glycoprotein G-specific immunodot enzyme assay for detecting antibodies to herpes simplex virus types 1 and 2 in human sera." *Journal of Clinical Microbiology* 26.4 (1988): 662-667.
- [92] Shacter, Emily, et al. "Differential susceptibility of plasma proteins to oxidative modification: examination by western blot immunoassay." *Free Radical Biology and Medicine* 17.5 (1994): 429-437.
- [93] Mary, C., et al. "Western blot analysis of antibodies to *Leishmania infantum* antigens: potential of the 14-kD and 16-kD antigens for diagnosis and epidemiologic purposes." *The American journal of tropical medicine and hygiene* 47.6 (1992): 764-771.
- [94] Wallis, R. S., M. Amir-Tahmasseb, and J. J. Ellner. "Induction of interleukin 1 and tumor necrosis factor by mycobacterial proteins: the monocyte western blot." *Proceedings of the National Academy of Sciences* 87.9 (1990): 3348-3352.

- [95] Assous, M. V., et al. "Western blot analysis of sera from Lyme borreliosis patients according to the genomic species of the *Borrelia* strains used as antigens." *European Journal of Clinical Microbiology and Infectious Diseases* 12.4 (1993): 261-268.
- [96] Peden, Alexander H., et al. "Preclinical vCJD after blood transfusion in a PRNP codon 129 heterozygous patient." *The Lancet* 364.9433 (2004): 527-529.
- [97] Eastwood, Sharon L., and Paul J. Harrison. "Synaptic pathology in the anterior cingulate cortex in schizophrenia and mood disorders. A review and a Western blot study of synaptophysin, GAP-43 and the complexins." *Brain research bulletin* 55.5 (2001): 569-578.
- [98] Lee, Douglas C., et al. "Monitoring plasma processing steps with a sensitive Western blot assay for the detection of the prion protein." *Journal of virological methods* 84.1 (2000): 77-89.
- [99] Nadala, Elpidio Cesar B., et al. "Detection of yellowhead virus and Chinese baculovirus in penaeid shrimp by the Western blot technique." *Journal of virological methods* 69.1 (1997): 39-44.
- [100] Ghaemmaghami, Sina, et al. "Global analysis of protein expression in yeast." *Nature* 425.6959 (2003): 737-741.
- [101] Mahmood, Tahrin, and Ping-Chang Yang. "Western blot: technique, theory, and trouble shooting." *North American journal of medical sciences* 4.9 (2012): 429.
- [102] Western blot. <http://www.nature.com/scitable/definition/western-blot-288>.

[103] Gel electrophoresis. <http://www.nature.com/scitable/definition/gel-electrophoresis-286>.

[104] Western blot. [https://en.wikipedia.org/wiki/Western\\_blot](https://en.wikipedia.org/wiki/Western_blot).

## Appendix A: Preliminary Thermoacoustic Sensor Code

```
#include <avr/pgmspace.h>
#include <avr/io.h>
#include <stdio.h>
#include <inttypes.h>
#include <util/delay.h>
#include <string.h>
#include <stdlib.h>
#include <math.h>
#include <avr/interrupt.h>
#define F_CPU 12000000UL

volatile int count = 200; //Define variables for temperature calculation and
curving fitting//
volatile int Condition = 0;
int i = 0;
int j = 0;
long x;
long x0 = 0;
long dif = 0;
double v;
double v0;
double s;
double I;
double c1;
double c2;
double c3;
double c4;
int e;
int f;

int k=20; //Initialize parameter values//
double a = 0;
double a0 = 0;
double b = 7;
double c = 1.6238;
double d = 46.7459;
double T0 = 23;
double T1 = 28;
double E;
double Estore;

void UartTransmitterInit(void) //Initialize UART transmitter//
{
    UBRR0L = 77;
    UCSROA = (0<<U2X0) | (0<<MPCM0);
    UCSROB = (0<<RXCIE0) | (0<<TXCIE0) | (0<<UDRIE0) | (0<<RXEN0) | (1<<TXEN0) | (0<<UCSZ02);
    UCSROC =
```

```
(0<<UMSEL00) | (0<<UMSEL01) | (0<<UPM00) | (0<<UPM01) | (0<<USBS0) | (1<<UCSZ01) | (1<<UCSZ00) |
(0<<UCPOL0);
```

```
    return;
}
```

```
void UartTransmitterInit1(void)           //Initialize UART1 to transmit and
receive//
{
    UBRR1L = 77;
    UCSR1A = (0<<U2X1) | (0<<MPCM1);
    UCSR1B = (1<<RXCIE1) | (0<<TXCIE1) | (0<<UDRIE1) | (1<<RXEN1) | (1<<TXEN1) | (0<<UCSZ12);
    UCSR1C =
(0<<UMSEL11) | (0<<UMSEL10) | (0<<UPM11) | (0<<UPM10) | (0<<USBS1) | (1<<UCSZ11) | (1<<UCSZ10) |
(0<<UCPOL1);
    return;
}
```

```
void USART_Transmit(unsigned char data, FILE *stream )
{
    loop_until_bit_is_set(UCSR0A, UDRE0);
    UDRO = data;
    return;
}
```

```
int uart_getchar(FILE *stream)
{
    char c;
    loop_until_bit_is_set(UCSR0A, RXCO);
    if (UCSR0A & _BV(FE0))
        return _FDEV_EOF;
    if (UCSR0A & _BV(DOR0))
        return _FDEV_ERR;
    c = UDRO;
    return(c);
}
```

```
FILE uart_str = FDEV_SETUP_STREAM(USART_Transmit, uart_getchar, _FDEV_SETUP_RW);
```

```
void RTCInit (void)           //Set frequency and clock//
{
    TIMSK2 &= ~((1 << OCIE2B) | (1 << OCIE2A) | (1 << TOIE2));
    TCCR2A = (0<<WGM21) | (0<<WGM20);
    TCCR2B = (0<<WGM22);
    ASSR = (1<<AS2);
    TCNT2 = 0; OCR2B = 0x00;
    OCR2A = 31;
}
```

```

    TCCR2B = (0x7 << CS20);
    TCCR2A = (1 << WGM21);
    TIMSK2 = (1 << OCIE2A);
    return;
}

void Measurement (void)          // Measure voltage of thermistor //
{

    double CH;
    double CL;
    double high;
    double low;

    x = 0;
    y = 0;

    PORTB = 0xFF;
    PORTD = 0x03;
    PORTC = 0x20;

    for (int counter = 0; counter < 256; counter++)    //Read ADC and do addition//
    {
        ADCSRA |= (1<<ADSC);
        CL = ADCL; // low 8 bits
        CH = ADCH; // high 8 bits

        while(!(ADCSRA & (1<<ADIF)));
        ADCSRA|= (1<<ADIF);

        high = pow(16, 2) * CH;
        low = CL;

        y = high + low;
        x = x + y;
    }

    PORTD = 0x01;
    PORTC = 0x20;

    x = x >> 4;

    v = (x) * -0.01481 + 76.69;          // Temperature conversion//

    PORTD = 0x00;
    PORTC = 0x00;
    PORTB = 0x00;
}

void Ecalculation (void)        // Curve fitting error calculation//
{

```

```

    E = v - T0 - a*((1 - exp(-i/b)));
    E = pow(E, 2);

    return;
}
void func_operation (void)    // Adjust coefficient C value//
{

    if (operation == 1) {
        Ecalculation();

        if (count <= 130) {
            a = a + 0.1;
        }

        if (count > 130) {
            a = a + 0.01;
        }

        operation = Echeck(operation);
    }

    if (operation == 2)
    {

        Ecalculation();

        if (count <= 130) {
            a = a - 0.1;
        }
        if (count > 130)
        {
            a = a -0.01;
        }
        operation = Echeck(operation);
    }

    return;
}
int Echeck (int current_operation)
{
    int operation;
    double Eadjust;
    double Edif;

    Eadjust = v - T0 - a*((1 - exp(-i/b)));
    Eadjust = pow(Eadjust, 2);
    Edif = Eadjust - E;
}

```

```

if (Edif < 0) {

    if (current_operation == 1) {
        operation = 1;
    }
    if (current_operation == 2) {
        operation = 2;
    }
}

if (Edif > 0) {
    if (current_operation == 1) {
        operation = 2;
    }
    if (current_operation == 2) {
        operation = 1;
    }
}

return operation;
}

void calculateCurve(void) //Calculate intensity based on coefficient C//
{

    c4=-0.9316*s+20.69; //40
    c3=-0.7736*s+20.2; //60
    c2=-0.8154*s+23.41; //80
    c1=-0.7929*s+25.46; //100

    if(i>10)
    { a=a0/5;
        if(a<c4)
        {
            I=40+k*(a-c4)/(c3-c4);
        }
        else if(a<c3)
        {
            I=60-k*(c3-a)/(c3-c4);
        }
        else if(a<c2)
        {
            I=80-k*(c2-a)/(c2-c3);
        }
        else if (a<c1)
        {
            I=100-k*(c1-a)/(c1-c2);
        }
    }
}

```

```

        else
        {
            I=100+k*(a-c1)/(c1-c2);
        }
        int e = (I-(int)I)*100;
        int f = (int)I;
        a0=0;
        Condition = 2;

        printf("Intensity is "); // Output intensity value //
        printf("%d.%d;", f, e);
        printf ("\n\r");
        printf ("\n\r");
        i=0;
    }
    else
    {
        Ecalculation();
        Es = E;

        while (count!= 0)
        {
            if( E >= 0.0001)
            {
                func_operation ();
            }
            count = count - 1;
        }
        count=200;
        if(i>5)
        {
            a0=a0+a;
        }
    }
    return;
}

```

```

ISR(TIMER2_COMPA_vect) // Comparision interruption//
{

```

```

    Measurement();

    int m = (v-(int)v)*100;
    int n = (int)v;

    if (Condition == 0)
    {

        printf ("T:");
        printf("%d.%d;", n, m);
    }

```

```

printf ("\n\r");
dif = x0-x;
if (dif < 1000) // Temperature change detection //
{
    if (dif >= 3)
    {
        printf ("\n\r");
        printf("Sensor ON");

        printf ("\n\r");
        printf("Sensor Calculating");
        s = v0;
        Condition = 1;
    }
    x0 = x;
    v0 = v;
}

if (Condition == 1)
{
    if(a==0)
    {
        a=0.70084*s-12.194;

        T0=s;
    }
    i++;
    calculateCurve();
}

if (Condition == 2)
{
    if(j>5)
    {
        Condition = 0;
        j=0;
        a=0;
    }
    else
    {
        j++;
    }
    x0 = x;
}

}

void ADCinit (void)
{

```

```

    ADMUX |=
(0<<REFS1) | (0<<REFS0) | (0<<ADLAR) | (0<<MUX4) | (0<<MUX3) | (0<<MUX2) | (0<<MUX1) | (0<<MUX0) ;
    ADCSRA |= (1<<ADEN) | (1<<ADPS2) | (1<<ADPS1) | (1<<ADPS0) ;
    ADCSRB &= (0<<ADTS2)&(0<<ADTS1)&(0<<ADTS0) ;

}

int main(void)
{
    sei();
    DDRB = 0xFF;           //Set I/O //
    DDRC = 0xFF;
    DDRD = 0xFF;

    UartTransmitterInit(); //Initialize UART transmitter//
    UartTransmitterInit1();
    ADCinit();
    RTCinit();

    stdout = &uart_str;   // Establish the default streams to use the uart//
    stdin = &uart_str;
    stderr = &uart_str;

    while(1)
    {

        TIMSK2 |= (1 << OCIE2A); // Timer Interruption //

    }

    return 0;
}

```

## Appendix B: Improved Thermoacoustic Sensor Code

```
#include <avr/pgmspace.h>
#include <avr/io.h>
#include <stdio.h>
#include <inttypes.h>
#include <util/delay.h>
#include <string.h>
#include <stdlib.h>
#include <math.h>
#include <avr/interrupt.h>
#define F_CPU 12000000UL

double w11= 3.5008;           // Define and set parameters for neural network//
double w12= 5.0117;
double w13= 0.47412;
double w21= -1.3035;
double w22= 4.4669;
double w23= -0.10647;
double w31= 0.1084;
double w32= 0.014241;
double w33= 2.8166;
double b11= -3.3727;
double b12= 1.8568;
double b13= 0.086394;
double b2= -0.079312;
double h1;
double h2;
double h3;
double H1;
double H2;
double H3;

volatile int count = 200; // set variables for temperature calculation and
curving fitting//
volatile int Condition = 0;
int i = 0;
int j = 0;
long x;
long x0 = 0;
long dif = 0;
double v;
double v0;
double s;
double s1;
double I;
double I1;
int e;
int f;
```

```

int k=20;
double a = 0;
double a0 = 0;
double a1 = 0;
double b = 13.5;
double T0 = 23;
double E;
double Estore;

void UartTransmitterInit(void) //Initialize UART transmitter//
{
    UBRROL = 77;
    UCSROA = (0<<U2X0) | (0<<MPCM0);
    UCSROB = (0<<RXCIE0) | (0<<TXCIE0) | (0<<UDRIE0) | (0<<RXEN0) | (1<<TXEN0) | (0<<UCSZ02);
    UCSROC =
(0<<UMSEL00) | (0<<UMSEL01) | (0<<UPM00) | (0<<UPM01) | (0<<USBS0) | (1<<UCSZ01) | (1<<UCSZ00) |
(0<<UCPOL0);

    return;
}

void UartTransmitterInit1(void) //Initialize UART1 to transmit and receive//
{
    UBRRI1 = 77;
    UCSRI1A = (0<<U2X1) | (0<<MPCM1);
    UCSRI1B = (1<<RXCIE1) | (0<<TXCIE1) | (0<<UDRIE1) | (1<<RXEN1) | (1<<TXEN1) | (0<<UCSZ12);
    UCSRI1C =
(0<<UMSEL11) | (0<<UMSEL10) | (0<<UPM11) | (0<<UPM10) | (0<<USBS1) | (1<<UCSZ11) | (1<<UCSZ10) |
(0<<UCPOL1);
    return;
}

void USART_Transmit(unsigned char data, FILE *stream )
{
    loop_until_bit_is_set(UCSROA, UDRE0);
    UDRO = data;
    return;
}

int uart_getchar(FILE *stream)
{
    char c;
    loop_until_bit_is_set(UCSROA, RXC0);
    if (UCSROA & _BV(FE0))
        return _FDEV_EOF;
    if (UCSROA & _BV(DOR0))
        return _FDEV_ERR;
    c = UDRO;
}

```

```

    return(c);
}

FILE uart_str = FDEV_SETUP_STREAM(USART_Transmit, uart_getchar, _FDEV_SETUP_RW);

void RTCInit (void)                                //Set frequency and clock//
{
    TIMSK2 &= ~((1 << OCIE2B) | (1 << OCIE2A) | (1 << TOIE2));
    TCCR2A = (0<<WGM21) | (0<<WGM20);
    TCCR2B = (0<<WGM22);
    ASSR = (1<<AS2);
    TCNT2 = 0; OCR2B = 0x00;
    OCR2A = 31;
    TCCR2B = (0x7 << CS20);
    TCCR2A = (1 << WGM21);
    TIMSK2 = (1 << OCIE2A);
    return;
}

void Measurement (void)                            // Measure voltage of thermistor//
{
    double CH;
    double CL;
    double high;
    double low;

    x = 0;
    y = 0;

    PORTB = 0xFF;
    PORTD = 0x03;
    PORTC = 0x20;

    for (int counter = 0; counter < 256; counter++) //Read ADC and do addition//
    {
        ADCSRA |= (1<<ADSC);
        CL = ADCL; // low 8 bits
        CH = ADCH; // high 8 bits

        while(!(ADCSRA & (1<<ADIF)));
        ADCSRA|= (1<<ADIF);

        high = pow(16, 2) * CH;
        low = CL;

        y = high + low;
        x = x + y;
    }
}

```

```

PORTD = 0x01;
PORTC = 0x20;

x = x >> 4;

v = (x) * -0.01481 + 76.69;          // Temperature conversion//

PORTD = 0x00;
PORTC = 0x00;
PORTB = 0x00;
}

void Ecalculation (void)            // Curve fitting error calculation//
{
    E = v - T0 - a*((1 - exp(-i/b)));
    E = pow(E, 2);

    return;
}

void func_operation (void)          // Adjust coefficient C //
{

    if (operation == 1) {
        Ecalculation();

        if (count <= 130) {
            a = a + 0.1;
        }

        if (count > 130) {
            a = a + 0.01;
        }

        operation = Echeck(operation);
    }

    if (operation == 2)
    {

        Ecalculation();

        if (count <= 130) {
            a = a - 0.1;
        }
        if (count > 130)
        {
            a = a -0.01;
        }
        operation = Echeck(operation);
    }
}

```

```

        }

    return;
}

int Echeck (int current_operation)
{
    int operation;
    double Eadjust;
    double Edif;

    Eadjust = v - T0 - a*((1 - exp(-i/b)));
    Eadjust = pow(Eadjust, 2);
    Edif = Eadjust - E;

    if (Edif < 0) {

        if (current_operation == 1) {
            operation = 1;
        }
        if (current_operation == 2) {
            operation = 2;
        }
    }

    if (Edif > 0) {
        if (current_operation == 1) {
            operation = 2;
        }
        if (current_operation == 2) {
            operation = 1;
        }
    }

    return operation;
}

void ANNetwork(void) // Neural network processing //
{

    if(i>10)
    { a=a0/5;

        s1=(s-23)/3; // Normalize input data //
        a1=(2*a-11.4061)/9.4594;

        h1=w11*(a1)+w21*(s1)+b11;
    }
}

```

```

        h2=w12*(a1)+w22*(s1)+b12;

        h3=w13*(a1)+w23*(s1)+b13;

        H1=2/(1+exp(-2*h1))-1;

        H2=2/(1+exp(-2*h2))-1;

        H3=2/(1+exp(-2*h3))-1;

        I1=w31*(H1)+w32*(H2)+w33*(H3)+b2;

        I=40*I1+70;
    }

    int e = (I-(int)I)*100;
    int f = (int)I;
    a0=0;

    Condition = 2;

        printf("Intensity is "); // Output intensity value //
        printf("%d.%d;", f, e);
        printf ("\n\r");
        printf ("\n\r");
        i=0;
    }
    else
    {
    Ecalculation();
    Es = E;

    while (count!= 0)
    {
        if( E >= 0.0001)
        {
            func_operation ();
        }
        count = count - 1;
    }
    count=200;
    if(i>5)
    {
        a0=a0+a;
    }

    }
    return;
}

ISR(TIMER2_COMPA_vect) // Comparison interruption//
{

```

```

Measurement();

int m = (v-(int)v)*100;
int n = (int)v;

if (Condition == 0)
{
    dif = x0-x;
    if (dif < 1000) // Temperature change detection //
    {
        if (dif >= 3)
        {
            printf ("\n\r");
            printf("Sensor ON");

            printf ("\n\r");
            printf("Sensor Calculating");
            s = v0;
            Condition = 1;
        }
    }

    x0 = x;
    v0 = v;
}

if (Condition == 1)
{
    if(a==0)
    {
        a=0.70084*s-12.194;

        T0=s;
    }
    i++;
    ANNetwork();
}

if (Condition == 2)
{
    if(j>5)
    {
        Condition = 0;
        j=0;
        a=0;
    }
    else
    {
        j++;
    }
    x0 = x;
}

```

```

    }
}

void ADCinit (void)
{
    ADMUX |=
(0<<REFS1) | (0<<REFS0) | (0<<ADLAR) | (0<<MUX4) | (0<<MUX3) | (0<<MUX2) | (0<<MUX1) | (0<<MUX0);
    ADCSRA |= (1<<ADEN) | (1<<ADPS2) | (1<<ADPS1) | (1<<ADPS0);
    ADCSRB &= (0<<ADTS2)&(0<<ADTS1)&(0<<ADTS0);
}

int main(void)
{
    sei();
    DDRB = 0xFF;           // Set I/O //
    DDRC = 0xFF;
    DDRD = 0xFF;

    UartTransmitterInit(); // Initialize UART transmitter//
    UartTransmitterInit1();
    ADCinit();
    RTCInit();

    stdout = &uart_str;   // Establish the default streams to use the uart //
    stdin = &uart_str;
    stderr = &uart_str;

    while(1)
    {
        TIMSK2 |= (1 << OCIE2A); // Timer Interruption //
    }

    return 0;
}

```